

**INFLUENCE OF RICE HUSK DERIVED NANO-SILICA ON  
PERFORMANCE, EMISSIONS, AND COMBUSTION  
CHARACTERISTICS OF DIESEL ENGINE FUELED WITH BAOBAB  
BIODIESEL**

**Fredrick Andrew Kapile**

**A Dissertation Submitted in Fulfillment of the Requirements for the Degree of Doctor of  
Philosophy in Sustainable Energy Sciences and Engineering of the Nelson Mandela  
African Institution of Science and Technology**

**Arusha, Tanzania**

**August, 2024**

## ABSTRACT

The increasing number of on-road automobiles as a result of an exponential increase in population and lifestyle places enormous strain on depleted fossil petroleum fuel, energy security, and environmental stability. This situation drives researchers to find an alternative source to replace petroleum diesel. Biodiesel is one of the promising viable substitutes. However, biodiesels may not always fulfill the EN 14214 standard due to differences in fuel properties. This could cause issues with engine operation and emissions. This study therefore aims to use novel nano-silica ( $\text{SiO}_2$ ) additives extracted from rice husk to improve its fuel properties. Also focuses on the influence of additives on the operation of the compression ignition (CI) engine. The *Adansonia digitata* methyl esters (ADME) were made by transesterification process, The physicochemical properties of the fuels with and without additives were measured as per ASTM D6751 and EN 14214 standards methods, and nano-silica was analyzed by Thermogravimetry (TGA), Fourier transform infrared spectroscopy (FT-IR), Brunauer Emmett Teller (BET), X-ray diffractometer (XRD. Barret-Joyner Halenda (BJH) pore diameter, specific surface area, and pore volume of  $\text{SiO}_2$  were observed to be 19.3 nm, 502.24  $\text{m}^2/\text{g}$ , and 0.761  $\text{cm}^3/\text{g}$ , respectively. At 400 and 800 ppm dose levels, the oxidation induction period (OIP) increased dramatically, peaking at 10.03 h. The stability of ADME has significantly improved, as evidenced by these results, meeting the >3 h and >8 h standard limits set by ASTM D6751 and EN 14214, respectively. The viscosity of B100 decreased with increasing additive content, from 4.62  $\text{mm}^2/\text{s}$  for neat B100 to 2.21  $\text{mm}^2/\text{s}$  for 400 ppm. Cetane number (CN) (60 to 64). All nano-fuel blends used in engine tests were prepared by an ultrasonication process. The results revealed that the brake thermal efficiency (BTE) at maximum brake powers (BP) for B20, B20+ $\text{SiO}_2$ , B100, and B100+ $\text{SiO}_2$  fuels were 29.9, 28.2, 28.44, and 27.1%, respectively, and brake-specific fuel consumption (BSFC) was reduced as the load increased. The peak heat release rate (HRR) of the B100+ $\text{SiO}_2$  and B20+ $\text{SiO}_2$  are slightly higher by 2.9 and 2.6%, respectively, than the neat B100 at medium BP. However, in-cylinder gas pressure (CGP) increased following the order of B20+ $\text{SiO}_2$ <B20<B100<B100+  $\text{SiO}_2$ <B0. Moreover, the exhaust emissions of nano-fuel blends exhibited a greater reduction of CO, THC,  $\text{CO}_2$ ,  $\text{NO}_x$ , and particulate matter (PM) compared to B20 and B100. Overall, this study recommends that  $\text{SiO}_2$  nano-additive is a good substitute fuel additive to use with biodiesel and its blends because of the improved properties of biodiesel, decreased emissions, and increased engine performance efficiency.

## DECLARATION

I, Fredrick Andrew Kapile, do hereby declare to the senate of Nelson Mandela African Institution of Science and Technology that this dissertation is my original work and that it has neither been submitted nor being concurrently submitted for degree award in any other institution.

Fredrick Andrew Kapile



22<sup>nd</sup> August, 2024

---

**Name of Candidate**

**Signature**

**Date**

The above declaration is confirmed by:

Prof. Thomas T. Kivevele



22<sup>nd</sup> August, 2024

---

**Name of Supervisor 1**

**Signature**

**Date**

Prof. Akos Bereczky



22<sup>nd</sup> August, 2024

---

**Name of Supervisor 2**

**Signature**

**Date**

Prof. Justin Ntalikwa



22<sup>nd</sup> August, 2024

---

**Name of Supervisor 3**

**Signature**

**Date**

## **COPYRIGHT**

This dissertation is copyright material protected under the Berne Convention, the Copyright Act of 1999 and other international and national enactments, in that behalf, on intellectual property. It must not be reproduced by any means, in full or in part, except for short extracts in fair dealing; for researcher private study, critical scholarly review or discourse with an acknowledgment, without a written permission of the Deputy Vice Chancellor for Academic, Research and Innovation, on behalf of both the author and the Nelson Mandela African Institution of Science and Technology.

## CERTIFICATION

The undersigned certify that, they have read and hereby recommend for acceptance by the Nelson Mandela African Institution of Science and Technology a dissertation titled “**Influence of Rice Husk Derived Nano-Silica on Performance, Emissions, and Combustion Characteristics of Diesel Engine Fueled with Baobab Biodiesel**” in partial fulfillment of the requirements for the Degree of Doctor of Philosophy in Sustainable Energy Sciences and Engineering of the Nelson Mandela African Institution of Science and Technology.

Prof. Thomas Kivevele

22<sup>nd</sup> August, 2024

---

**Name of Supervisor 1**

**Signature**

**Date**

Prof. Akos Bereczky

22<sup>nd</sup> August, 2024

---

**Name of Supervisor 2**

**Signature**

**Date**

Prof. Justin Ntalikwa

22<sup>nd</sup> August, 2024

---

**Name of Supervisor 3**

**Signature**

**Date**

## **ACKNOWLEDGEMENTS**

I thank God for his daily healing, peace, and guidance. This was much needed in tackling this monumental task. I want to thank the Government of Tanzania through the Ministry of Education Science and Technology (MoEST) for the financial support of my studies at Nelson Mandela Africa Institution of Science and Technology (NM-AIST). I extend my appreciation to my employer, the Dar es Salaam University College of Education (DUCE) for granting the study leave and financial support.

My profound appreciation is extended to my supervisors, Prof. Thomas Kivevele from NM-AIST, Arusha, and Prof. Akos Bereczky for their grants for the ERASMUS mobility grants to conduct experiments in Hungary (Budapest University of Technology and Economics) as well as their technical support, tutoring, and engine testing, I also thank study in Hungary as well as their technical support, tutoring, and engine testing. I also thank Prof. Justin Ntalikwa from the University of Dodoma (UDOM) for his input advice discussion, supervision, and guidance to accomplish this dissertation.

In addition, many thanks go to the NM-AIST laboratory team for technical and analytical assistance. I would also like to extend my gratitude to my fellow students at NM-AIST. The University of Dar es Salaam (UDSM) is highly appreciated for allowing me to use their laboratory facilities. My appreciation also goes to Dr. Ophery Ilomo (Head of, the chemistry department, UDSM) for technical assistance to make this study possible. I am also grateful to all individuals who contributed to the accomplishment of my study for their cooperation, friendship, and prayers, which were vital during my study. My sincere gratitude to my wife Calorine Chogo for her patience, and encouragement, also for taking care of our children Lisa, Robinson, Lawrence, and Alphonse during my absence and for their love, and support during my PhD study.

## **DEDICATION**

To my late father

Comrade Andrew Anthony Kapile (R.I.P.)

My beloved children

Lisa, Robinson, Lawrence, and Alphonse

## TABLE OF CONTENTS

ABSTRACT.....	i
DECLARATION.....	ii
COPYRIGHT.....	iii
CERTIFICATION .....	iv
ACKNOWLEDGEMENTS .....	v
DEDICATION .....	vi
LIST OF TABLES .....	xiii
LIST OF FIGURES .....	xii
LIST OF ABBREVIATIONS AND SYMBOLS .....	xv
CHAPTER ONE .....	1
INTRODUCTION .....	1
1.1 Background of the Problem .....	1
1.2 Statement of the Problem.....	3
1.3 Rationale of the Study.....	4
1.4 Research Objectives.....	5
1.4.1 General Objective .....	5
1.4.2 Specific Objectives .....	5
1.5 Research Questions .....	5
1.6 Significance of the Study .....	6
1.7 Delineation of the Study .....	7
CHAPTER TWO .....	8
LITERATURE REVIEW .....	8
2.1 Fossil Fuel Challenges .....	8
2.2 Overview Energy in Africa .....	9
2.3 Sustainable Energy Sources .....	11



2.3.1	Biofuels .....	12
2.3.2	Biodiesel .....	12
2.3.3	Advantages of Biodiesel .....	13
2.3.4	Disadvantages of Biodiesel.....	13
2.4	Feedstock for Biodiesel Synthesis .....	14
2.4.1	Morphological and Botany Description of <i>Adansonia digitata</i> .....	14
2.5	Physicochemical Properties of Oil, Biodiesel, and its Blends .....	15
2.5.1	Iodine Value .....	15
2.5.2	Acidic Value .....	16
2.5.3	Saponification Value .....	17
2.5.4	Free Fatty Acid (FFA) Composition .....	17
2.5.5	Flash Point .....	17
2.5.6	Cetane Number .....	17
2.5.7	Oxidation Stability .....	18
2.5.8	Pour and Cloud Point.....	18
2.5.9	Calorific Value .....	18
2.5.10	Water Content .....	19
2.6	Biodiesel Synthesis by Transesterification Process .....	19
2.6.1	Parameters Affecting Biodiesel Synthesis .....	20
2.7	Nanoparticle Additives.....	22
2.7.1	Physicochemical Properties of Nano-Silica Additives .....	25
2.8	Operation of Compression Ignition (CI) Engine .....	30
2.8.1	Factors Affecting ID Period in CI Engines .....	32
2.8.2	Classification of Combustion Chambers of CI Engine .....	33
2.8.3	Engine Performance, Emission, and Combustion Characteristics.....	34
2.8.4	Health And Environmental Risk of Diesel Engine Exhaust Emissions .....	35

2.8.5	Global Policy Overview .....	35
2.9	Summary .....	36
2.10	Conceptual Framework .....	37
CHAPTER THREE .....		38
MATERIALS AND METHODS .....		38
3.1	Materials .....	38
3.2	Preparation and Characterization of ADSO .....	38
3.2.1	Preparation of ADSO .....	38
3.2.2	Physicochemical Characterization of ADSO and Its Derivatives.....	39
3.3	Preparation and Characterization of Nano-silica Additive .....	45
3.3.1	Nanoparticle Textual Profile .....	47
3.3.2	Thermal Gravimetric Analysis (TGA).....	49
3.3.3	Fourier Transformation Infrared Spectrometry (FT-IR) .....	49
3.3.4	Crystallographic, Morphological, and Elemental Analysis .....	49
3.4	Synthesis of Biodiesel by Transesterification Process.....	50
3.4.1	Optimization of Biodiesel Production .....	50
3.4.2	Determination of Fuel-Related Properties of ADME .....	51
3.4.3	Fat Acid Composition of ADME .....	51
3.5	The Effect of Nano-particle Additives on the Fuel Properties of ADME and its Blends .....	52
3.5.1	Preparation and Physicochemical Properties of Nano-Fuel Blends .....	52
3.6	Engine Performance, Exhaust Emissions, and Combustion Testing .....	53
3.6.1	Engine Test Setup and Procedure.....	53
3.6.2	Engine Performance Characteristics .....	54
3.6.3	Engine Combustion Characteristics .....	57
3.6.4	Exhaust Emission Characteristics .....	58

3.7	Uncertainty Analysis .....	58
CHAPTER FOUR.....		60
RESULTS AND DISCUSSION.....		60
4.1	Characterization of ADSO .....	60
4.2	Optimization of Biodiesel Synthesis.....	61
4.2.1	Effect of Methanol to Oil Molar Ratio on Biodiesel Yield.....	61
4.2.2	Effect of Reaction Time on Biodiesel Yield .....	61
4.2.3	Effect of Reaction Temperature on Biodiesel Yield.....	61
4.3	Physicochemical Properties of ADME .....	63
4.3.1	Composition Profile of FFA in ADME .....	63
4.3.2	Physicochemical Properties of Nano Fuel Blends .....	64
4.4	Physicochemical Properties of Nanoparticle Additives.....	65
4.4.1	The FT-IR Spectral Analysis.....	65
4.4.2	Thermal Gravimetric Analysis of RHS.....	67
4.4.3	Surface Pore and Textural Profile Analysis of RHS.....	68
4.4.4	XRD Spectral Analysis .....	68
4.4.5	Scanning Electron Microscope .....	70
4.4.6	The RHA Elemental Composition Profile .....	72
4.5	Effects of Nano-additive on Fuel Properties of ADME.....	72
4.5.1	Oxidation Stability.....	72
4.5.2	Kinematic Viscosity .....	73
4.5.3	Flash Point .....	73
4.5.4	Cetane Number .....	75
4.5.5	Cloud and Pour Point.....	75
4.6	Comparison of Commercial Alumina and Manufactured Silica Nano-additives on Fuel .....	75

4.6.1	Properties of ADME and its Blends.....	75
4.7	Engine Performance Analysis .....	79
4.7.1	Brake Thermal Efficiency (BTE).....	79
4.7.2	Brake Specific Fuel Consumption .....	80
4.7.3	Exhaust Gas Temperature .....	81
4.8	Engine Combustion Analysis.....	82
4.8.1	In-cylinder Gas Pressure .....	82
4.8.2	Heat Release Rate .....	83
4.8.3	The Mass Rate of Fuel Burnt .....	84
4.8.4	Variation of Crank Angle (CA) for Test Fuels at Minimum and Maximum Brake Power .....	92
4.9	Engine Exhausts Emission Analysis .....	93
4.9.1	Total Hydrocarbon (THC) Emission.....	93
4.9.2	Carbon Monoxide (CO) Emission .....	94
4.9.3	Carbon Dioxide (CO <sub>2</sub> ) Emission .....	96
4.9.4	Oxides of Nitrogen (NO <sub>x</sub> ) Emission .....	97
4.9.5	Particulate Matter (PM) Emission .....	98
CHAPTER FIVE .....		100
CONCLUSION AND RECOMMENDATIONS .....		100
5.1	Conclusion .....	100
5.2	Recommendations.....	101
REFERENCES .....		102
RESEARCH OUTPUTS.....		119

## LIST OF TABLES

Table 1:	Distribution of Africa's oil and natural gas reserves (Rempel, 2023) .....	11
Table 2:	Physicochemical properties of biodiesel and base diesel fuel (Kapile <i>et al.</i> , 2022) .....	16
Table 3:	Test methods and instruments used in the measurement of ADSO and ADME ....	40
Table 4:	Engine specification profile .....	54
Table 5:	Descriptions of instruments used with their accuracy .....	59
Table 6:	Uncertainties in measured parameters .....	59
Table 7:	Physicochemical properties of ADSO .....	60
Table 8:	Physicochemical properties of ADME.....	63
Table 9:	Composition of FFA in ADME by GC-MS analysis.....	64
Table 10:	Physicochemical properties of ADME (ASTM D6751) and its blends (ASTM D7467) .....	65
Table 11:	The RHA elemental composition profile .....	72

## LIST OF FIGURES

Figure 1:	Fossil fuel global primary energy consumption (Ritchie & Roser, 2019).....	9
Figure 2:	Africa fuel's shares of total energy supply in 2014 (Maji <i>et al.</i> , 2019).....	10
Figure 3:	Photographs of a baobab tree and fruit.....	15
Figure 4:	Diesel combustion stages (Choudhary <i>et al.</i> , 2018).....	34
Figure 5:	Conceptual framework of the utilization of nano-silica additives on fuel blends in CI engine.....	37
Figure 6:	Photograph of baobab: (A) fruit (B) fruit pulp (C) seeds (D) seed oil (Chilabade, 2018).....	39
Figure 7:	The GC-MS instrument used for fatty acid composition analysis .....	41
Figure 8:	Viscometer.....	43
Figure 9:	Bomb calorimeter .....	44
Figure 10:	Cloud and pour point tester .....	45
Figure 11:	Schematic diagram of extraction of nano-silica from RHA.....	47
Figure 12:	Photographs of: (a) RH (b) RHA calcined at 650°C (c) RHS .....	47
Figure 13:	Transesterification process .....	50
Figure 14:	Schematic diagram of ultrasound-assisted preparation unit (Gavhane <i>et al.</i> , 2021) .....	53
Figure 15:	Engine: (a) front (b) backward view photograph (c) test rig setup .....	56
Figure 16:	Influence of: (a) methanol to oil ratio (b) reaction time (c) reaction temperature on biodiesel yield.....	62
Figure 17:	The FT- IR spectra of: (a) RHA (b) RHS .....	66
Figure 18:	The RHS thermal decomposition profile between 25 and 800°C .....	68
Figure 19:	The XRD spectra of: (a) RHS (b) RHA .....	70
Figure 20:	The XRD spectrum of pure commercial SiO <sub>2</sub> nanoparticle (Gavhane <i>et al.</i> , 2021) .....	70
Figure 21:	The SEM images of the: (a) RHA (b) RHS.....	71

Figure 22: Influence of nano-SiO <sub>2</sub> additive on: (a) oxidation stability (b) kinematic viscosity (c) flash point (d) CN of ADME .....	74
Figure 23: Effect of commercial and manufactured nano-additives on: (a) oxidation stability, (b) kinematic viscosity, and (c) cetane number .....	77
Figure 24: Effect of commercial and manufactured nano-additives on: (a) oxidation stability (b) kinematic viscosity of B100 and B20 .....	79
Figure 25: Brake thermal efficiency (BTE) as a function of brake power .....	81
Figure 26: Brake specific fuel consumption (BSFC) as a function of brake power .....	82
Figure 27: Exhaust gas temperature (EGT) as a function of brake power.....	82
Figure 28: The variation of: (a) CGP and (b) HRR profile of the test fuels at 0, 4, 8, 12, 16, and 20 kW brake powers .....	91
Figure 29: The mass rate burnt as a function of brake power.....	91
Figure 30: The variation of the crank angle at: (a) minimum and (b) maximum brake power .....	93
Figure 31: Total hydrocarbon (THC) emission as a function of brake power .....	95
Figure 32: Carbon monoxide (CO) emission as a function of brake power .....	96
Figure 33: Carbon dioxide (CO <sub>2</sub> ) emission as a function of brake power.....	97
Figure 34: Oxides of nitrogen (NO <sub>x</sub> ) emission as a function of brake power.....	99
Figure 35: Particulate matter (PM) emission as a function of brake power .....	99

## LIST OF ABBREVIATIONS AND SYMBOLS

$\Theta$	Crank angle
$\Phi$	Equivalence ratio
P	Air density
a	Crank shaft length (m)
%	Percentage
°C	Degree centigrade
ppm	Parts per million
s-SNOM	Scattering-type Scanning Near-Field Optical Microscopy
aTDC	After top dead center
bTDC	Before top dead center
ADME	Adansonia digitata methyl ester
ADSO	Adansonia digitata seed oil
AOAC	American Official for Analytical Chemistry
ASTM	American Society for Testing Measurement
AFM	Atomic Force Microscopy
AV	Acidic value
A/F	Air-fuel ratio
ATR	Attenuated total reflectance
BET	Brunauer Emmett Teller
BJH	Barret Joyner Halenda



BMEP	Brake mean effective pressure
BP	Brake power
BSEC	Brake specific energy consumption
BSFC	Brake specific fuel consumption
BTE	Brake thermal efficiency
BTEs	Budapest University of Technology and Economics
CARB	California Air Resources Board
CGP	Cylinder gas pressure
CI	Compression ignition
CN	Cetane number
CO	Carbon monoxide
CO <sub>2</sub>	Carbon dioxide
DI	Direct injection
DOC	Diesel oxidation catalysts
DPF	Diesel particulate filter
DERA	Diesel Emissions Reduction Act
DUCE	Dar es Salaam University College of Education
EGR	Exhaust gas recirculation
EGT	Exhaust gas temperature
EN	European standards
EOC	End of Combustion

EPA	Environmental Protection Agency
ESIA	Environmental and Social Impact Assessment (ESIA)
FAAE	Fatty Acid Alkyl Ester
FAEE	Fatty acid ethyl ester
FAME	Fatty acid methyl ester
FFA	Free fatty acid
FID	Flame Ionization Detection
FTIR	Fourier transforms infrared spectroscopy
GC-MS	Gas chromatography-mass spectrometry
GHG	Greenhouse gas
GO	Graphene oxide
HRR	Heat release rate
ICE	Internal combustion engine
ID	Ignition Delay
IR	Infra-Red Radiation
IV	Iodine value
LHV	Lower Heating Value
MEWES	Materials Energy Water and Environment Science
MoEST	Ministry of Education Science and Technology
NM-AIST	Nelson Mandela African Institution of Science and Technology
NO <sub>x</sub>	Oxides of nitrogen

OIP	Oxidation induction period
PAHs	Polycyclic aromatic hydrocarbons
PCDDF	Polychlorinated dibenzo-p-dioxins/dibenzofuran
PM	Particulate Matters
POME	Palm oil methyl ester
RH	Rice Husk
RHA	Rice Husk Ash
RHS	Rice Husk Silica
RIPI	Research Institute of Petroleum Industry
SBME	Soybean methyl ester
SCR	Selective Catalytic Reduction
SI	Spark ignition
SOC	Start of combustion
SOI	Start of injection
STP	Standard Temperature and Pressure
SV	Saponification value
TERS	Tip-Enhanced Raman Spectroscopy
THC	Total hydrocarbon
UDOM	University of Dodoma
UDSM	University of Dar es Salaam
UHC	Unburn hydrocarbon

USD

United state dollar

## CHAPTER ONE

### INTRODUCTION

#### 1.1 Background of the Problem

Biodiesel is becoming increasingly popular worldwide. Greenhouse gas (GHG) emissions and climate change remain significant concerns, driving the need for renewable and sustainable energy sources and the development of local, secure fuel supplies. One promising alternative fuel that has emerged is biodiesel, known for its renewable nature, biodegradability, cost-effectiveness in raw material acquisition, ease of manufacturing, lower emissions, and similar fuel qualities to conventional diesel.

The fatty acid alkyl esters (FAAE) in biodiesel are determined by the alcohol used in the transesterification process and are produced from animal fats and plant oils (Syafiuddin *et al.*, 2020).

Depending on where its feedstock comes from, it is separated into three generations. The production of first-generation biodiesel from edible oils and food crops strains available land and food supplies. There is no impact on food supply and security from the manufacturing of second-generation biodiesel because it uses non-edible oils and non-food crops. However, there is still a problem with the demand for fresh water and land. The third-generation or new biodiesel is derived from microbial or algae oil and does not require much land or freshwater (Bhuiya *et al.*, 2016). However, there is still a problem with the demand for fresh water and land (Gajraj *et al.*, 2018).

In the current, study, biodiesel was produced from the baobab plant (*Adansonia digitata*) seed oil (ADSO). It belongs to the Bombacaceae family. It is a non-edible biodiesel feedstock (second generation). It is sometimes known as the Bombax or Kapok family (Mohammed, 2018). The *Adansonia* genus contains eight species of the African baobab, often known as the dead rat tree or monkey bread tree, It is an unusually planted, medium-sized deciduous tree (Mohammed, 2018). Baobab trees, which are native to equatorial Africa, have bizarrely inflated trunks. It is large, with barrel-shaped trunks. They can grow to 9 m in diameter, and only a few trees can grow to 25 m tall (Kamatou *et al.*, 2011).

Biodiesel can be produced and blended before being used in a compression ignition (CI) engine. However, there are several drawbacks to using biodiesel in CI engines, including a 10% drop in fuel efficiency on an energy basis, greater density, a lower degree of fuel atomization, lower cloud and pour points, piston ring sticking, increased NO<sub>x</sub> emissions, and cold starting issues (Hoang, 2021). Several researchers have examined methods to enhance engine performance, exhaust emissions, and combustion characteristics. These methods include exhaust gas recirculation (EGR), emulsification, low-temperature combustion, selective catalytic reduction (SCR), diesel oxidation catalyst (DOC), diesel particulate filter (DPF), lean nitrogen traps, and fuel treatments (Hoseini *et al.*, 2017).

Many studies have shown that adding nanoparticles to biodiesel can enhance its thermophysical characteristics, such as mass diffusivity, thermal conductivity, and surface area-to-volume ratio. These can then lead to an improvement in the biofuels' physical and chemical characteristics, such as oxidation stability, kinematic viscosity, flash point, cloud point, and pour point. Enhanced biodiesel fuel properties improve engine performance, exhaust emissions, and combustion characteristics (Hoseini *et al.*, 2017).

The diesel engine is an internal combustion engine in which the raised temperature of the air in the cylinder induced by mechanical compression causes fuel ignition; thus, the diesel engine is a compression-ignition (CI) engine. This is in contrast to engines that use spark plugs to ignite the air-fuel mixture, such as a petrol engine or a gas engine (using a gaseous fuel like natural gas or liquefied petroleum gas) (Heywood, 2018). Diesel engines operate by compressing either air or air plus residual combustion gases from the exhaust gas recirculation (EGR). During the intake stroke, the air is drawn into the chamber and compressed during the compression stroke. This raises the temperature of the air inside the cylinder to the point where atomized diesel fuel injected into the combustion chamber ignites. When fuel is injected into the air right before burning, the fuel disperses unevenly, resulting in a heterogeneous air-fuel combination. The torque produced by an engine is governed by adjusting the air-fuel ratio rather than restricting the intake of air, the diesel engine relies on adjusting the amount of fuel injected, and the air-fuel ratio is often high (Pandey & Sharma, 2021).

Currently, researchers focus on the use of metal oxide nanoparticles to improve fuel quality, by acting as oxygen donors to reduce THC and CO emissions. In general, from the literature reviews metal oxides have mechanical properties due to large surface area to volume ratio. It releases electron pairs in the polymer matrix resulting in improved adhesion interaction, resists

abrasion, and hinders free radical movement. At elevated temperatures, it increases surface conductivity between the fuel matrix and air molecules during gas adsorption and desorption (Cuong & Quang, 2020). Therefore, it enhances combustion enthalpies, more quick oxidation, shorter ignition delays (ID), lower melting point, higher ignition temperature, enhanced high heat per mass transfer rates, and reduces pollutant emissions (Saxena *et al.*, 2017; Kapile *et al.*, 2022).

Since RH is almost 100% pure in its amorphous phase and contains 87–97% SiO<sub>2</sub> with traces of alkali and other elements, it is a potential source for this study. Using a simple reaction method through the calcination process results in better SiO<sub>2</sub> extraction from RH as it recovers the product easily, cost-effectively, and efficiently (Prasad *et al.*, 2003). The influence of nanoparticles on CI engine performance can also be improved by varying operating parameters such as load, engine speed, and blending ratio to enhance the overall air-fuel mixture, vortex, and turbulence characteristics. It prevents the deposition of carbon and iron, thereby reducing engine friction (Hoseini *et al.*, 2020). Moreover, fuel additive reduces BSFC, improve BTE, increase brake power (BP), and reduce emissions (Gavhane *et al.*, 2021).

In general, due to its mechanical, thermal, and electrical properties, fuel additives have recently been offered as the most viable solution for improving fuel qualities for larger blending ratios. However, the use of these additives is limited by their toxicity, fuel blend properties, and economic feasibility due to their rapid evaporation and longer ID. The nano-silica additive is economically feasible and less toxic because it was extracted from RH as agricultural waste to increase its value instead of being burned to increase environmental pollution (Kapile *et al.*, 2022). Therefore, this study focuses on the use of SiO<sub>2</sub> nanoparticles which have not been more commonly researched previously as biodiesel additive. The impacts of nanoparticles on performance, emissions, and combustion characteristics in CI diesel engines were investigated comprehensively.

## **1.2 Statement of the Problem**

The chemical structure of fatty acids in plant oil limits the range of properties attainable by the biodiesel produced by the transesterification process. In this context, improving biodiesel's properties to meet global standards, such as the ASTM D6751, and EN14214 is an ongoing research area. The present study investigates novel and low-cost nano-silica additives calcined from agricultural waste (rice husks) to improve the fuel properties of biodiesel made from

ADSO. Most of the reported nanoparticle additives for improving biodiesel's properties are derived from non-renewable resources that are economically and environmentally unsustainable. The Sol-Gel process is a well-known synthetic method for producing unique metal oxide nanoparticles as well as mixed oxide composites. This process involves high production costs which hinders its utilization and commercialization since it takes a long period for processing, difficulty related to phase separation, and contamination of toxic heavy metals. Therefore, the main focus of this study is to make low-cost nano-silica additives from abundant rice husks using a simpler reaction method than the Sol-Gel method. It has a high reactivity index containing silica of about 87–97% with a small amount of alkali and other trace elements. The study also intends to increase the value of rice husk as an agricultural waste instead of being burned to enhance pollution. The ADME and its blends were therefore doped with the nano-silica by ultrasonication process to investigate how it influences fuel-related properties including flash points, kinematic viscosity, CN, and oxidation stability which are predominant factors in engine operation. The study explores further utilization of this nano additive on the operational efficiency and characteristics parameters of a CI diesel engine. Since it improves atomization, shortens ID, and reduces emissions.

### **1.3 The rationale of the Study**

This research investigated the influence of nano-silica additives on the potential fuel-related properties of ADME at different concentrations (400, 600, 800, and 1000 ppm). Silica nanoparticles were extracted from the rice husks by a simple chemical reaction. The current study also explores details on the production of ADME from ADSO through a transesterification process. Moreover, the study explores the physicochemical properties of ADSO and ADME such as acidic value, kinematic viscosity, iodine value, flash point, density, CN, oxidation stability, and calorific value. Manufactured SiO<sub>2</sub> nano-particle additives were characterized for physicochemical properties by using SEM, XRD, XRF, FT-IR, BET, and BJH.

Furthermore, this study focuses on the influence of SiO<sub>2</sub> nanoparticle additives on the performance (e.g. BTE, BSFC, EGT), combustion (CGP, HRR, mass rate burnt), and exhaust emission (CO, THC, CO<sub>2</sub>, NO<sub>x</sub>, and PM) characteristics of CI engine fueled with ADME (B100) and its blends (B20, B20+SiO<sub>2</sub>, and B100+SiO<sub>2</sub>) in comparison with the neat conventional diesel (B0). In addition, the current study helps to remind Tanzania's energy policymakers to contribute to a long-term sustainable energy plan. The results can therefore be used as a starting point for the development of national guidelines for the environmental impact



assessment of the use of conventional fuels on climate change and the health risks associated with GHG. The results are also a potential aid to all energy technology stakeholders to promote sustainable development in Tanzania.

## **1.4 Research Objectives**

### **1.4.1 General Objective**

To experimentally investigate the influence of nano-silica additives extracted from agricultural waste (rice husk) on the fuel properties of ADME and its impact on engine performance, exhaust emissions, and combustion characteristics.

### **1.4.2 Specific Objectives**

The following were the specific objectives of this study:

- (i) To establish the physicochemical properties of *Adansonia digitata* Seed Oil (ADSO) and *Adansonia digitata* Methyl Ester (ADME).
- (ii) To analyze the physicochemical properties of nano-silica additive extracted from the rice husk (agricultural waste).
- (iii) To investigate the influence of synthesized nano-silica additives on the fuel-related properties of ADME at different concentrations.
- (iv) To evaluate the performance, exhaust emissions, and combustion characteristics of a CI diesel engine fueled with ADME and its blends doped with nano-silica additive.

## **1.5 Research Questions**

The study intended to answer the following questions:

- (i) What is the potential of ADSO in the production of biodiesel?
- (ii) How effective is the silica extracted from rice husk as a basic nano-additive used for modifying the fuel-related properties of ADME?
- (iii) How closely do the fuel characteristics of the biodiesel produced from ADSO doped with nano-silica additives match the guideline of the worldwide biodiesel standard?

- (iv) What is the influence of nano-silica additives on the performance, exhaust emissions, and combustion characteristics of ADME and its blends in the CI engine?

## **1.6 Significance of the Study**

The impact of this research has a significant contribution to understanding the specific needs of the renewable energy sector and the implications on the policy-making organization in Tanzania to avoid climate change and global catastrophes. Findings and recommendations in this study can also be used by stakeholders in planning for investment in more sustainable and renewable energy resources. To promote public health awareness and sustainable policy-making energy industry. Because of the issues with pollution to the environment, depletion, and increased cost of petroleum fuels, biodiesel has emerged as a possible substitute fuel in the modern world since petroleum diesel is a nonrenewable resource and causes global warming due to increased GHG. Compared to modern engine fuels, biodiesel requires less modification, is a renewable, biodegradable energy source, and emits fewer exhaust emissions. This study will contribute to considerably sustainable and environmentally friendly biodiesel production to enhance its commercialization.

On the other hand, nanoparticles have a relatively large surface-area-to-volume ratio, making them ideal catalysts. The nanoparticles dispersed throughout the fuel facilitate better air-to-fuel mixing and enhance chemical reactivity during combustion, leading to better performance, combustion, and reduction of emissions. Nanoparticles, due to their diminutive size (less than 100 nm in diameter) and lower required quantities, offer significant advantages in various applications, including enhanced catalytic activity and reduced resource consumption. The lattice structure of SiO<sub>2</sub> nano-additive donates an oxygen molecule to carbon at a lower temperature and pressure than normal combustion. This oxidation reaction allows for the decomposition of THC and soot, thereby reducing the volume of pollutants released and the amount of fuel used. The lower pressure in the combustion chamber also reduces the production of NO<sub>x</sub> and makes combustion more efficient. Therefore, this study enhances awareness on improving engine life span, public health hazard awareness on pollution of GHG, low-cost production of nano-additives, improving the value of agricultural waste, and increasing utilization and commercialization of biodiesel as alternative energy to replace fossil fuel.

## **1.7 Delineation of the Study**

This dissertation is divided into five chapters; Chapter One discusses background information on the statement of the research problem, the rationale of the study, objectives, research questions, significance, and delineation of the study. This chapter explores in detail definitions and the significance of using nano-silica additives to improve fuel properties and engine performance. The literature review in Chapter Two covers important topics related to the *A. digitata* plant, biodiesel, and its production processes. It also discusses how operating parameters during the biodiesel synthesis process affect production efficiency. Influence of nano-silica additives on performance and emission criteria on a diesel engine. Chapter Three presents material and methods which cover detail on analytical techniques and the experimental procedure followed in this study. Chapter Four presents the results and discussion of the physicochemical properties of nanoparticles and biodiesel, the impact of nanoparticles on ADME's possible fuel qualities finally evaluation of the performance, emissions, and combustion characteristics of ADME and its blends fueled in a diesel engine. Chapter Five presents the conclusions and recommendations which provide detail on scientific and knowledge contributions for future energy planning and research.

## CHAPTER TWO

### LITERATURE REVIEW

#### 2.1 Fossil Fuel Challenges

The most widely used energy source is petroleum products. In 2017, 80.7% of the world's energy came from fossil fuels, according to the World Bank report of 2017. The distribution of sources, including coal, crude oil, and natural gas, was examined by Ritchie & Roser (2019) as shown in Fig. 2. The US Department of Energy looked into annual global fossil fuel-related CO<sub>2</sub> emissions. Fossil fuel usage was 9776 million metric tons (Masera, 2019). Additional issues associated with fossil fuels include resource depletion and supply security. The literature cautions regarding the limited availability of fossil fuels.

For instance, a research study by Masera (2019) reported that the reserves of coal, natural gas, and crude oil will be depleted in 35, 37, and 107 years, respectively. The issue of fossil fuel depletion was reported in this kind of study, despite the dates being simply estimates. One of the main causes of GHG emissions and consequently health risks for humans has been identified as the burning of fossil fuels in diesel engines (Campbell-Lendrum & Prüss-Ustün, 2019).

The direct immediate impact of cancer on human health is caused by exhaust gas emissions like soot and NO<sub>x</sub>, especially in the respiratory and cardiovascular systems. About 73–83% of particulate matter (PM) is caused by carbon soot from diesel engines (Masera *et al.*, 2021). Soot also contains sulphur compounds, soluble organic compounds, ash, trace elements, and other pollutants such as polychlorinated dibenzo-p-dioxins/dibenzofuran (PCDDF) and polycyclic aromatic hydrocarbon (PAH) (Tomašek *et al.*, 2021). Exposure to NO<sub>x</sub> emissions and PM, their chance of developing respiratory, cardiovascular, and lung cancer increases. In the United Kingdom, the Health Protection Agency reported that GHG in the atmosphere has been linked to 11 900 premature deaths (Vardoulakis & Heaviside, 2012). In conclusion, it is generally accepted that the problems caused by fossil fuels should be addressed first with alternative solutions.

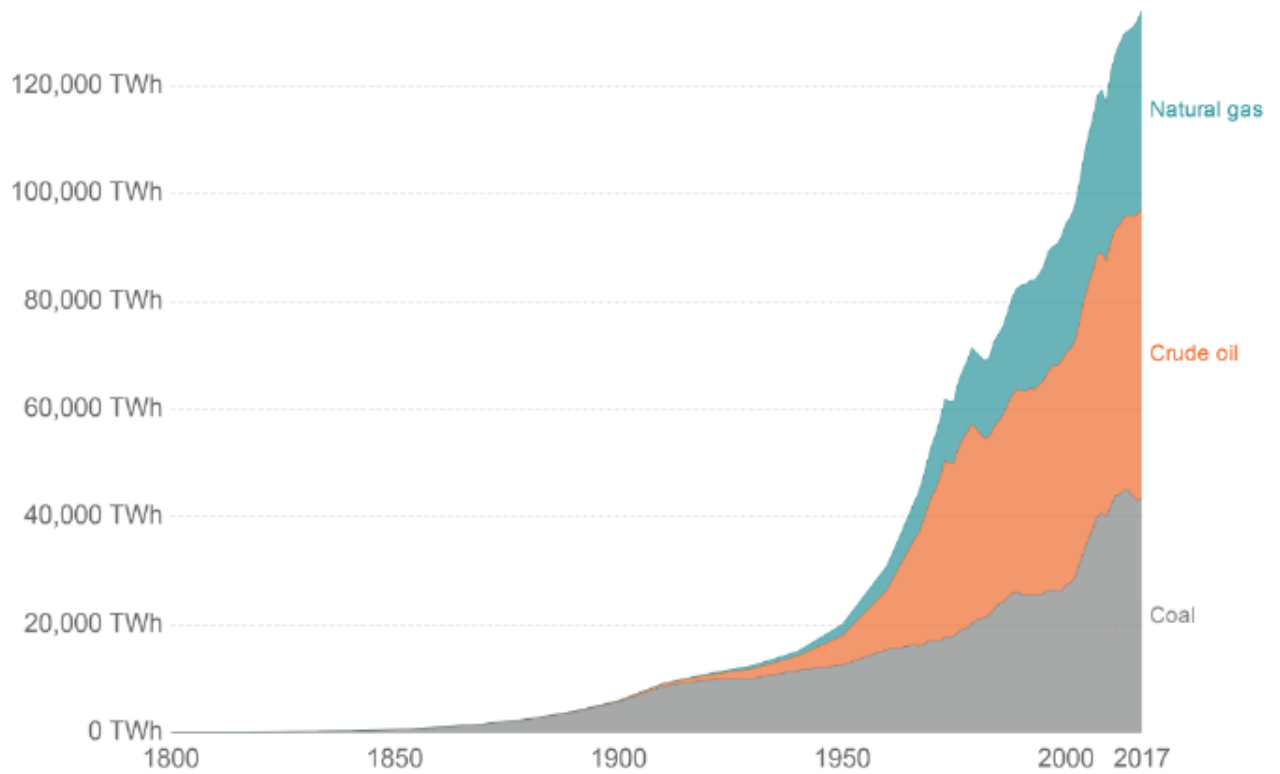


**Figure 1: Fossil fuel global primary energy consumption (Ritchie & Roser, 2019)**

## 2.2 Overview Energy in Africa

Africa has a variety of energy sources, including hydropower, solar electricity, wind, biomass, coal, oil, and natural gas (Chitiga *et al.*, 2008; Kazimierczuk, 2019). The most important energy source among these is traditional biomass like crop leftovers and firewood. As shown in Fig. 2, biomass supplied almost 48% of the continent's primary energy in 2014. The remaining sources were natural gas, oil, and coal, which contributed 14, 21, and 15% respectively of the total (Schulz *et al.*, 2016; Hafner, 2021). Hydropower resources also provide a significant quantity of energy. However, Africa now uses relatively little non-traditional energy, such as geothermal, wind, and solar power. Because of cleanliness, no carbon emissions, and by doing so, the environmental harm caused by mining or drilling for fossil fuels is avoided. The literature's findings showed that Africa has a high potential for biomass because of the continent's abundance of land, and the high cost of fossil fuels. Energy insecurity is one of the main issues facing Africa. More than 69% of people in Africa relied on traditional biomass in 2014 to meet their needs for heating and cooking at home (Winkler, 2007).

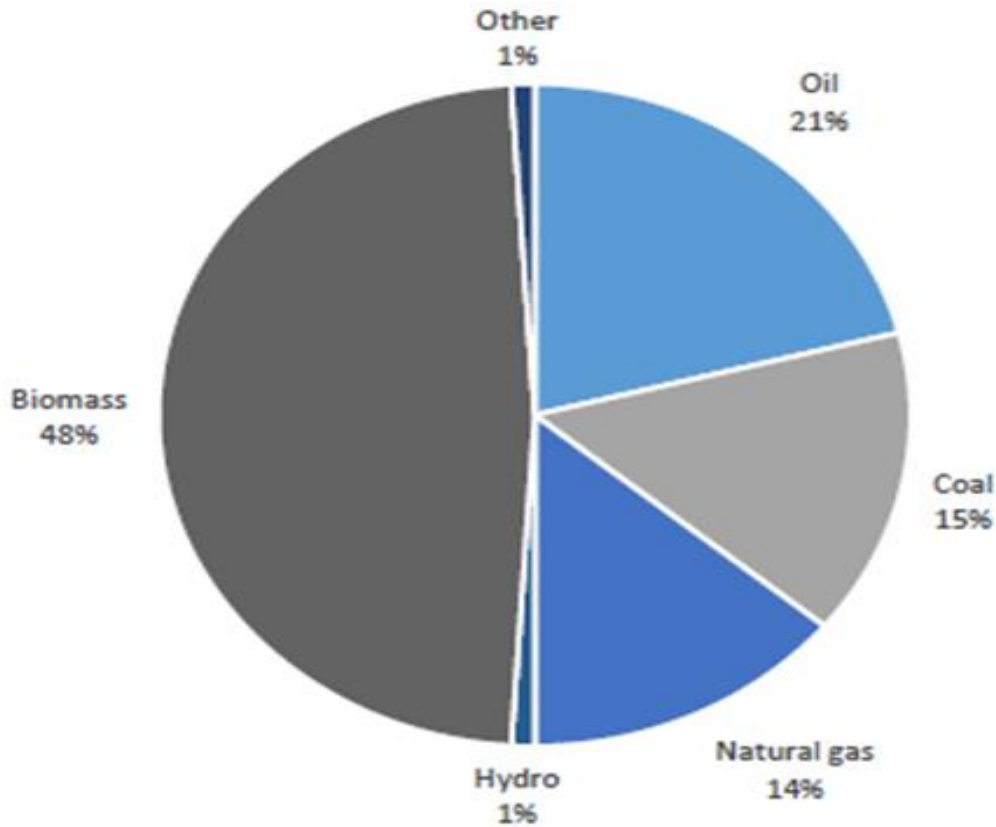


**Figure 2: Africa fuel's shares of total energy supply in 2014 (Maji *et al.*, 2019)**

Another factor causing energy instability in Africa is the unequal distribution of fossil fuel reserves (Amineh & Yang, 2018). Africa possesses global reserves of about 7.6, 3.6, and 7.5% of oil, coal, and natural gas, respectively. Table 1 shows that approximately 45% of the continent's total oil reserves are found in North Africa, West Africa contains about 32%, and Southern, East, and Central Africa have 23% (Alemzero *et al.*, 2021). The previous report reveals that the North and West African areas hold about 51 and 35% respectively of all available natural gas. Furthermore, South Africa alone contains around 95% of Africa's coal reserves (Rempel, 2023). Since fossil fuel sources are distributed unevenly, more than 70% of African countries are net importers of energy. Dependence on foreign energy has an impact on the availability and affordability of energy sources in the societies (Musoni, 2018).

**Table 1: Distribution of Africa's oil and natural gas reserves (Rempel, 2023)**

Places	Oil (%)	Natural gas (%)
North Africa	45%	51%
East Africa	4%	1%
Central Africa	7%	2%
Southern Africa	12%	11%
West Africa	32%	35%

### **2.3 Sustainable Energy Sources**

The European Union set goals by 2020 and 2030, to mitigate GHG emissions by 24 and 32%, respectively, compared to 1990 levels, through the use of alternative sources to replace fossil fuel (Westphal, 2016; Oztig, 2017). Member countries were given until 2020 to meet a 10% biodiesel mandate for transportation fuels. The Department for Transport in the United Kingdom by 2032, has implemented a minimum objective of 12.4% utilization of biofuel volume fraction in transportation (Masera, 2019). To reach their emission targets, some nations additionally promote the use of renewable energy through subsidies, tax breaks, and other incentives.

In Tanzania utilization of liquid biofuel is still rare however, it encourages investment in renewable energy by imposing incentives such as tax exemption. For environmental impact assessment, The National Environment Management Act of 2004 requires biofuel investors/developers to conduct an Environmental and Social Impact Assessment (ESIA) and an Environmental Audit which addressed that, ESIA must include the sustainability requirements. Following the start of the project, a biofuels investor or developer may be obliged to conduct an Occupational Health and Safety Assessment (Eshton & Katima, 2015). According to the Department of Energy and Climate Change report of 2012, the tighter emission limitations and targets will therefore likely result in an increase in the total demand for bioenergy. The International Renewable Energy Agency report of 2017 states that renewable energy can cut global CO<sub>2</sub> emissions by 44% in 2050.

### **2.3.1 Biofuels**

Biofuel refers to any fuel made from biomass in the form of liquid, gaseous, or solid (Singh & Nigam, 2018). Biodiesel, bioethanol, and biogas are examples of biofuels. Biofuels are becoming increasingly popular around the world, owing to the environmental benefits they provide. Biofuels are regarded as environmentally benign because they are biodegradable and renewable. Since it creates jobs, the expansion of the biofuels sector is thought to be a major factor in the decline of poverty in developing countries (Varela-Pérez *et al.*, 2022).

### **2.3.2 Biodiesel**

One of the most significant liquid biofuels now in use is biodiesel. Table 2 illustrates some of the physical and chemical similarities between fossil diesel and biodiesel. As a result, biodiesel is widely regarded as the most viable option to replace conventional petroleum diesel (Srivastava *et al.*, 2018).

Conventional diesel engines may run on biodiesel without requiring major engine modification because of the fuel's similar properties. It is a fuel that is frequently used for transportation, as well as for producing heat and power (Chilabade, 2018). Moreover, any ratio of biodiesel to petroleum diesel may be used to produce a biodiesel-diesel blend. It is a potential oxygenated fuel derived from natural and renewable resources. It is made up of mono-alkyl esters of long-chain fatty acids that are produced from sustainable feedstocks. Being biodegradable, non-toxic fuel burns rather clean, thus why it is being researched as a possible replacement for traditional, more polluting petroleum fuels. Biodiesel, whether used on its own or blended with petroleum diesel, can lower certain exhaust emissions compared to diesel made from petroleum. The specific type of biofuel and its proportion in the mixture with petroleum diesel influence the extent of these reductions. Additionally, it does not contribute to an increase in GHG levels in the atmosphere (Kweku *et al.*, 2018).

In terms of aromatic concentration and biodegradability, biodiesel is better than diesel. A substantial oil yield from any feedstock is essential for achieving large-scale production at reduced costs (Staples *et al.*, 2018). Biodiesel can be utilized independently or blended with diesel fuel to reduce exhaust gas emissions. However, the elevated viscosity of biodiesel results in larger droplet sizes, inadequate vaporization, and a limited injection spray angle. Fuel density is also a significant characteristic since injection systems measure fuel by volume, and so changes in density owing to varying injected fuel masses influence engine output power



(Siddique *et al.*, 2021). But fuel with less energy content causes engines to run slower and produce less power. Moreover, diesel-biodiesel blends have been the focus of numerous investigations since they are believed to be a viable fuel at low blending ratios such as B20 (Maroa & Inambao, 2021).

The search for alternative energy is currently being driven by concerns about environmental regulations. The use of mixed biodiesel-diesel fuel has emerged as a viable option globally, but one that is restricted to modest blending ratios (up to 20%, or B20). The most practical way to enhance engine performance, emission and combustion characteristics, and fuel and blend quality has been suggested to be through the use of fuel additives. The physicochemical characteristics of baseline diesel fuel and biodiesel, as determined by ASTM D6751 and EN 14214 standard limits, are shown in Table 2. However, because of their toxicity, economic viability, and blended fuels' physicochemical characteristics, their use is limited (Imdadul *et al.*, 2017; Razak *et al.*, 2021).

### **2.3.3 Advantages of Biodiesel**

The main advantage of biodiesel is that be produced locally from renewable resources. According to the findings reported that it is biodegradable, and also environmentally friendly (Rozina *et al.*, 2022). Furthermore, biodiesel has lower PM, THC, CO, and SO<sub>2</sub> emission profiles. Using biodiesel instead of fossil diesel according to the study by Helwani *et al.* (2009), reduces CO, PM, and UHC emissions by 46.7, 66.7, and 45.2% respectively. Also, it is safer to handle, store, and transport than fossil diesel since biodiesel is non-flammable (Mishra & Goswami, 2018).

### **2.3.4 Disadvantages of Biodiesel**

According to the Environmental Protection Agency (EPA) assessment report of 2002, biodiesel produces more NO<sub>x</sub> than fossil diesel, while being regarded as a clean fuel. In the previous report observed by Verma *et al.* (2019), biodiesel has the potential to raise NO<sub>x</sub> emission, based on findings, B20, B40, and B60 seemed to release about 3 to 4%, 4 to 6%, and 6 to 9% more than petroleum diesel, respectively. Since biodiesel is more viscous than petroleum diesel, fuel pumping can be challenging as a result, when biodiesel is utilized as fuel, fuel consumption increases (Syafiuddin *et al.*, 2020). Studies reported that due to its poor cold-flow property, at low temperatures, it tends to crystallize or thicken which can compromise operating issues such as tube and filter obstruction. Biodiesel is also very prone to auto-oxidative breakdown, which

has an impact on storability and engine performance (Mahmud *et al.*, 2022). Furthermore, it was observed that using biodiesel as a fuel causes greater corrosion of copper and brass, severe engine wear, and decreased engine speed and brake power (Thangarasu *et al.*, 2019).

## **2.4 Feedstock for Biodiesel Synthesis**

Biodiesel is a chemical combination of fatty acid alkyl esters (FAAE) produced from lipids or oil. The majority (>90%) of lipids required to make biodiesel are also found in the human diet. Crops including, sunflower, rapeseed, and soybean are key sources of feedstock for the synthesis of biodiesel (Rezania *et al.*, 2019). This is a significant barrier to the utilization and commercialization of biodiesel since diverting food products used to produce fuel is considered unethical. The biodiesel derived from edible food-grade components may contribute to rising food inflation and insecurity (Kaimal *et al.*, 2022). Additionally, the high price of edible vegetable oils drives up the cost of producing biodiesel, reducing its economic viability when compared to diesel fuel obtained from fossil fuels. The use of low-value lipids in place of edible oils is one solution to the aforementioned problems. Similarly, biodiesel is made from edible plant oils from species like *Jatropha curcas*, *Pongamia pinnata*, and *Azadirachta indica* (Kirubakaran & Selvan, 2018). Grease, animal fats, microbial oils, and used frying oil are all being researched as potential feedstocks. Africa has a variety of non-edible plant seed oils that can be utilized as raw materials to produce biodiesel because they have no commercial value such as *Adansonia digitata* (baobab) oil.

### **2.4.1 Morphological and Botany Description of *Adansonia digitata***

*Adansonia digitata* trees are members of the Malvaceae family and the genus of *Adansonia*. It is also known as the baobab tree, the monkey bread tree, and the upside-down tree. As displayed in Fig. 3, it is enormous, growing to a height of 23 m or more, making it stand out in the natural world. It is identified by its swollen trunk and short, which, depending on the maturity of the tree, can have a conical, cylindrical, or bottle-shaped form (Chilabade, 2018).



**Figure 3: Photographs of a baobab tree and fruit**

## **2.5 Physicochemical Properties of Oil, Biodiesel, and its Blends**

The measure for the quality of fuel to be produced is the physicochemical characteristics of the oil, biodiesel, and blends that determine the engine's operational characteristics. Water content, oil, density, kinematic viscosity, FFA composition, saponification value, acid value, iodine value, and oxidation stability are potential parameters to be analyzed. Table 2 displays the physicochemical properties of biodiesel and base conventional diesel as per global ASTM and EN standard limits.

### **2.5.1 Iodine Value**

The iodine value (IV) of the oil is used to quantify its overall unsaturated characteristic. The amount of iodine, required to react with the double bonds when 100 g of oil is added. The

quantity of double bonds in that molecule controls the unsaturation characteristic of the oil. An excellent illustration is unsaturated linoleic acid with two double bonds and eighteen carbon atoms (C:18). During the titration process, the amount of iodine consumed also establishes the oil's unsaturated fatty acid content and serves as a gauge for the stability of the oil's oxidation stability. A high iodine level suggests that the oil contains more C=C, which will have an impact on engine performance (Soares *et al.*, 2017).

**Table 2: Physicochemical properties of biodiesel and base diesel fuel (Kapile *et al.*, 2022)**

Properties	ASTM D6751 limits	EN 14214 limits	Diesel
Kinematic viscosity at 40°C (mm <sup>2</sup> /s)	1.9 – 6.0	3.5 - 5.0	2.0 - 4.5
Density at 15°C (kg/m <sup>3</sup> )	860 - 900	860 - 900	850
Cetane number (minimum)	>47	>51	54.6
Cloud point (°C)	-3 - 12	-	-15 to -5
Pour point (°C)	-15 - 10	-	-35 to -15
Flash point (°C)	>130	>101	60 - 80
Iodine number (gI <sub>2</sub> /100g)	60 - 135	-	-
Acidic number (mg KOH/g)	0.8 max	-	-
Calorific value (MJ/kg)	42 - 46	-	45
Oxidation stability at 110°C (h)	>6	>3	-

### 2.5.2 Acidic Value

The acidic value (AV) of the oil or fats indicates the quantity of free fatty acids present. The amount of KOH, measured in milligrams, required to neutralize the organic acids included in one gram of fat or oil. It is one of the fundamental characteristics of fats and oils. Generally, the formation of soap during transesterification is encouraged by the oil's high AV. High AV feedstock and the alkali catalyst react right away to produce soap. For this case, two steps esterification and transesterification are required. Moreover, the high AV of biodiesel blends has been observed to cause fuelling system deposits and may increase the chance of corrosion (Reddy *et al.*, 2016).

### **2.5.3 Saponification Value**

The saponification value (SV) is another crucial component of the oil. It is the milligrams of KOH or NaOH needed, under specific conditions, to saponify one gram of lipids or oil. It quantifies the amount of esterified and free acids found in lipids and fatty acids. This characteristic shows whether or not the oil or fats can be used to form soap. Therefore, a higher SV implies a higher AV and a greater chance of soap formation (Reddy *et al.*, 2016).

### **2.5.4 Free Fatty Acid (FFA) composition**

The primary factor influencing the physicochemical characteristics of the biodiesel produced is its FFA composition. It impacts biodiesel's oxidation stability, density, AV, heat of combustion, lubricity, and kinematic viscosity, according to Mohammed (2018). These characteristics are impacted by a chemical composition including the carbon chain length, and the distribution of atoms within the compound. The saturation and unsaturation levels are determined by the number of single and double bonds respectively. Depending on the source of feedstock, different carbon chains have different lengths which may affect the entire stability of biodiesel produced. An esterification reaction with an acid catalyst can be employed to manage excess FFA before base-catalyzed transesterification, based on the commercial processing industry. Therefore, the component of FFA alters the quality of biodiesel fuel and hence affects the overall engine performance (Aldhaidhawi *et al.*, 2017; Mohammed, 2018).

### **2.5.5 Flash Point**

The lowest temperature, at which an ignition source ignites the fuel blends and vaporizes biodiesel under 101.3 kPa (760 mmHg) condition. The tendency of fuel volatility is reflected in its flash point. This is the lowest temperature at which a volatile material will evaporate and combine with air to create an ignitable combination. The volatility decreases as the flash point increases (Kapile *et al.*, 2022).

### **2.5.6 Cetane Number**

The measure of biodiesel fuel ignition quality and determination of combustion roughness is known as cetane number. It depends on engine size, design, load fluctuations, and the nature of speed as well as starting and ambient conditions. An elevation in the cetane number (CN) beyond the specified threshold does not significantly enhance engine performance.

Consequently, it is advisable to maintain the required CN at the lowest possible level to optimize fuel availability (Alrefaai *et al.*, 2018).

### **2.5.7 Oxidation Stability**

Oxidation stability indicates the capacity of biodiesel to withstand oxidation over long periods of storage. Fuel chemical structure promotes oxidation, which results in gum formation and fuel deterioration (Atabani *et al.*, 2019). Biodiesel that has significant levels of oleic, linolenic, or linoleic acid in it is more prone to oxidation. An increased concentration of unsaturated free fatty acid (FFA) chains in oil enhances the propensity for oxidation through reactions with atmospheric oxygen (Atabani *et al.*, 2019). Additionally, elevated temperatures and the presence of reactive metal contaminants in methyl esters further contribute to the oxidation process.

### **2.5.8 Pour and Cloud Point**

These are the essential tests for fuels in cold climates that will enable you to continue operating your vehicle throughout the winter. The cloud point of a liquid sample is defined as the temperature at which the initial formation of the smallest detectable aggregation of wax crystals occurs following cooling under specific conditions. Conversely, the pour point refers to the minimum temperature at which a fuel, when subjected to specified testing conditions, is unable to flow freely through a filter (Chhabra *et al.*, 2021).

### **2.5.9 Calorific Value**

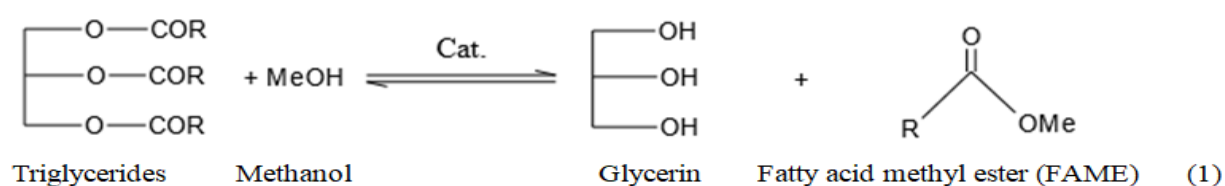
The calorific value is the amount of heat energy present in the fuel that is determined by the complete combustion of a defined quantity at constant pressure and under normal conditions. The calorific value of fuel determines its efficiency. If the value is high, the efficiency will be high as well. If the value is low, the efficiency decreases. It is important to understand the calorific value of fuel to carry out daily activities. This information plays a role in calculating the quantity of energy consumed. Fuel shippers and suppliers require this information to bill gas customers. It also helps in determining the transportation costs of fuel shippers and suppliers.

### 2.5.10 Water Content

It is crucial precautions to assess the engine quality performance and procurement of the fuels, therefore, it is imperative to know the water content of the fuel or oil while it is being manufactured, purchased, or transferred. It has an adverse influence on engine life span since it can cause corrosion more readily when there is water present.

## 2.6 Biodiesel Synthesis by Transesterification Process

The most well-liked and frequently employed technique for making biodiesel is the transesterification process. In this process, homogeneous or heterogeneous catalysts can be employed to separate the oil into biodiesel and glycerin, potentially simplifying and speeding up the synthesis process (Najeeb *et al.*, 2021).



This process entails the interaction of triglycerides with alcohol, particularly ethanol or methanol, facilitated by the presence of a catalyst, which may be an alkali, acid, or enzyme, among other options, to yield fatty acid alkyl esters. In this reaction, potassium hydroxide (KOH) or sodium hydroxide (NaOH) dissolved in alcohol is commonly employed as a catalyst (Moazeni *et al.*, 2019). Fatty acid ethyl ester (FAEE) is a byproduct of using ethanol. Glycerin and FAME, or biodiesel, are the products of the reaction. Methanol can also be substituted with ethanol for alcohol to produce FAME (Moazeni *et al.*, 2019).

According to the findings, methyl esters are the most widely used commercial product and methanol is substantially less expensive than ethanol, methyl ester synthesis was preferred over ethyl ester production (Jayaraman *et al.*, 2020). Another major disadvantage of methanol is that it is produced using petroleum, whereas ethanol may be produced solely from renewable agricultural resources, implying that it can be completely independent of petroleum-based alcohol. In countries that produce ethanol, ethanol is also widely utilized. Additionally, butanol and propanol have also been employed in the production of biodiesel, this is according to the study reported by Jayaraman *et al.* (2020). In a study reported by Hanif *et al.* (2018), alkali-catalyzed is substantially faster than acid-catalyzed reaction. The most commonly utilized commercial NaOH, sodium methoxide (CH<sub>3</sub>ONa), and KOH are the most often used alkali

catalysts. Small manufacturers use KOH and NaOH flakes because they are affordable, convenient to transport, and store. The recommended catalysts for large continuous-flow production operations are solutions of  $\text{CH}_3\text{ONa}$  or  $\text{CH}_3\text{OK}$  in methanol, which are now commercially available (Singh & Tirkey, 2022). Sulphuric acid has been the most studied catalyst for acid-catalyzed systems, but other acids such as HCl,  $\text{BF}_3$ ,  $\text{H}_3\text{PO}_4$ , and organic acids have also been utilized. However, saponification reduces catalytic effectiveness, makes glycerol separation difficult, and also induces gel formation. Separating the catalyst from the reaction mixture in homogeneous catalyzed processes is difficult and costly. A substantial volume of water is utilized to separate the catalyst from the product for this purpose (Jambulingam *et al.*, 2020). Moreover, researchers have concentrated on developing novel biodiesel manufacturing technologies and optimizing procedures to conserve energy and use shorter time rather than transesterification reaction (Mathew *et al.*, 2021). As a result, new techniques including the supercritical process, ultrasound-assisted, and microwave-assisted methods have recently been employed (Cercado *et al.*, 2018).

### **2.6.1 Parameters Affecting Biodiesel Synthesis**

Transesterification can be influenced by parameters such as reaction temperature, alcohol-to-oil molar ratio, presence of water, FFA content, catalyst concentration, and reaction time.

#### **(i) Effect of alcohol to oil molar ratio**

Alcohol to oil molar ratio is critical for biodiesel yield (Moazeni *et al.*, 2019). Normally, 3 mol of alcohol is required for 1 mol of triglycerides to produce 3 mol of fatty acid ester and 1 mol of glycerol in the transesterification step. Excessive alcohol consumption accelerates the conversion of lipids to esters. So, up to a particular concentration, the production of biodiesel increases as the concentration of alcohol increases. However, increasing the alcohol level not only reduces the output of biodiesel but also raises the cost of alcohol recovery (Moazeni *et al.*, 2019).

Furthermore, the alcohol content ratio varies depending on the catalyst utilized; for example, when using an alkali catalyst, the reaction requires a 6:1 alcohol to catalyze the transesterification of oils. If the oil samples include a significant level of free fatty acid (FFA), the reaction does not respond to the alkali catalyst. In that case, an acid catalyst will be more successful at catalyzing the reaction, as it requires more alcohol than an alkali catalyst. This is owing to the acid catalyst's tolerance of the FFA and water concentration in the oil samples.



When waste cooking oil is subjected to an acid catalyst reaction, it requires a greater alcohol ratio, i.e. 15:1 as was previously reported by Cordero-Ravelo & Schallenberg-Rodriguez, (2018).

#### **(ii) Effects of reaction time**

When the reaction time is increased, fatty acid esters conversion increases. Because of the mixing and dispersion of the alcohol and oil, the reaction is gradual at first and becomes rapid later. The maximum ester conversion, however, was accomplished in 90 minutes. Increased reaction time has little effect on the yield of biodiesel or mono alkyl ester (Chang *et al.*, 2021). Furthermore, longer reaction times result in a lower-end product of biodiesel due to the reversible reaction of transesterification, which results in ester loss and soap formation (Chang *et al.*, 2021).

#### **(iii) Effects of reaction temperature**

Another key aspect influencing biodiesel output is reaction temperature. Higher reaction temperatures, for example, enhance the reaction rate and shorten the reaction time due to reduced oil viscosity. However, previous research discovered that increasing the reaction temperature over the optimal threshold value reduces biodiesel yield because it normally promotes triglyceride saponification as reported by Kumar *et al.* (2020). To prevent alcohol evaporation, the transesterification reaction temperature should typically be lower than the boiling point of alcohol. Depending on the oils or fats used, the optimal temperature might range from 50 to 60°C (Kumar & Tomar, 2019; S Kumar *et al.*, 2020).

#### **(iv) Effect of FFA and water content**

Water and FFA levels are important components in the transesterification reaction. For biodiesel generation, base-catalyzed transesterification reactions require water-free and low acid value (<1) raw materials. If the oil samples include a high FFA level (greater than 1%), the process will require more alkali catalysts to neutralize the FFA. Water has a stronger negative effect than FFAs since it can produce soap production and foaming, which can cause an increase in viscosity. Furthermore, the production of gels and foams impedes the separation of glycerol from biodiesel (Mathew *et al.*, 2021). During transesterification, FFA and water always create negative results, causing soap production and consumption of catalyst, resulting in a reduction in catalyst action and hence reducing FAME. It was suggested that a supercritical

methanol approach (623 K, 43 MPa, 4 min of treatment with methanol to oil molar ratio of 42:1) can be able to address this challenge, as compared to alkaline and acid-catalyzed methods. It should be emphasized that water has less impact in the supercritical methanol approach (Moazeni *et al.*, 2019).

#### **(v) Effect of catalyst concentration**

The concentration of catalysts also influences biodiesel production. Sodium hydroxide (NaOH) or potassium hydroxide are the most widely utilized catalysts for biodiesel generation (KOH). However, sodium methoxide is more successful since mixing sodium hydroxide with methanol produces a small amount of water, which inhibits the creation of the final product (Biodiesel) due to the hydrolysis reaction (Maheshwari *et al.*, 2022). This is one of the reasons why the catalyst is first mixed with methanol before being applied to oil or fats. Furthermore, as the concentration of catalyst in oil samples increases, it facilitates the conversion of triglycerides to biodiesel. Insufficient catalyst, on the other hand, results in partial conversion of triglycerides into FFAE. However, optimal biodiesel yield was achieved when the NaOH concentration reached 1.5 wt%, a further increase in concentration was revealed to affect end-product yield. Because extra alkali catalyst reacts with triglycerides to produce more soap, this is according to the study reported by Mathew *et al.* (2021) and Maheshwari *et al.* (2022).

### **2.7 Nanoparticle Additives**

Nanoparticles are particles with diameters ranging from 1 to 100 nm. A particle is defined in nanotechnology as a small object that behaves as a whole unit in terms of transport and properties. Particles are further classified based on their diameter. Ultrafine particles are the same as nanoparticles and range in size from 1 to 100 nm. Previous findings reported by Kunc *et al.* (2019) showed that nano-SiO<sub>2</sub> additives have small particle size, porous, and large surface area to volume ratio with many hydroxyl groups. It has unsaturated residual bonds on its surface and has high reflectivity to long-wave visible, and ultraviolet light.

Since the development of nanoscience and nanotechnology, researchers have been actively involved in the use of nano-materials (metal or metal oxide) at the nanoscale size, to generate clean energy sustainably. These days, nanomaterials are utilized for producing renewable energy that improves energy storage and is used for purifying water. Metal/metal oxide nanoparticles have currently enormous interest in the scientific community as fuel additives since the invention of nanotechnology. Several research efforts have been made to better

understand its role in improving fuel properties and ultimately, achieving the larger goal of producing environmentally clean fuel. Based on the previous study by Abdulhaleem (2019), silica nanoparticles range in size from 15 to 30  $\mu\text{m}$  with a large specific surface area. This is the size that allows them to enter the contact area as molecules, giving them some advantages over organic molecules. A promising strategy for enhancing the performance of diesel fuel is the addition of nanoparticles to improve the efficiency of the CI engine and reduce exhaust emissions.

Oi-Uchisawa *et al.* (2003) improved the platinum (Pt) catalyst for soot oxidation by using support composed of mixed oxides of  $\text{SiO}_2$ ,  $\text{Al}_2\text{O}_3$ ,  $\text{TiO}_2$ , and  $\text{ZrO}_2$  (zirconium dioxide). When loaded onto  $\text{TiO}_2$ - $\text{SiO}_2$ , the Pt catalyst exhibited significant catalytic activity. This effectiveness was further validated in a diesel engine equipped with DPF. Essentially, the combustion byproducts generated by fuel-borne  $\text{SiO}_2$  additives can serve as catalysts for soot oxidation within the DPF. A study by Ağbulut *et al.* (2020) mixed oxides of  $\text{SiO}_2$ ,  $\text{Al}_2\text{O}_3$ , and  $\text{TiO}_2$  additives with biodiesel individually and examined the impact of these additives on the combustion and efficiency of a CI engine. They found that each of these additives can enhance the CGP and the maximum HRR.

Gavhane *et al.* (2021) aimed to evaluate the performance and emissions of soybean methyl ester (SBME) under different loads and various concentrations of  $\text{SiO}_2$  nano-additives. Results showed that incorporating  $\text{SiO}_2$  nano-additives led to a 3.48–6.39% increase in BTE and a 5.81–9.88% decrease in BSFC. Additionally, CO, HC, and smoke emissions were reduced by 1.9–17.5%, 20.56–27.5%, and 10.16–23.54%, respectively, compared to SBME25 (B25) fuel blends. Adzmi *et al.* (2019) conducted a study on the impact of incorporating  $\text{SiO}_2$  nano-additives (at concentrations of 50 and 100 ppm) into a blend of palm oil methyl ester (POME) on diesel engine performance and emissions. Experiments were conducted using a single-cylinder diesel engine under various operating loads and a constant engine speed. Their findings showed that the addition of  $\text{SiO}_2$  nano-additives led to a 43% increase in BP, a 25% decrease in CO, and 4.48% reduction in  $\text{NO}_x$  emissions across various load conditions and levels of silica nano-additives.

The research by Özgür *et al.* (2015) investigated the impact of adding  $\text{SiO}_2$  nano-additives (25 and 50 ppm) to rapeseed methyl ester on diesel engine performance and emissions. The results showed a maximum increase in BP of 4.2–4.8% and brake torque of 3.6–4.3% for the 25 and 50 ppm blends, respectively. There was a 10.4% reduction in CO emissions with the 25 ppm

SiO<sub>2</sub> nano-additives blend, and the maximum reductions in NO<sub>x</sub> emissions were 7.2% and 9.4% for the 25 and 50 ppm nanoparticle blends, respectively. Overall, the study suggests that the effects on performance and emissions vary depending on multiple factors and are not definitively conclusive. Ghafoori *et al.* (2015) reported on metal nanoparticle combustion in a diesel engine and discovered that nano-sized metallic powders have a large specific surface area, which leads to increased fuel activity. Adding nano additives to hydrocarbon and biofuels reduces kinematic viscosity, increases calorific value, enhances oxidation stability, and raises the flash point. Consequently, this process improves ID and minimizes soot emissions.

According to Karthickeyan (2019), on examining the engine operational characteristics of diesel blended with canola oil methyl ester with 50 and 100 ppm concentrations of zinc oxide (ZnO), operating at 1500 rpm under full load. The physical and chemical characteristics showed a slight improvement when compared to neat biodiesel. These included an increase in the calorific value (from 38 455 to 42 931 kJ/kg at 100 ppm ZnO nanoparticle), cetane index (from 6.28 to 56), kinematic viscosity (from 5.5 to 3.8 mm<sup>2</sup>/s at 50 ppm) and flash point (from 49.5 to 51°C at 50 and 100 ppm) respectively. Another study conducted an experimental study on the physicochemical properties and performance of biodiesel after the addition of cerium oxide (CeO) nanoparticles. The results observed that the flash point and the viscosity of the biodiesel increased with the addition of the CeO nanoparticles. The emission of the UHC and NO<sub>x</sub> were reduced with the presence of additives (Sajith *et al.*, 2010).

Hoseini *et al.* (2020) reported the effects of graphene oxide (GO) nano-particles on the performance and emissions of a diesel engine fueled with *Oenothera lamarckiana* biodiesel. The investigated biodiesel was used in the blend of B20. The GO nano-particles with concentrations of 30, 60, and 90 ppm were considered for each fuel blend at 2100 rpm and loads of 0, 25, 50, 75, and 100%. Results showed EGT significantly increased and reductions in CO (~5-22%) and THC (~17-26%) were observed. However, GO nano-particles were purchased from the Iranian Research Institute of Petroleum Industry (RIPI) which were also made from inorganic compounds (Hoseini *et al.*, 2020). Therefore, this study used SiO<sub>2</sub> extracted from RH which is agricultural waste and is readily available (September *et al.*, 2023).

In another research, Sivasaravanan *et al.* (2019) evaluated the impact of nanoparticles derived from RH in a single-cylinder diesel engine fueled with Neem-based biodiesel blends and baseline diesel. When 1000 ppm RH nanoparticles were blended with B0, B10, and B20, BTE increased by 1.7, 6.6, and 8.3%, respectively, while BSFC decreased by 4, 6.9, and 6.1%,

respectively, compared to their respective baseline fuels. The B0, B10, and B20 additive by RH nanoparticles reduced CO emissions by up to 7.1, 10.3, and 10%, respectively. The amount of HC released was reduced by 6.5, 11.3, and 11.2%. However, NO<sub>x</sub> emissions rose by 4.7% for diesel vehicles, while B10 and B20 vehicles were reduced by 2 and 11.9%, respectively. However, in their study, they did not investigate how RH nanoparticles doped into Neem-based biodiesel blends influenced engine combustion characteristics.

On the contrary, the utilization of these additives is restricted due to their economic viability, fuel blending ratio, and toxicity, which are influenced by the rapid evaporation and extended ID of biodiesel. However, using RH as a nanoparticle additive may result in sedimentation on the cylinder wall and piston ring, reduce the lubricity of the fuel mixture, increase engine wear and corrosion, and can also damage the exhaust valve guides and engine bearings. This is due to the lower surface area-to-volume ratio and the presence of impurities in RH (Ashraful *et al.*, 2014). Thus why, the current study focuses on using pure RH silica, which has a large surface area-to-volume ratio due to a lower pore radius.

Most of the recent nanoparticle additions, however, are made from a non-renewable source which is not commercially feasible nor environmentally friendly. The synthetic technique for making new metal oxide is the Sol-Gel process. This process includes drying, polymerization, condensation, and hydrolysis. The primary drawbacks of this approach are its time-consuming, contamination of hazardous materials (toxic heavy metals), and challenging phase separation (Kapile *et al.*, 2022). Among the recent additives used in diesel and biodiesel fuels, nanoparticles have emerged as a novel and promising additive that results in the reduction of exhaust emissions, improves oxidation stability, and enhances engine performance. Many researchers have focused their attention on fuel modification methods by using nano-additives to achieve improved performance and emission characteristics (Lv *et al.*, 2022).

### **2.7.1 Physicochemical Properties of Nano-Silica Additives**

#### **(i) Nanoparticle textual profile**

Using a fully automated analyzer, BET analysis provides precise specific surface area evaluation of materials by nitrogen multilayer adsorption measured as a function of relative pressure. The technique includes external area and pore area evaluations to determine the total specific surface area in m<sup>2</sup>/g, which is useful in studying the effects of surface porosity and particle size in a variety of applications. Using adsorption and desorption techniques, BJH

analysis can also be used to determine pore area and specific pore volume. This technique characterizes the pore size distribution independent of the sample's external area due to particle size. The BET theory was an extension of the Langmuir theory, developed by Irving Langmuir. According to the Langmuir theory, the gas pressure of a medium above a solid surface at a constant temperature is related to the monolayer adsorption of gas molecules, also known as adsorbates, onto a solid surface.

The following assumptions form the foundation of the Langmuir theory:

- (i) The same adsorption energy applies to all surface sites for the adsorbate, typically argon, krypton, or nitrogen gas. The region on the sample where one molecule can adsorb is known as the surface site.
- (ii) Adsorption of the solvent at one location happens separately from adsorption at nearby locations.
- (iii) Adsorbate activity is inversely proportional to concentration.
- (iv) Adsorbates form a monolayer.
- (v) Each active site can be occupied only by one particle.

The Langmuir theory has a few flaws that the BET theory addresses. With three additional assumptions, the BET theory extends the Langmuir theory to multilayer adsorption (Swenson & Stadie, 2019):

- (i) Gas molecules will physically adsorb on a solid in layers infinitely
- (ii) The different adsorption layers do not interact
- (iii) Theory can be applied to each layer

The following is the mechanism of the BET theory.

Adsorption is the adhesion of gas atoms or molecules to a surface. Adsorption should not be confused with absorption, which occurs when a fluid permeates a liquid or solid. The amount of gas adsorbed is determined not only by the exposed surface, but also by temperature, gas pressure, and the strength of the interaction between the gas and solid. Nitrogen is commonly used in BET surface area analysis due to its high purity and strong interaction with most solids.

Because the interaction between gaseous and solid phases is typically weak, the surface is cooled with liquid N<sub>2</sub> to achieve detectable levels of adsorption. The sample cell is then gradually filled with known amounts of nitrogen gas. To create partial vacuum conditions results in relative pressures lower than atmospheric pressure. No further adsorption occurs after the saturation pressure, regardless of the pressure increase.

Pressure transducers with high precision and accuracy monitor pressure changes caused by the adsorption process. Following the formation of the adsorption layers, the sample is removed from the nitrogen atmosphere and heated, causing the adsorbed nitrogen to be released from the material and quantified. The collected data is displayed as a BET isotherm, which plots the amount of gas adsorbed as a function of relative pressure (Wang *et al.*, 2015).

## **(ii) Thermal gravimetric analysis of nanoparticle**

Thermal gravimetry is a branch of thermal analysis that studies the weight change of a substance as a function of time or temperature. When the sample is subjected to a controlled heating or cooling environment, the weight change profile is recorded. The term "isothermal mode" refers to when the weight change is recorded as a function of time. The weight change as a function of temperature is recorded in scanning mode (Loganathan *et al.*, 2017). The main idea behind thermogravimetric analysis (TGA) is that the mass change of a sample can be studied under controlled conditions. As a result, TGA is primarily used to comprehend thermal events such as absorption, adsorption, desorption, vaporization, sublimation, decomposition, oxidation, and reduction. TGA can also be used to evaluate volatile or gaseous products lost during chemical reactions for samples such as nano-materials, polymers, polymer nano-composites, fibers, paints, coatings, and films. TGA can be used to study the kinetics of chemical reactions under various conditions in addition to predicting thermal stability for samples. To investigate the kinetics, it is necessary to optimize the factors or conditions that influence the mass change of samples throughout the experiment. The following factors have been discovered to influence mass change: (a) the weight and volume of the sample taken for analysis, (b) the physical form of the sample, (c) the shape and nature of the sample holder, (d) the nature of the atmosphere under which the analysis is performed, (e) the pressure of the atmosphere maintained in the sample chamber during the analysis, and (f) the rate of heating or cooling. Temperature conditions are well known to cause changes in sample mass. However, it is critical to recognize that not all types of thermal changes can influence weight change. Sample melting and crystallization behavior, for example, cannot be predicted by TGA.

Thermo-balance is the TGA unit's brain consisting of several smaller components, including an electronic microbalance, a sample holder, a furnace, a temperature programmer, and a recorder. The arm of a microbalance is held in place by a clamp that is part of the thermo-balance. It is important to note whether the balance returns to the zero position after the clamp is released (Loganathan *et al.*, 2017). Transporting the thermo-balance while clamps are holding the microbalance's arm is not advised. If such transportation is attempted, the zero point will be impacted. After the sample has been properly placed, it is generally preferred to wait for the microbalance to stabilize for 15–20 min.

### (iii) **Fourier transformation infrared spectroscopy (FT-IR)**

One contemporary analytical method for determining the nanoparticle's conversion is FT-IR. Rice husks are relatively effective absorbers in the infrared range ( $1750\text{--}1760\text{ cm}^{-1}$ ). It's a quick and easy way to detect functional groups. This method uses a scanning probe to combine FT-IR with s-SNOM, or scattering-type scanning near-field optical microscopy. Similar to s-SNOM, nano FT-IR is based on atomic force microscopy (AFM), which involves shining an external light source on a sharp tip and measuring the back-scattered light as a function of tip location.

A typical nano FT-IR setup consists of an AFM, a broadband infrared light source for tip illumination, and a Michelson interferometer that doubles as a Fourier transform spectrometer. In nano-FT-IR, the sample stage was positioned in one of the interferometer arms, enabling the recording of the detected light's phase and amplitude (unlike conventional FT-IR, which typically does not produce phase information). Simple chemical identification and characterization are made possible by the direct comparison of nano-FT-IR spectra with standard FT-IR databases for organic chemicals, polymers, biological materials, and other soft matter (Jung *et al.*, 2018). Nano-FT-IR is usually performed under ambient conditions and doesn't require any specific sample preparation. It uses an AFM in noncontact mode, which is sufficient for soft-matter and biological sample studies and is inherently non-destructive. Not limited to infrared, nano-FT-IR can be used from THz to visible spectral ranges, depending on application needs and broadband source availability. AFM-IR, SNOM, TIP-enhanced Raman spectroscopy (TERS), and other scanning probe techniques can be used in conjunction with nano-FT-IR for vibrational research. The wavelength of the carbonyl peak ( $1744\text{ cm}^{-1}$ ) is used as a signal to monitor the progress of the reaction. However, prior research has demonstrated the effectiveness of this technique in a well-established system, it also highlights some of its



drawbacks such as; that it is not product-specific and may be susceptible to a range of interferences. The ester carbonyl group stretching vibration at  $1740\text{ cm}^{-1}$  exhibits strong bands, the -COC vibration at  $1171$  and  $1207\text{ cm}^{-1}$  has medium intensity bands, and the  $(\text{CH}_2)$  group vibration band is present at  $724\text{ cm}^{-1}$ . They confirmed the sample's low moisture content by observing the absence of a wide band in the  $2500\text{--}3300\text{ cm}^{-1}$  region (Rosi *et al.*, 2019).

#### **(iv) Gas chromatography-mass spectrometry (GC-MS)**

In analytical chemistry, gas chromatography (GC) is a frequently employed chromatography technique for the separation and examination of substances that are vaporized without undergoing degradation. GC is widely used to assess the purity and evaluate the relative amount of a given material or separate its constituent parts from one another. Sometimes GC might help identify a molecule as well as in isolating pure compounds in preparative chromatography (Long *et al.*, 2018).

#### **(v) X-ray diffraction (XRD) spectral analysis**

X-ray diffraction (XRD) is a versatile technique used in nanotechnology to characterize and obtain accurate information about the composition, crystal structure, and crystalline grain size of nanoparticles. The XRD method works best with powdered samples that have been freshly prepared by drying the samples' respective colloidal solutions. The position and intensity of a sample's peaks are compared using XRD equipment to patterns from various diffraction database references, which aids in quantifying the composition of nanoparticles (Poulose *et al.*, 2023).

The scattering of X-rays caused by the revolution of electrons in the nucleus of the atom when the rays strike the nanoparticles is the working principle of the XRD method. The scattered X-rays are reflected in different directions, resulting in interference patterns. These patterns can be destructive or constructive, but only the scattered X-rays that interact constructively cause diffraction. When two waves move in phase with one another, constructive interference occurs in a nanoparticle; when they move out of phase, destructive interference occurs. Atoms with shorter periodic arrangements exhibit greater diffraction angles and vice versa. The atomic-scale arrangement and the diffraction are strongly and inversely correlated (Peppenene, 2018; Vahidi *et al.*, 2021).

#### **(vi) Scanning electron microscope (SEM)**

Another method for determining particle size, shape, and texture that only allows milligram quantities of material to be used is scanning electron microscopy (SEM). In a SEM, a small electron beam moves in parallel tracks across the prepared sample. A cathode-ray tube's screen can be used to detect and display the various signals that are produced as a result of the electrons' interactions with the sample. Because the depth of focus is so much greater than that of the light microscope, it is possible to see particles smaller than 1 nm and to gather data on surface texture. In contrast to optical microscopy, SEM requires more time-consuming sample preparation and cannot differentiate between crystalline and non-crystalline materials. Additionally, it is more challenging to produce a particle size distribution using SEM because, despite being visual and descriptive, the information is typically not quantitative. After all, only a small number of particles are visible in the viewing field at any given time. The SEM, however, can offer useful additional information on particle texture when combined with other techniques like laser diffraction, which may help to explain agglomeration or flow issues.

### **2.8 Operation of Compression Ignition (CI) Engine**

Compression ignition is the basis for diesel engine operation. In a CI engine, combustion is an irregular process that occurs simultaneously at various locations in a nonhomogeneous mixture at a rate regulated by fuel injection. The fundamental difference between CI engine combustion and spark injection (SI) engine combustion is that CI engine combustion is unassisted and occurs on its own. In a CI engine, the combustion space is filled with fuel after the air has been compressed. The extreme temperature and pressure of air cause fuel that is injected in atomized form to burn on it, this burning process lasts as long as fuel is injected. In theory, the fuel injection and burning process should occur concurrently until the cut-off point; however, this is not the case in real-world CI engines (Choudhary *et al.*, 2018). Generally, in SI engines, fuel is typically injected into the intake manifold or directly into the combustion chamber, mixed with air, and then ignited by the spark plug but in CI engines, fuel is injected directly into the combustion chamber under high-pressure, usually using a fuel injector (Choudhary *et al.*, 2018). According to the Fig. 5, the various important combustion phases are described as follows:

#### **(i) Ignition delay (ID) period**

During this stage, compressed air is fed into the combustion area along with fuel in an atomized form. Nevertheless, preparation time is needed before the start of combustion (SoC) and the

fuel does not burn instantly. A fuel droplet initially transforms into vapor (a gaseous state) when it is injected into heated air. The ignition is set if the internal temperature is higher than the temperature required for self-ignition at the appropriate pressure. Consequently, "physical delay," or the time required to change a liquid droplet into a gas, and "chemical delay," or the time required to get ready for a chemical reaction to begin, can be attributed to the delay in initiating the ignition. The duration of the ID is determined by the fuel characteristics, compression ratio (i.e. pressure and temperature after compression), fuel injection, ambient air temperature, engine speed, and combustion chamber geometry, among other factors. The ID is inevitable at this stage, so fuel injection is advanced by about 20° before Total Dead Center (bTDC) to compensate. In Fig. 5, the A-B path represents ID, showing pressure rise during combustion. Fuel injection starts at 'A', and ignition starts at 'B'. In theory, this ID should be as short as possible (Mustayen *et al.*, 2022).

## **(ii) Uncontrolled or premixed combustion**

During the ID period, the injection of fuel continues as it did at point A' and will continue until the cut-off point. During the preparation for ignition, continuous fuel injection results in the accumulation of fuel in the combustion chamber. When ignition begins, the sustainable flame front is established, and this accumulated fuel is rapidly burned. This uncontrolled burning of accumulated fuel occurs in such a way that the combustion process becomes uncontrolled, resulting in a steep pressure rise as shown from 'B' to 'C'. The uncontrolled burning continues until all of the collected fuel is burned. If the pressure rises during this phase, it becomes very abrupt and the combustion is referred to as abnormal combustion, which can cause engine parts to be damaged in extreme conditions. Therefore, it is clear that "uncontrolled combustion" depends on the ID period because, during the ignition delay itself, fuel accumulates and burns, causing a steep pressure rise. Therefore, the ignition delay should be as short as possible to ensure the least amount of uncontrolled combustion, which releases about one-third of the total fuel heat (Kumar *et al.*, 2020).

## **(iii) Controlled combustion**

Once the uncontrolled combustion is complete, the rate of burning matches the rate of fuel injected, and the combustion is referred to as controlled combustion. Controlled combustion is shown between 'C' and 'D' and maximum heat is evolved in a controlled manner during this phase. During the controlled combustion phase, the rate of combustion can be directly regulated

by the rate of fuel injection, via the fuel injector. During this phase, pressure varies smoothly and the maximum temperature is reached. It is observed that approximately two-thirds of total fuel heat is released during this phase.

**(iv) After-burning**

Any residual that remains after controlled combustion is burned and this phase is then referred to as after burning. This after-burning may exist because of fuel particles that are located far from the flame front in the combustion space. "After-burning" spans  $60^\circ$  to  $70^\circ$  of the crank angle's rotation and happens even during the expansion stroke.

### **2.8.1 Factors Affecting ID Period in CI Engines**

**(i) Compression ratio (CR)**

An increase in CR increases the temperature of the air. Auto-ignition temperature decreases with increased density. Both these reduce the delay period (DP).

**(ii) Engine power output**

With an increase in engine power, the operating temperature increases. The A/F ratio decreases and the delay period decreases.

**(iii) Engine speed**

The delay period decreases with increasing engine speed, as the temperature and pressure of compressed air rise at high engine speeds.

**(iv) Injection timing**

The temperature and pressure of air at the beginning of injection are lower for higher injection advance. The DP increases with an increase in injection advance or longer injection timing. The optimum angle of injection is  $20^\circ$  bTDC.

**(v) Atomization of fuel**

Higher fuel injection pressures increase the degree of atomization. The fineness of atomization reduces the DP due to the higher A/V ratio of the spray droplet.

**(vi) Injection pressure**

Increased injection pressure increases fuel temperature and also reduces droplet size, therefore reducing DP due to the higher A/V ratio of spray droplets.

**(vii) Intake temperature**

High intake temperature increases the air temperature after compression, which reduces DP.

**(viii) Engine size**

Large engines operate at lower speeds, thus increasing the DP in terms of crank angle.

**(ix) Cetane number**

Fuels with high CN have lower DP.

**(x) Fuel/air ratio (F/A)**

With an increasing F/A ratio, operating temperature increases, and thus DP decreases.

**(xi) Injection duration**

An increase in injection duration, results in a higher quantity of fuel injected which leads to an increased operating temperature and reduces DP.

## **2.8.2 Classification of Combustion Chambers of CI Engine**

- (i) Direct-injection (DI) engines, which have a single open combustion chamber and direct fuel injection;
- (ii) Indirect-injection engines in which fuel is injected into the pre-chamber, which is located above the piston crown and connected to the main chamber by a nozzle or one or more orifices, in, which the chamber is divided into two regions.

Generally, for a DI engine; An open chamber is a chamber formed between the piston and the cylinder head that contains the entire compression volume in which the combustion occurs. To help fuel and air, the combustion chamber's shape may produce swirl or turbulence. Swirl and turbulence both refer to the motion of the gases in the chamber, which rotates roughly around the chamber axis. The mixing of fuel and air in this combustion chamber is entirely dependent

on the spray characteristics and air motion, and it is not significantly impacted by the combustion process. To achieve rapid mixing in this type of engine, the spray characteristics must be carefully arranged. High injection pressure is used to inject the fuel and swirling or squishing of the air caused by a small clearance space over a portion of the piston is typically used to assist in mixing.

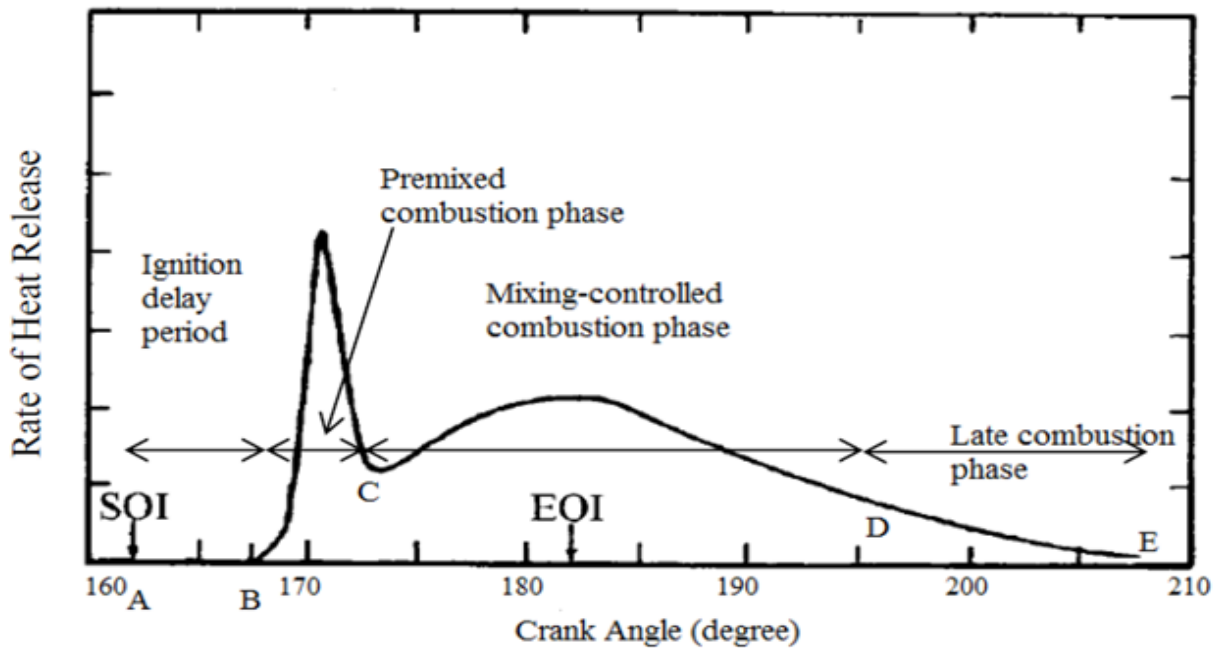


**Figure 4: Diesel combustion stages (Choudhary *et al.*, 2018)**

### 2.8.3 Engine Performance, Emission, and Combustion Characteristics

The combustion of a diesel engine is a significant but complex phenomenon. The combustion efficiency of a diesel engine determines its performance and emissions. Many researchers have investigated the engine performance, emissions, and combustion of biodiesel-fueled diesel engines. The majority of them stated that the major combustion factors influencing performance, combustion, and emissions are heat release rate (HRR), ID, combustion phases, maximum heat release rate ( $HRR_{max}$ ) in premixed phase, and combustion duration. More specifically, combustion affects emissions such as  $NO_x$ , PM, THC,  $CO_2$ , and CO formation, as well as performance such as brake specific fuel consumption (BSFC), brake specific energy consumption (BSEC), exhaust gas temperature (EGT), and brake thermal efficiency (BTE). The effects of combustion on performance and emissions varied depending on parameters such as biodiesel feedstock (sources), biodiesel content, cetane number, advance injection timing

and combustion, oxygen content, engine load, engine speed, density, and viscosity (Sathish & Singaravelu, 2020).

#### **2.8.4 Health And Environmental Risks of Diesel Engine Exhaust Emissions**

According to air quality data (based on 2014 – 2016), it is estimated that about 70% of total known cancer risks related to air toxics in California, were attributed to PM. Short-term exposure to diesel exhaust can lead to serious human health negative effects such as acute irritation (eye, throat, bronchial), neurophysiological symptoms (lightheadedness, nausea), and respiratory symptoms (cough, phlegm). Long-term exposure led to an immunologic effect to worsen existing heart and lung disease. Premature deaths especially in children and elders, allergenic responses, and asthma-like symptoms (Verma *et al.*, 2019). Environmentally, emissions from diesel engines contribute to the production of ground-level ozone which damages crops, trees, and other vegetation. Also, the formation of acid rain affects soil, lakes, and streams and enters the human food chain via water, meat, and fish. These emissions also contribute to property damage and reduced visibility. Global climate change affects air and water quality, fluctuation of weather patterns, rising sea levels, melting of snow, and floods, also affect ecosystems and agriculture. Reducing GHG emissions from diesel engines through improved fuel economy or idle reduction strategies can help address climate change, improve our nation's energy security, and strengthen our economy (Hussain *et al.*, 2020).

#### **2.8.5 Global Policy Overview**

Based on The Environmental Protection Agent (EPA) aims to maintain a safe environment for people to live, learn, and work in by giving everyone an equal level of protection from environmental and health risks and access to decision-making. Diesel Emissions Reduction Act (DERA) program initiatives support EPA's commitment to lessen the harm that diesel emissions cause to people's health and the environment in every community across the nation. As stipulated in the Energy Policy Act: of 2005 (Kaufman *et al.*, 2020).

Under the EPA Act 2005, the EPA was to prioritize projects that maximize public health benefits, enhance cost-effectiveness, and serve areas with the highest population density and the poorest air quality. To include a certified and verified engine configuration and technology. Also to maximize the engine's expected useful life as well as to use diesel fuel with a sulphur content of 15 ppm or less. EPA's National Clean Diesel Campaign for Transportation and Air Quality administers the DERA program. In its DERA Fifth Report to Congress (August 2022),

the EPA reports that it awarded more than USD 801.0 million between 2008 and 2018 to retrofit or replace 73 700 engines in vehicles, vessels, locomotives, and other equipment. EPA estimates that the program has resulted in the reduction of emissions of NO<sub>x</sub> by 491,000 tons, PM by 16 800 tons, and carbon dioxide by 5.3 million tons over the lifetime of the affected engines. Further, the EPA estimates that DERA funding requests have exceeded availability by as much as 35:1 for the rebate program and 7:1 for the national grant competition (Alvarez *et al.*, 2024).

## **2.9 Summary**

- (i) The biodiesel derived from edible food-grade components may contribute to rising food inflation and insecurity (Kaimal *et al.*, 2022). This study focused on using non-edible feedstock.
- (ii) Biodiesel is very prone to auto-oxidative breakdown, which has an impact on storability and engine performance (Mahmud *et al.*, 2022). This study employed nano-silica additives to improve important fuel properties of biodiesel and its blends.
- (iii) The synthetic technique for making new metal oxide is the Sol-Gel process. This process includes drying, polymerization, condensation, and hydrolysis. This process involves time-consuming, contamination of hazardous materials (toxic heavy metals), and challenging phase separation. This study used a calcination process that is simple, cheap, and affordable.
- (iv) The most used commercial nanoparticles are very expensive and not environmentally friendly. Therefore, this study used nano-silica additives extracted from RH as agricultural waste, this helps to increase its value instead of burning them to enhance pollution.



## 2.10 Conceptual Framework

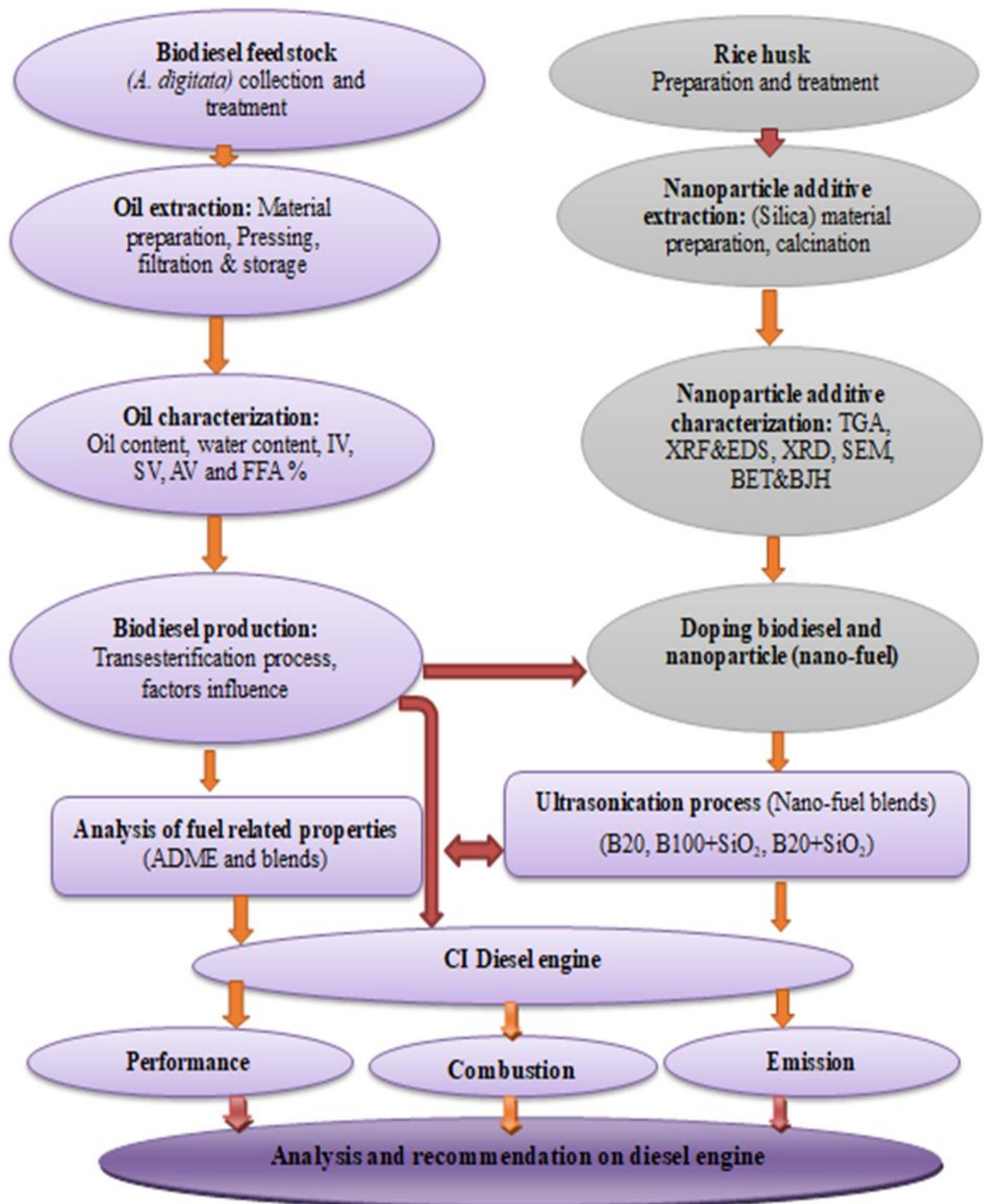


Figure 5: Conceptual framework of the utilization of nano-silica additives on fuel blends in CI engine

## CHAPTER THREE

### MATERIALS AND METHODS

#### 3.1 Materials

Ripe *Adansonia digitata* (baobab fruits) were collected from Dodoma and Singida in Tanzania, peeled to obtain the seed part, and the broiler of the seed was dried to remove moisture in preparation for the oil pressing machine. Rice husk (*Oryza sativa*) waste was bought from a local processing rice mill in Arusha municipality, washed, and dried for nanoparticle calcination. The chemical reagents such as ethanol (99.5%), Potassium hydroxide (85%), Sodium thiosulphate, Sulphuric acid ( $\text{H}_2\text{SO}_4$ , 98%), hydrochloric acid (HCl, 95%), and sodium hydroxide (NaOH, 99%) anhydrous pellets (97%), methanol ( $\text{CH}_3\text{OH}$ , 99.5%), and sodium dodecyl sulphate (SDS), were purchased from the Diligent Chemicals Storage Company (Dar es Salaam, Tanzania) and others from Dar es Salaam University College of Education (Dar es Salaam, Tanzania). The samples including pure ADME (B100), bending of 20% of biodiesel and 80% of diesel (B20), nano-fuel blend of B20 and nano-silica ( $\text{B20}+\text{SiO}_2$ ), and blend of biodiesel and nano-silica ( $\text{B100}+\text{SiO}_2$ ) and conventional diesel (B0), which was used as a base fuel were tested on the CI diesel engine installed at Budapest University of Technology and Economics at Budapest, Hungary.

#### 3.2 Preparation and Characterization of ADSO

##### 3.2.1 Preparation of ADSO

The ADSO was extracted from dried seeds using a double screw press machine. An expeller press is a screw-type machine that presses oil seeds through a caged barrel-like cavity. Raw materials enter one side of the press and waste products exit the other side. The machine uses friction and continuous pressure from the screw drives to move and compress the seed material. The oil seeps through small openings that do not allow seed fiber solids to pass through. Afterward, the pressed seeds are formed into a hardened cake, which is removed from the machine. The pressure involved in expeller pressing creates heat in the range of 60 – 99°C. Figure 6 displays the photographs of baobab fruit, pulp, seeds, and seed oil.

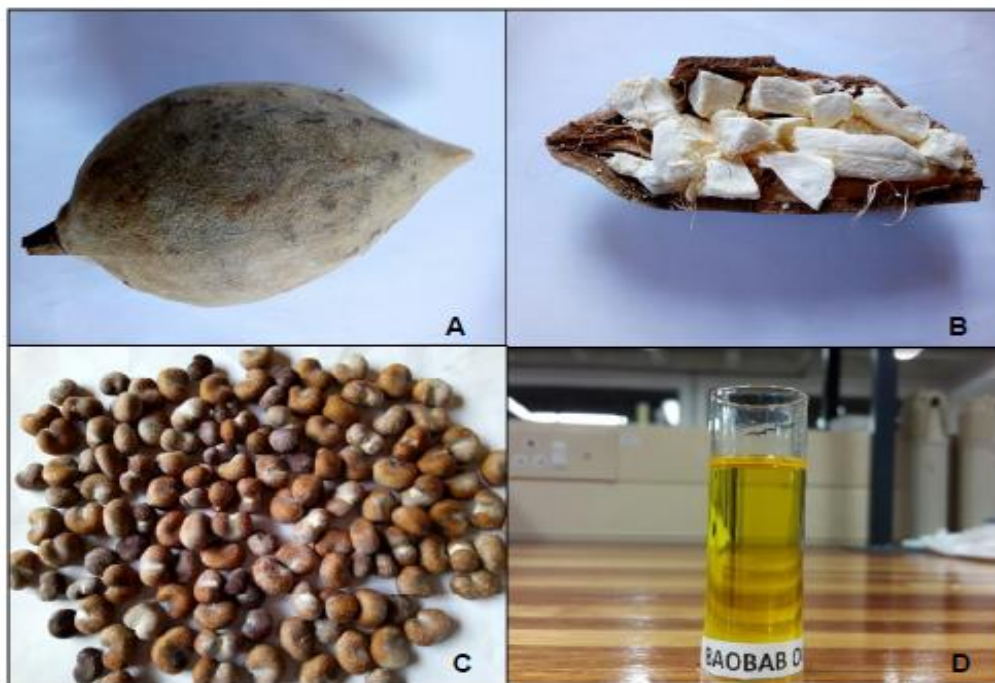


**Figure 6:** Photograph of baobab (A) fruit (B) fruit pulp (C) seeds (D) seed oil (Chilabade, 2018)

### 3.2.2 Physicochemical Characterization of ADSO and Its Derivatives

The physicochemical properties of ADSO were investigated, such as density was determined as stipulated in EN 12185, water content (ASTM D6304), oil content (EN 4264), CN (ASTM D6890), IV (EN 3961), percentage of FFA (EN 4264), and AV (ASTM D664). The properties of oil and its derivatives were determined according to the AOAC and ASTM D6751 (Folayan *et al.*, 2019). Table 3 shows instruments used with technical methods applied in the experiment.

#### (i) Determination of oil content

The oil was mechanically removed from the confined seed by exerting enough power on it. In these circumstances, the pressure is great enough to rupture the seed and release the oil 4 g of samples extracted by pressing for 2 h were used to calculate the oil content. After the solvent was evaporated, the weight of dried oil seeds was measured using digital balance, and the weight of the residual was also measured, then Equation 2 was used to determine the percentage of crude oil that was left (Sangkharak *et al.*, 2020).

$$\% \text{ of oil content} = \frac{\text{weight of dried seeds} - \text{weight of residual}}{\text{weight of dried seeds}} \times 100 \quad (2)$$

**Table 3: Test methods and instruments used in the measurement of ADSO and ADME**

Test	Units	Method	Instrument
Oil content	%	Calculation	Calculation
Acidic value	mgKOH/g	ASTM D664	Si analytic
Moisture content	ppm	ASTM D6304	Moisture meter
Density @15°C	kg/m <sup>3</sup>	EN ISO12185	Densitometer
Iodine value	gI <sub>2</sub> /100g	EN ISO3961	Titration
Cetane number (min.)	-	ASTM D6890	
Saponification value	MgKOH/g	ASTM D 664	
Pour point	°C	ASTM D97	Pour test cabinet
Kinematic viscosity at 40°C	mm <sup>2</sup> /s	ASTM D7042	Viscometer
Cloud point	°C	ASTM D2500	Cloud test cabinet
Calorific value	MJ/kg		Bomb calorimeter
Flash point	°C	ASTM D6450	Pensky-Martin open cup tester

### (ii) Determination of moisture content

The moisture content of 6 g of oil was assessed by heating it in a pre-dried aluminum dish at 105°C for approximately 8 hours in a temperature-controlled oven. The weight of seeds before dried and that of dried seeds was recorded by digital balance. The percentage of moisture content was calculated relative to the initial weight of the sample (% dry weight), as described in Equation 3 (Mauer & Bradley, 2017; Nielsen & Nielsen, 2017).

$$\% \text{ of moisture content} = \frac{\text{weight of seed before dried} - \text{weight of dried seeds}}{\text{weight of seeds before dried}} \times 100 \quad (3)$$

### (iii) Determination of acidic value (AV)

Acidic value (AV) is defined as the measurement of the FFA content of the oil. The glass indicating and reference electrode were used to dissolve the sample in a toluene and propane-2-ol mixture that contained a small amount of water. It was then stoichiometrically titrated with alcoholic KOH. The endpoint was only taken at distinct inflections in the resulting curve, which

was produced by manually or mechanically plotting the meter readings against the relevant quantities of titrating solution. When no discernible inflections were found, endpoints were selected at meter readings that matched those observed for used oils and aqueous basic and acidic buffer solutions (ASTM- D 664). It is expressed as the amount of KOH (in mg) to neutralize 1 g of oil and then calculated by Equation 4.

$$AV = \frac{\text{titre volume} \times \text{grams of NaOH in 0.1 M of KOH solution}}{\text{sample weight in grams}} \quad (4)$$

#### (iv) Determination of free fatty acids (FFA) composition

The GC-MS at the UDSM, Tanzania, was used to analyze the samples as depicted in Fig. 7. It was recorded in a GC-MS-QP 2010 Ultra Shimadzu instrument operating in Electron Ionization (EI) mode (MS) at 70 eV, and Flame Ionization Detector (FID) for GC. A Restek-5MS capillary column (30 m x 0.25 mm x 0.25 mm) was used. The oven temperature program was 60°C to 260°C and held at 60°C for 4 min. The temperature was increased to 260°C for 12 min (hold time) at the rate of 7°C/min. The injection mode was split and the temperature was 250°C. Helium carrier gas flowed at a rate of 11.21 mL/min. In MS, there was an ion source temperature of 230°C and an interface temperature of 300°C. With the use of Mass Spectral Library and Search Software (NIST), the scan method was able to identify the compounds in the samples. With a 20% ion allowance, the target ion, and five additional reference ions utilized in the quantitative analysis, the compounds present in the samples were quantified using the peak height integration method. All scanned compounds in the samples had peak heights, which were used to calculate the percentage compositions of the results.



**Figure 7:** The GC-MS instrument used for fatty acid composition analysis

**(v) Saponification value (SV)**

According to Seshamamba *et al.* (2018) procedures, SV can be calculated for which in 15 mL of ethanoic KOH, 0.5 g of oil was dissolved, which was synthesized by 0.5 M in 95% ethanol 018. An hour was spent heating the solution and slowly stirring it with a magnetic stirrer. While the solution was still hot, two drops of phenolphthalein indicator were added, and 1 M HCl was added to titrate it. Equation 5 was used to determine the saponification value.

$$SV = \frac{(b-a) \times \text{grams KOH in 0.5 MKOH solution}}{\text{sample weight in grams}} \quad (5)$$

where  $a$  and  $b$  are the volumes of oil and titre blank solution respectively.

**(vi) Iodine value (IV)**

By utilizing chemicals such as carbon tetrachloride ( $\text{CCl}_4$ ), 0.1 N  $\text{Na}_2\text{S}_2\text{O}_3$  solutions, Wijs reagent, 10% potassium iodide (KI), and starch indicator, by titration process, the IV of the oil sample was determined. 5 mL of  $\text{CCl}_4$  was added to each flask. The oil sample of about 10 g was placed into one flask, leaving the other empty. Each flask was titrated with 0.1 N  $\text{Na}_2\text{S}_2\text{O}_3$  solutions for 20 min and then 60 mL of distilled water and 8 mL of KI solution were added. The IV was calculated using Equation 6.

$$IV = \frac{(b-a) \times N(\text{Na}_2\text{SO}_4) \times \text{mass of iodine in 0.1 MICI}}{\text{sample weight (g)}} \quad (6)$$

where  $a$  is titration volumes of blank,  $b$  is titration volumes of oil, and  $N$  is the Normality of  $\text{Na}_2\text{S}_2\text{O}_3$ .

**(vii) Density at 15°C**

An oscillating sample tube was filled with a small volume of liquid sample (about 0.7 mL) and sample density was determined using calibration data and the change in tube mass was brought by oscillating frequency (Sarkar *et al.*, 2020).

**(viii) Kinematic viscosity at 40°C**

A calibrated viscometer shown in Fig. 8 with a reproducible driving head was used to measure the amount of time needed for a fixed volume of liquid to flow through its capillary at a known

and tightly controlled temperature. Kinematic viscosity was calculated by multiplying the measured flow time by the viscometer's calibration constant (Folayan *et al.*, 2019).



**Figure 8: Viscometer**

#### **(ix) Calorific value**

An adiabatic bomb calorimeter was used as shown in Fig. 9. Under standard conditions, the calorimeter's effective heat capacity was determined using benzoic acid, which has a certified calorific value of 26.47 MJ/kg. An amount of 1 mL of pure water was used to pipette the explosive. After being precisely weighed 0.5 g, the oil cup was filled with the sample and dropped into the bomb. An ignition source was suspended within the sample from a nickel-chromium wire. During assembling, the bomb was charged with oxygen at 35 atm. The calorimeter was originally set at a temperature of about 275 K below ambient to minimize heat losses. The firing circuit was closed and the jacket's temperature was watched until it dropped for an additional 5 min after the water jacket's natural heat transmission took about another 5 min. Equation 7 was used to get the net calorific value. Three repetitions of the experiment results were allowed for a variation of roughly 0.28 MJ/kg.

$$\text{Calorific value (cal/g)} = \text{“(water equivalent (g) + water quantity of inner cylinder)”} \times \text{change in temperature} - \text{“calory correction /quantity of sample (g)”} \quad (7)$$



**(x) Cloud point**

Apparatus used in cloud point determination were a test jar, cork-carrying thermometer, water bath with heater, cloud point chamber, and crushed ice. The test jar was filled to the level mark, closed tightly by the cork carrying the thermometer, and placed into a bath of crushed ice. The test jar was removed from the jacket quickly without disturbing the specimen. Inspection for cloud point was done and the jacket was replaced. The operation was done without exceeding the time duration of 3 sec. Since the cloud point is the temperature of a liquid specimen when the smallest observable cluster of hydrocarbon crystals first occurs upon cooling under prescribed conditions, observation was done and the cloud point was reported to the nearest 1°C. At this point, a cloud is observed at the bottom of the test jar, which is confirmed by continued cooling (Lalji *et al.*, 2023).



**Figure 9: Bomb calorimeter**

**(xi) Pour point**

Following a specified rate of initial heating, the sample was cooled, and its flow characteristics were checked at intervals of 3°C. The temperature below which the specimen began to move and at which the pour point was noted, is according to ASTM D 97-04 testing method. Figure 10 displays the cloud and pour point tester.



### (xii) Percentage of free fat acid content

The percentage of half of the acidic value represents FFA and is determined by Equation 8.

$$FFA = \frac{\text{Acid value}}{2} \times 100\% \quad (8)$$



**Figure 10: Cloud and pour point tester**

### 3.3 Preparation and Characterization of Nano-silica Additive

According to the method adopted from the literature by Todkar *et al.* (2016), rice husk (RH) was dried, rinsed for 2 h with 1M HCl at 80°C, cleaned, and refluxed. Following a neutralization of the filtrate through washing, the resultant RH was dried for an entire night. Using a digital temperature probe, 100 g of RH were calcinated at temperatures between 650 and 850°C in a muffle furnace. After roughly two hours of heating, white RHA was generated. After the formation process, it was observed that the weight of the resulting white ash was 25 grams, accounting for 25% of the initial mass of the rice husk (RH). This deduction considered the presence of volatile matter. Meanwhile, 200 mL of deionized water was used to dissolve 24 mg of NaOH, yielding 12% NaOH solution. Next, a 1:7 mixture was mixed in a round-bottom flask containing 25 g of RHA and 175 mL of NaOH. After RHA is digested with NaOH at 80–90°C, silica is removed to produce sodium silicate ( $\text{Na}_2\text{SiO}_3$ ) solution. Thereafter, the solution was filtered to get rid of any leftover undigested ash and contaminants that hadn't

burnt. An aqueous  $\text{Na}_2\text{SiO}_3$  the solution is the clear filtrate that remains after precipitation (Equation 9). After that, it was dried for 60 min in an oven set between 100 and 120°C.

Concentrated sulphuric acid ( $\text{H}_2\text{SO}_4$ ) was introduced to a 200 mL beaker that had been filled with gelatinous sodium silicate and held at 85°C until the pH meter indicated that the solution was acidic. As a byproduct, sodium sulphate settled to the bottom and silica precipitated from the solution (Equation 10). To lower the exothermic temperature a tiny amount of water was supplied and the solution was then cooled for 30 mins. Water was then added to the solution to purify it, producing a cake of sodium sulphate and silica that both contained water. Before being weighed and recorded, the solution was allowed to evaporate the water in a variety of round-bottom flasks for 30 min.

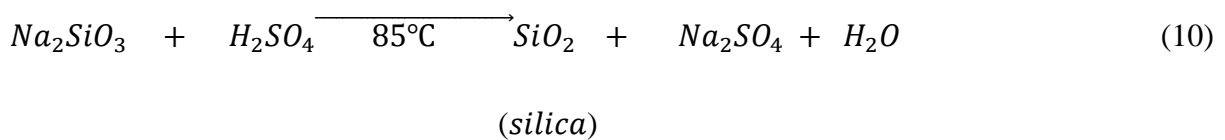
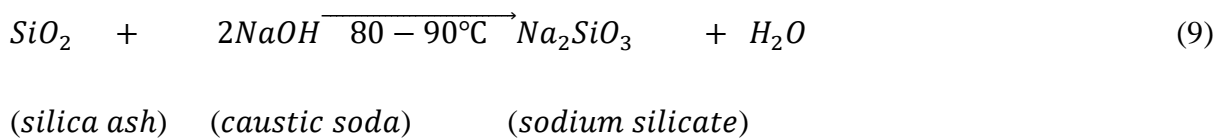
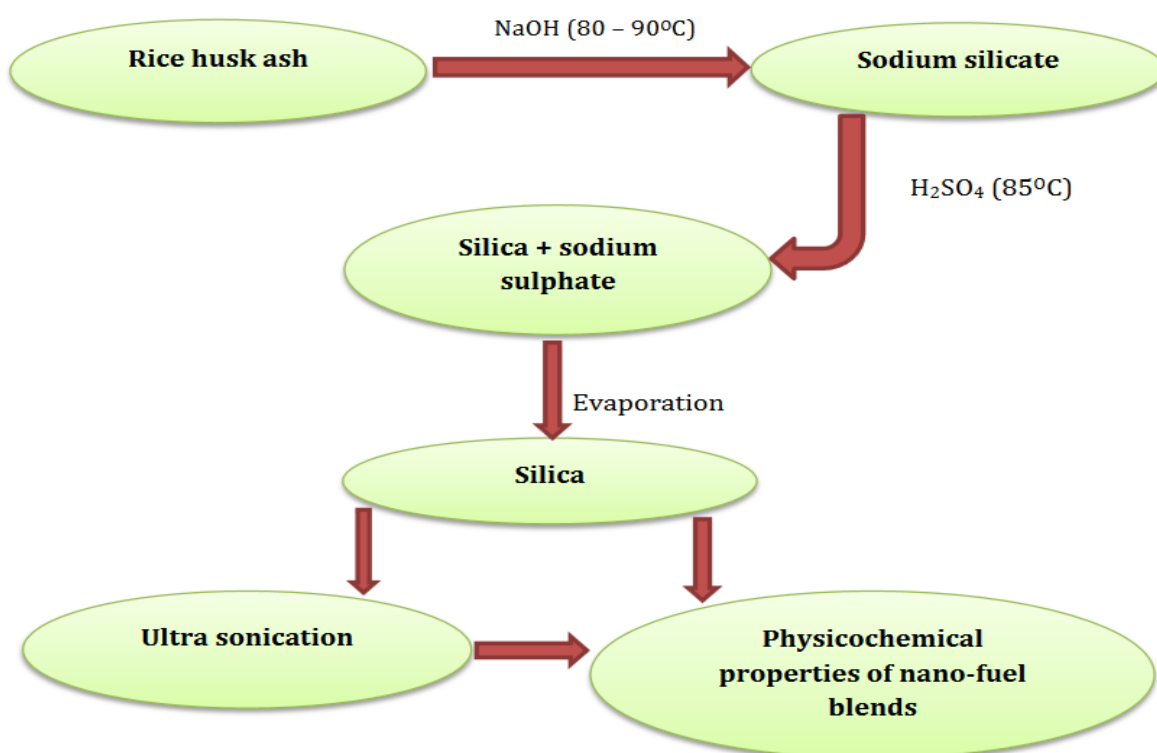


Figure 11 shows a schematic framework for the extraction of nano-silica from RHA and Fig. 12 shows photographs of samples produced. The calcinated rice husk silica (RHS) and rice husk ash (RHA) were characterized using a range of methods. Thermal breakdown was examined using TGA, porosity and texture were assessed using BET, and pore size and volume were ascertained using the BJH technique. The microstructures (morphology) were also examined using SEM, the elemental composition was ascertained using XRF, and the crystallographical structure of the nanoparticles was ascertained using XRD.



**Figure 11: Schematic diagram of extraction of nano-silica from RHA**



**Figure 12: Photographs of (a) RH (b) RHA calcined at 650°C (c) RHS**

### 3.3.1 Nanoparticle Textual Profile

The surface area, pore volume, and pore diameter of the generated RHA and RHS were determined at UDSM using the nitrogen adsorption-desorption isotherm at 77.3 K and Quanta chrome Nova 4200 (Win 1994-2013, v11.03). The BET equation and the 16.2 Å<sup>2</sup> nitrogen molecule cross-section were used to calculate the surface area. The BET equation used to determine the surface area in which at least five data points in the P/P<sub>0</sub> range of 0.025 to 0.30

should be used (Hwang & Barron, 2011; Lapham & Lapham, 2019). Capillary condensation begins at relative pressures greater than 0.5, while at low relative pressures, only monolayer formation occurs. When plotting the BET equation, the graph should be linear with a positive slope.

$$\text{BET equation: } \frac{\frac{P}{P_0}}{n(1-\frac{P}{P_0})} = \frac{1}{n_m C} + \frac{C-1}{n_m C} \left(\frac{P}{P_0}\right) \quad (11)$$

where  $n$  is “the quantity of adsorbate adsorbed”,  $\frac{P}{P_0}$  is “specific relative pressure”,  $n_m$  is “the monolayer capacity” which is the volume of gas adsorbed at standard temperature and pressure (STP) which is defined as 273 K and 1 atm and  $C$  is “the BET constant value”. Least squares regression can be used to calculate the slope and y-intercept. Equation 12 can be used to compute the monolayer capacity  $n_m$ .

$$n_m = \frac{1}{s+i} \quad (12)$$

$s$  is the slope and  $i$  is the y-intercept. Once  $n_m$  is determined, the total surface area  $S_{BET}$  can be calculated using Equation 13.

BET surface area:

$$S_{BET} = \frac{n_m \cdot L \cdot \sigma_m}{V_0 \cdot m} \quad (13)$$

whereby  $\sigma_m$  is “the cross-sectional area of the adsorptive (0.162 nm<sup>2</sup> for N<sub>2</sub>)”,  $L$  is the “Avogadro’s constant”,  $V_0$  is “the molar gas volume of the adsorptive at STP” and  $m$  is “the sample mass”. The textural parameter and porosity strength of BJH were determined by the same techniques, wherein the pore size distribution was calculated to the desorption line of the isotherm at a relative pressure  $\frac{P}{P_0}$ , as shown in Equation 14.

$$r_p = \frac{4.15}{\log\left(\frac{P_0}{P}\right)} + 3.54 \times \left(\frac{5}{\ln\left(\frac{P}{P_0}\right)}\right) 0.333 \quad (14)$$

where  $r_p$  is the pore radius.

### **3.3.2 Thermal Gravimetric Analysis (TGA)**

Using the Linseins thermal analysis apparatus (STA1000), the TGA analysis was carried out. The sample weight was 5.2 mg, and nitrogen was serving as an inert purge at a flow rate of 100 mL/min and a heating rate of 10°C/min over a temperature range of 17.7 to 900°C. RHA was produced by calcinating the precursor for the ground additives in a muffle furnace for 3 h at a ramp rate of 5°C. The resultant RHA was gathered, allowed to cool, and ready for the extraction of silica as a possible nanoparticle addition to enhance the characteristics of fuel. The data obtained in TGA is useful in determining the purity and composition of materials, drying and ignition temperatures of materials, and knowing the stability temperatures of compounds.

### **3.3.3 Fourier Transformation Infrared Spectrometry (FT-IR)**

Micrometric instruments (ASP2020) were employed for nitrogen sorption studies. Functional groups in the sample s (calcinated RHA and extracted RHS) were analyzed by using an FT-IR spectrometer. The model of FT-IR used in this study was Alpha Bruker ATR, the wavenumber ranging from 4000 to 1000  $\text{cm}^{-1}$ . Samples were grounded in a mortar to reduce the average particle size to 1 to 2 microns. About 5 to 10 mg of finely ground samples were then placed onto the face of a KBr plate, a small drop of mineral oil was added and the second window was placed on top.

There are several FTIR sampling techniques available, with the most common being transmission, attenuated total reflectance (ATR), specular reflectance, and diffuse reflectance. Transmission FTIR can be used for liquids, solids, and gases. Sample preparation is typically required for transmission measurements, solid samples may require dispersion in KBr and pressed into pellets, and IR transparent windows, such as  $\text{CaF}_2$  are required for measuring liquids. Placement of samples in such a way can result in non-reproducible spectra due to inconsistency in where the IR beam hits the sample.

### **3.3.4 Crystallographic, Morphological, and Elemental Analysis**

The X-ray Diffractometer model “Bruker AXS (Siemens) D5005, Bruker AXS GmbH” made in Germany, was employed for the determination of spectral analysis of RHA and RHS. XRD covers a wide range of applications on samples with a low degree of orientation. Combined with the powerful DIFFRAC.SUITE software the D8 DISCOVER Plus enables the simple execution of XRD applications such as Phase Identification, Phase Quantification, Structure Solution, Pair Distribution Function Analysis, and Small Angle X-ray Scattering (SAXS). An

X-ray fluorescence (XRF) spectrometer was coupled to this apparatus to ascertain the elemental composition of RHA. Morphological analysis of RHA and RHS was performed by scanning electron microscope (SEM) by displaying images at a magnification of 4400× resolution.

### 3.4 Synthesis of Biodiesel by Transesterification Process

Synthesis of biodiesel depends on the amount of FFA in ADSO. A two-step transesterification process is required to convert high-FFA oils to monoesters (Bakhtawar *et al.*, 2022). The FFA of ADSO was 3.8% higher than 2% and the two-step transesterification was employed. In the first step (esterification process) as shown in Fig. 13, the purpose was to lower the FFA level of ADSO below 2%, 100 g of oil was pre-treated at 60°C using an acid catalyst (0.5% H<sub>2</sub>SO<sub>4</sub> w/w<sub>oil</sub>) and 10 mL of methanol. In the second step (transesterification process), 800 mL of oil with FFA below 2%, 100 mL of methanol, and 1.5 wt% NaOH pellets were used to produce biodiesel. The reaction temperature was set at 65°C, with an 8:1 methanol to oil molar ratio, an agitation speed of 1500 rpm, and a reaction period of 4 h (Kapile *et al.*, 2022). The synthesized ADME was kept in storage to examine physicochemical properties.

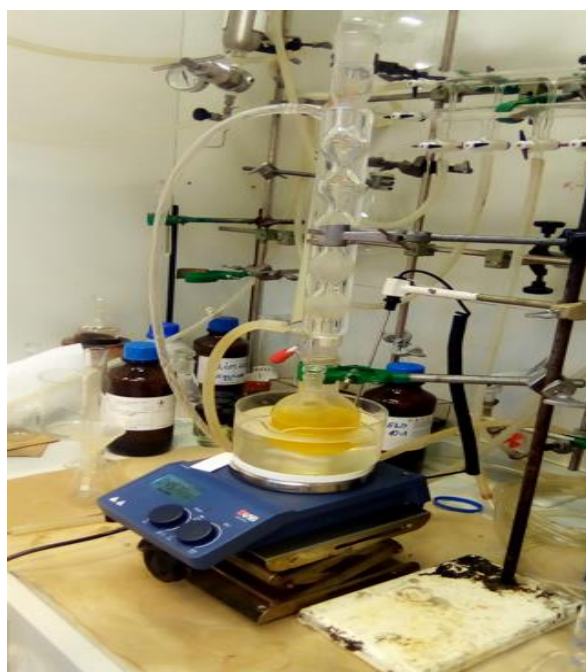


**Figure 13: Transesterification process**

#### 3.4.1 Optimization of Biodiesel Production

Reaction temperature, methanol-to-oil molar ratio, and reaction time have an impact on biodiesel production. The effects of these parameters on biodiesel production are investigated

in this study. The percentage yield was used as the criterion for reporting optimal conditions. The optimal value for each parameter was determined by holding the other parameters constant. As adopted by a previous report by Nabora *et al.* (2019) on altering the methanol to oil molar ratios (1:2, 1:4, 1:6, 1:8, 1:9, and 1:12) and adjusting the amount of catalyst and time to 1.5 wt% and four hours, respectively, the first phase of the reaction was optimized to produce the maximum amount of biodiesel. For optimal results, a methanol-to-oil ratio of 1:8 was used. Experiments were carried out with a constant catalyst quantity to find the best values for the other parameters. The biodiesel that was produced under optimal conditions was physicochemically analyzed and recorded.

### **3.4.2 Determination of Fuel-Related Properties of ADME**

Using Pensky-Martens open or closed cup testers in compliance with ASTM test methods D92 and D93-90, respectively, the produced fuel's properties, including its flash point, were measured. Using the cloud and pour point equipment, the kinetic viscosity at 40°C was measured using the Redwood viscometer (ASTM D445), and the density at 15°C was determined using the densitometer (ASTM D5002). The pour (ASTM D97), and the cloud point (ASTM D2500) using the cloud and pour point equipment. The Cd 12c-16 test method, developed by the American Oil Chemists Society, was utilized to conduct oxidation stability analysis. Using the OXITEST Oxidation Test Reactor (Make: VELP SCIENTIFICA, Model: F30910248 (D7462)), the oxidative stability of newly produced biodiesel with and without varying dopant concentrations of nanoparticles was examined. The test method used to determine the CN was ASTM D613.

### **3.4.3 Fat Acid Composition of ADME**

The fatty acid composition was determined using gas chromatography (GC 7890A, Agilent Technologies) equipped with a flame ionization detector. The capillary column was 30 m in length, with a film thickness of 0.25  $\mu\text{m}$ , and with an internal diameter of 0.25 mm. An amount of 0.5 g of oil was suspended in 1 mL of toluene for the acid-catalyzed transesterification reaction that produced FAME. The vials were sealed after 2 mL of methanolic  $\text{H}_2\text{SO}_4$  (1% v/v) was added. The reaction mixture was kept at 50°C overnight in a stoppered tube (16 h). After adding 2 mL of water, 2% w/v potassium bicarbonate was added to reduce the level of FFA. Then 25 mL of dichloromethane was used to extract the trans-methylated fatty acids, and anhydrous sodium sulphate was used to eliminate any trace water. The organic solvent

evaporated at a lower temperature. About 1 mL solution of dichloromethane was used to dissolve 1 mg of the sample for analysis using GC-MS.

### **3.5 The Effect of Nano-particle Additives on the Fuel Properties of ADME and its Blends**

Standard ASTM D6751 testing methods were used to determine kinematic viscosity, oxidation stability, flash point, CN, cloud, and pour points. Under optimal conditions, the biodiesel synthesized was doped with SiO<sub>2</sub> nanoparticles at intervals of 200 ppm with various concentrations from 400 to 1000 ppm. The potential fuel properties were analyzed in this study. A comparison of the fuel properties of ADME was also performed by blending commercial alumina and manufactured nano-silica additives with which Al<sub>2</sub>O<sub>3</sub>/SiO<sub>2</sub> (400/400 ppm dosage) was used for determining flash point, oxidation stability, and CN, however, the dosage of 200/200 ppm used for kinematic viscosity Ultrasonication process was used to produce a well-mixed homogeneous nano-fuel solution from fuel blending of B100+ SiO<sub>2</sub>, B20+SiO<sub>2</sub>, and B20+Al<sub>2</sub>O<sub>3</sub>.

#### **3.5.1 Preparation and Physicochemical Properties of Nano-Fuel Blends**

Ultrasonication is a unique homogenization technique utilized in a variety of applications. It is a process that breaks large particles into smaller fragments or better uniform-sized particles in the base fluid. It was employed in this investigation to create a well-mixed nano solution. For the ultrasonication process, SDS surfactant was used to stabilize the blend. In the ultrasonication bath, 20 vol% ADME was blended with diesel for 60 min., and an ultrasonication probe at 15–30 Hz was used to mix the blend further as displayed in Fig. 14. Afterward, the biodiesel blend was steadily mixed with SiO<sub>2</sub> nano-additives and SDS surfactant using a magnetic stirrer at 60°C for 30 min to eliminate traces of water molecules (Gavhane *et al.*, 2021). The same ultrasonication methods were then used to ensure that SiO<sub>2</sub> nano-additives were evenly dispersed in the biodiesel–diesel fuel blends. This method was previously used in the literature by Gavhane *et al.* (2021). Nano-fuel blends' potential fuel properties were determined using ASTM-approved methodology and procedures such as density, kinematic viscosity, flash point, and calorific value. These physicochemical properties of synthesized biodiesel and its fuel blends were assessed using ASTM D6751 and ASTM D7467 standards limits, respectively.



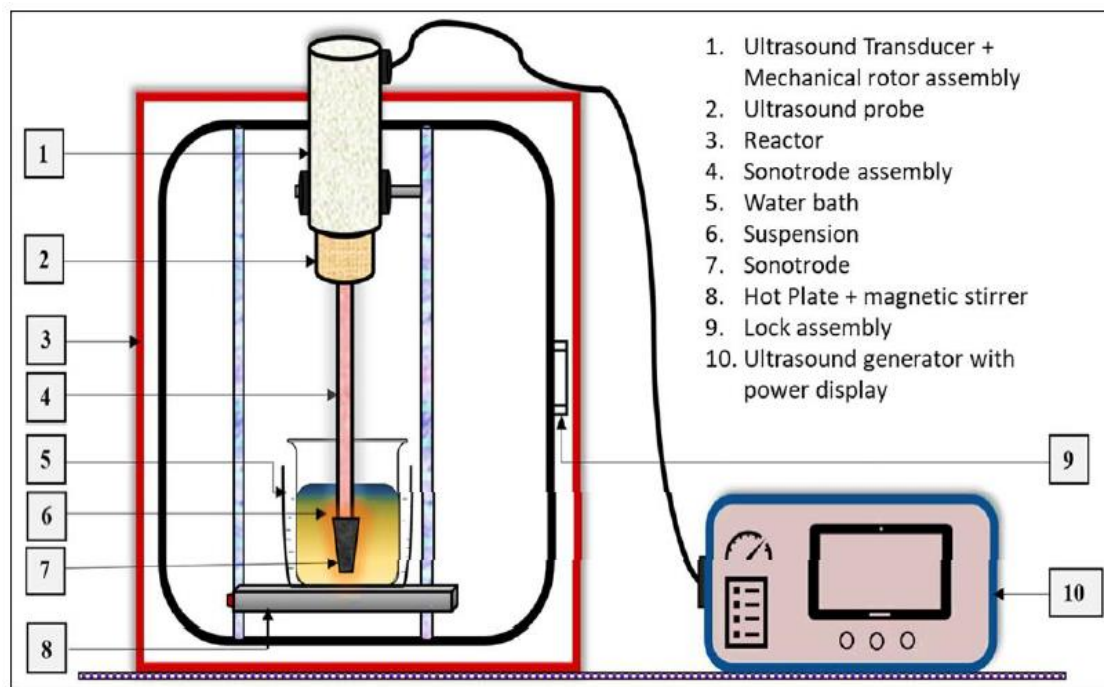


**Figure 14:** Schematic diagram of ultrasound-assisted preparation unit (Gavhane *et al.*, 2021)

### 3.6 Engine Performance, Exhaust Emissions, and Combustion Testing

#### 3.6.1 Engine Test Setup and Procedure

The engine used in the present study was a naturally aspirated, 3-in-line, IVECO AIFO 8031 i06.05, 4-stroke diesel engine with direct injection. Tests were conducted at fixed injection timing of diesel fuel. Samples that were tested include pure ADME (B100), fuel blends B20, B20+SiO<sub>2</sub>, and B100+SiO<sub>2</sub> which were dosed with 400 ppm of SiO<sub>2</sub> nanoparticle additives, and conventional diesel (B0), which was used as a base fuel for comparison tests. The engine test-up is shown in Fig. 15 and Table. 4 contains technical specifications for the engine. In the tests, a CI engine (1) was used to operate an M8B 160 Asynchronous generator (3) loaded with different resistors while the engine throttling and generator settings were controlled by a personal computer. One piston cylinder was coupled with, a pressure transducer (10) of type Kistler KIAG 6005. The pressure transducer's cylinder pressure signals were amplified by a charge amplifier type: Kistler 5018A1000) and coupled to a data acquisition card type: NI USB-6361-based indicator system for data collection. An incremental crank angle transducer-optical encoder (11) of type: Hengstler RI 32-0/1024 ER.14KA was used to externally trigger the data acquisition system 1024 times in one revolution. Fuel tanks (5) with an AVL-7030 fuel balance system supplied the fuel while controlled by a fuel flow meter. When changing

fuel, the engine fuel filter and fuel balance were drained and new fuel was added until the system was full. The engine was then started and left running for a few minutes to allow the fuel lines to drain and the system to stabilize.

Horiba MEXA-8120F and PG 250 (NDIR, H.FID, and HCLDC) exhaust gas analyzer (EGA) (8) modules were used to measure CO, THC, and NO<sub>x</sub>, and an AVL 415 (variable sampling) smoke meter (7) connected to the engine exhaust pipe was used to measure soot emissions. The emission data were recorded when the measured values stabilized. Brake power (BP) was applied at a constant engine speed of 1500 rpm for an interval of 4 kW between 0 and 20 kW. The heat release was then calculated using the equation of the conventional one-zone for a quasi-static open system first law of thermodynamics and measured values of cylinder pressure and crank angle.

**Table 4: Engine specification profile**

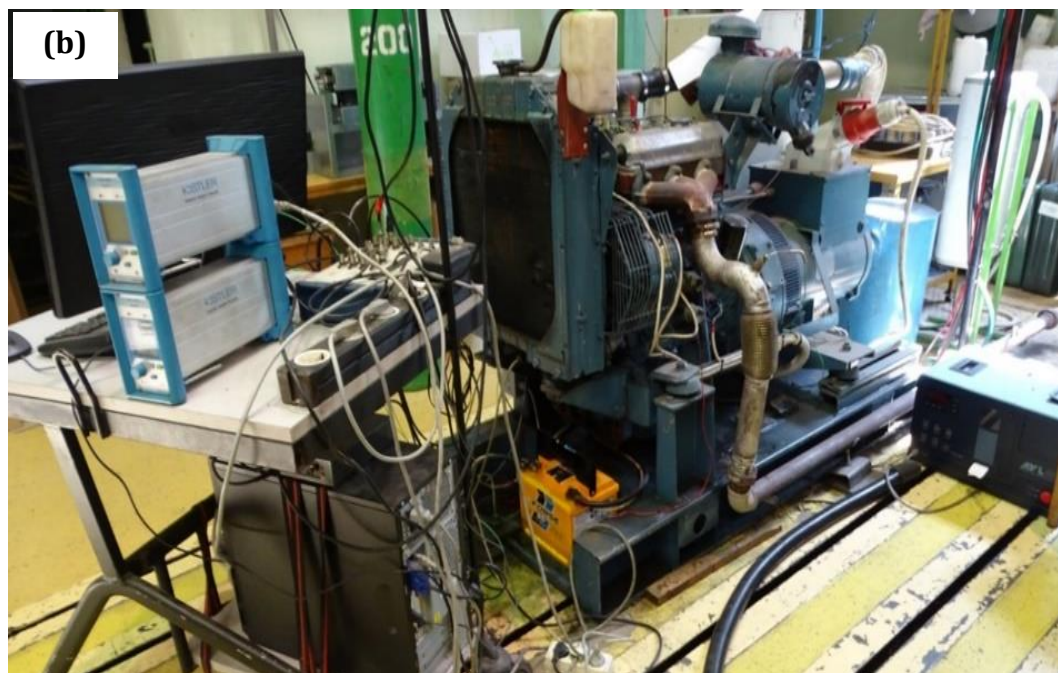
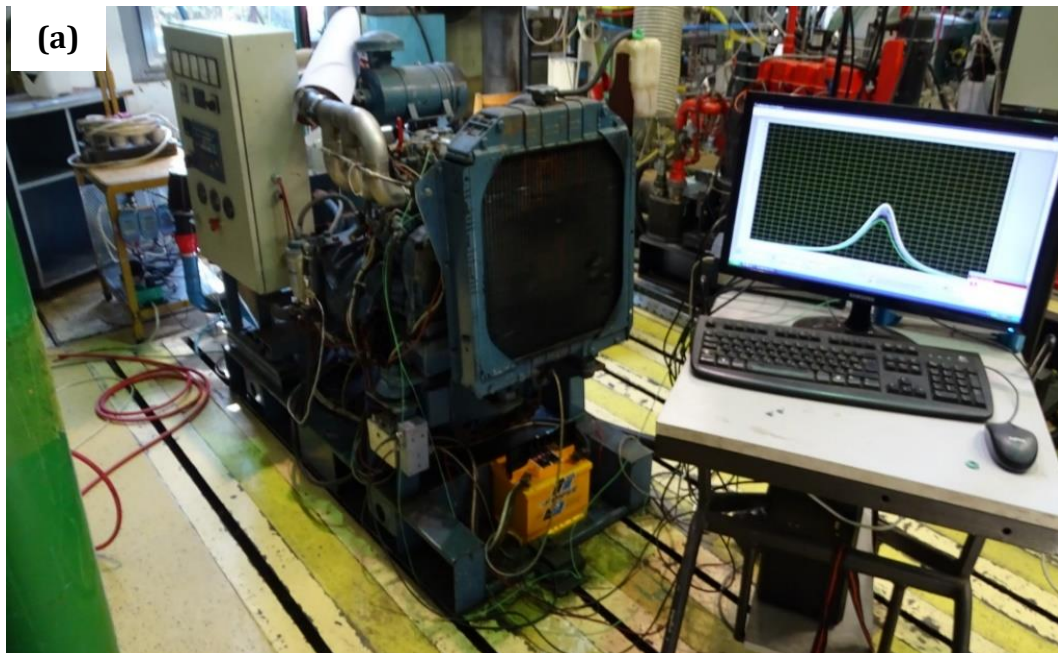
Engine parameters	Details
Engine model	IVECO AIFO 8031 i06.05
Engine type	4- stroke air cooled
Number of cylinders	3 inline
Combustion system	Direct injection
Bore/stroke	104 mm/115 mm
Compression ratio	17:1
Displacement volume	2.9 dm <sup>3</sup>
Maximum power	29 kW, at 1500 rpm

### 3.6.2 Engine Performance Characteristics

A diesel engine's performance characteristics define its efficiency, reflecting how well fuel energy is transformed into useful work and cost-effective operating points. Diesel engine performance characteristics such as EGT, BTE, and BSFC were measured for pure diesel and biodiesel nano-fuel blends each by varying engine brake powers (BP) to check the optimum compression ratio and to obtain minimum specific fuel consumption, better efficiency, and lesser emission.

Generally, BP is the power available at the engine crankshaft for doing useful work. It is sometimes known as engine output power. Brake thermal efficiency (BTE) is the ratio of the power available at the crankshaft to the input fuel energy in appropriate units. It can be calculated using Equation 15 by measuring the amount of fuel consumed per second and recording the lower heating value of the fuel.

$$BTE = \eta_B = \frac{\text{Brake power}}{\text{Fuel consumption} \times \text{Lower Heating Value}} = \frac{Bp}{\dot{m}_f \times LHV}(\%) \quad (15)$$



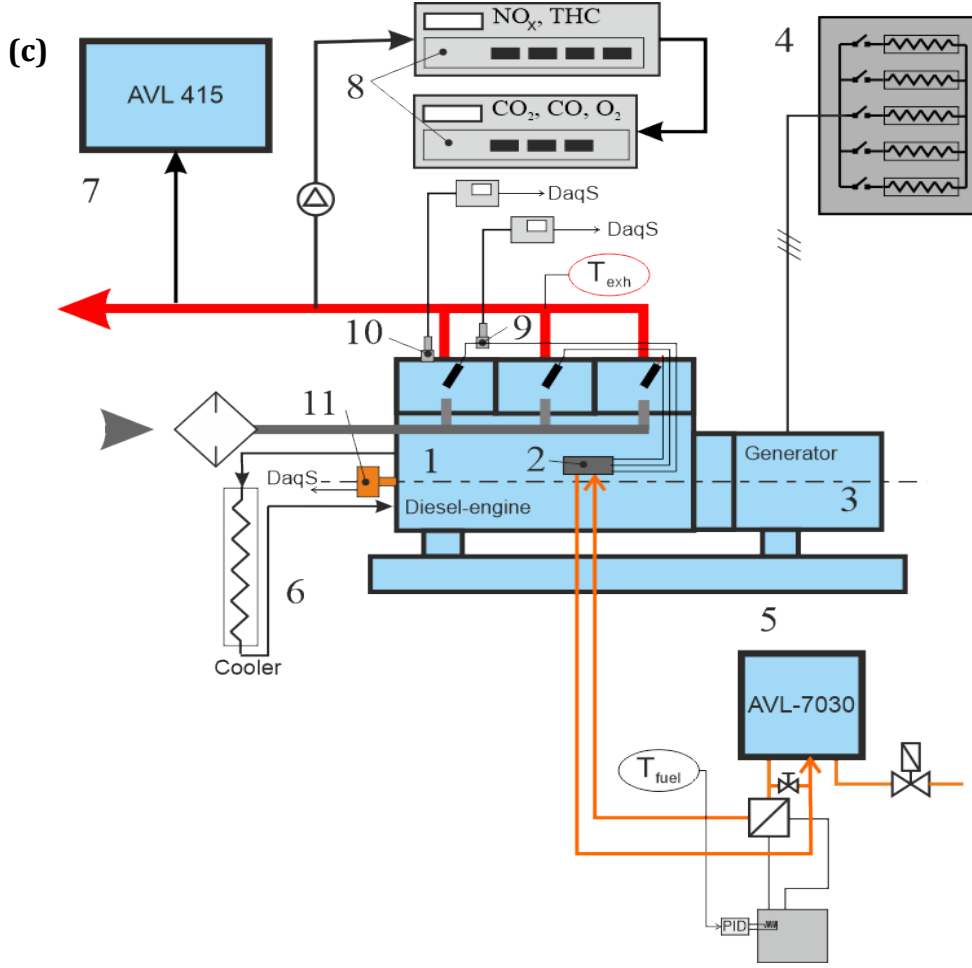


**Figure 15: Engine (a) front (b) backward view photograph (c) test rig setup**

1. Engine 2. Distribution injection system 3. Asynchronous generator 4. Artificial water-cooled load 5. AVL fuel balance 6. Air cooler 7. Smoke meter 8. Exhaust gas analyzer 9. Injection tube pressure transducer 10. Cylinder pressure transducer 11. Crank angle encoder

Brake-specific fuel consumption (BSFC) is the amount of fuel consumed by an engine for one unit of shaft power production. BSFC is used to express the fuel efficiency of the CI engine. Its SI units correspond to the inverse of the units of specific energy which is  $\text{kg/J} = \text{s}^2/\text{m}^2$ . BSFC can be calculated by Equation 16.

$$BSFC = \frac{\text{mass flow rate of fuel}}{\text{Brake power}} = \frac{\dot{m}_f}{BP} (\text{kg/kWh}) \quad (16)$$

$$\text{In which } \dot{m}_f = V_f \times \rho_f \times \frac{3600}{t} (\text{kg/h}) \quad (17)$$

where  $V_f$  is a volume of fuel that was  $50 \text{ cm}^3$ ,  $\rho_f$  is fuel density and  $t$  is the time measured until  $50 \text{ cm}^3$  of fuel is consumed, measured in sec.

### 3.6.3 Engine Combustion Characteristics

Pressure rise rate (PRR), Cylinder gas pressure (CGP), and heat release rate (HRR). Test fuel burning characteristics were investigated using the following combustion parameters: Mass fraction burned curve, ignition delay (ID), and crank angles for combustion phasing and duration. Brake means effective pressure (BMEP). The hypothetical/average pressure that is assumed to be acting on the piston throughout the power stroke is known as BMEP and therefore, BMEP can be calculated using Equation 18. It can also be calculated by dividing the work done by the engine during one cycle by the displacement volume.

$$BMEP = \frac{\text{Brake power}}{lank/2} \quad (18)$$

Where  $a$  is the in-cylinder area;  $l$  is the stroke length;  $n$  is the engine rotational speed;  $k$  is the number of cylinders; numeric 2 applies to a 4-stroke engine. Heat release rate (HRR) is influenced by the mixture formation, combustion rate, and ignition delay (ID) in the premixed combustion phase. The HRR was calculated based on the measured in-cylinder pressure data and crank angle readings. It indicates how much heat is released during combustion. It usually refers to the burnt mass of fuel and is expressed in kilowatts per square meter. The basis for determining the HRR was the energy conservation law and the equation of state. After rearranging and simplifications, HRR was calculated using Equation 19.

$$\frac{dQ}{d\theta} = \frac{\gamma}{\gamma-1} \times P \frac{dV}{d\theta} + \frac{1}{\gamma-1} \times V \frac{dP}{d\theta} \quad (19)$$

Where  $\frac{dQ}{d\theta}$  is HRR;  $\frac{dP}{d\theta}$  is the in-cylinder pressure variation with respect to crank angle;  $P$  is the cylinder gas pressure;  $V$  is the volume ( $m^3$ );  $\gamma$  is the specific heat ratio which was calculated by Equation 20.

$$\gamma(T) = 1.56 - 6 \times 10^{-5} \times T + 10^{-8} \times T^2 \quad (20)$$

with the measured pressure data and the calculated cylinder volume, the cylinder gas temperature can be obtained by the following Equation 21.

$$T = \frac{T_r \times P \times V}{P_r \times V_r} \quad (21)$$

In which  $P_r$ ,  $T_r$ , and  $V_r$  can be determined at a given reference condition.

### 3.6.4 Exhaust Emission Characteristics

Using different tested fuels and engine BP, exhaust gas analyzer type Horiba, MEXA-8120F was used to measure the exhaust emissions in which Horiba, PG 520 measures CO and CO<sub>2</sub> emission and THC by Horiba, MEXA 8120 F also NO<sub>x</sub> by Horiba, MEXA 8120. Smoke opacity was measured by smoke meter type AVL-415. Engine design parameters, such as engine type, size, injection pressure, and combustion chamber type, affect how these pollutants form), in addition to fuel quality and operating circumstances. For instance, combustion chamber modifications have the potential to reduce unwanted fuel spread and fuel impingement on walls, which further lowers the CO, THC, and soot emissions (Vergel-Ortega *et al.*, 2021).

### 3.7 Uncertainty Analysis

Errors and uncertainties can arise from a variety of variables such as instrument selection and calibration, changing ambient conditions, testing, observations, and also in measuring weight, length, and time. In general, uncertainty may be divided into two types: fixed mistakes and random errors. The former scenario is concerned with repeatability, whereas the latter is concerned with analytical measures. Table. 5 depicts the uncertainties of several instruments employed in this experimental work, while Table 6 depicts uncertainties in measured values. The uncertainty of the measured variable ( $\Delta X$ ) is calculated using the Gaussian distribution, as given in Equation 22, within the confidence limits of  $\pm 2s$ . The  $2s$  is the mean limit on which 95% of measured values rely.

$$\Delta X_i = \frac{2\sigma_i}{\bar{X}_i} \times 100\% \quad (22)$$

Where,  $X_i$  is the number of readings,  $\bar{X}_i$  is experimental reading and  $\sigma_i$  is the standard deviation. The uncertainties of calculated parameters were calculated using Equation 23.

$$R = f(X_1, X_2, X_3 \dots \dots \dots X_n) \quad (23)$$

$$\Delta R = \sqrt{\left[\left(\frac{\partial R}{\partial X_1} \Delta X_1\right)^2 + \left(\frac{\partial R}{\partial X_2} \Delta X_2\right)^2 + \left(\frac{\partial R}{\partial X_3} \Delta X_3\right)^2 + \dots \dots \left(\frac{\partial R}{\partial X_n} \Delta X_n\right)^2\right]} \quad (24)$$

Where  $R$  is the function of  $X_1, X_2, \dots X_n$  and  $X_1, X_2, X_3 \dots X_n$  represents the number of readings taken. Hence  $\Delta R$  is computed by the root mean square of errors of measured parameters by using Equation 24.

**Table 5: Descriptions of instruments used with their accuracy**

<b>Instrument</b>	<b>Description</b>	<b>Range</b>	<b>Accuracy</b>
Fuel flow measuring system	AVL-7030 fuel balance	0.5-25L/h	$\pm 0.1$
CO analyzer	Horiba, PG 520	0-5000ppm	$\pm 1$
CO <sub>2</sub> analyzer	Horiba, PG 520	0-20 V/V%	$\pm 1$
THC analyzer	Horiba, MEXA 8120 F	0-5000ppm	$\pm 2.1$
NO/NO <sub>x</sub> analyzer	Horiba, MEXA 8120	0-5000ppm	$\pm 0.5$
Smoke meter	AVL 415	0-100%	$\pm 3$
Piezo transducer	Kistler KIAG 6005	-	$\leq \pm 0.8(\%FSO)$
Charge amplifier	Kistler KIAG 5001	-	-
Crank angle speed encoder	Hengstler RI 32-0/024 ER.14KA	0-360°	$\pm 0.35^\circ$

**Table 6: Uncertainties in measured parameters**

<b>Measured parameters</b>	<b>Uncertainty (%)</b>
Brake power (kW)	0.24%
Fuel flow rate	0.74%
THC (ppm)	0.2%
CO (%)	0.1%
CO <sub>2</sub> (V/V%)	0.3%
NO <sub>x</sub> (ppm)	0.2%
EGT (°C)	0.75%
Smoke (mg/m <sup>3</sup> )	0.6%

## CHAPTER FOUR

### RESULTS AND DISCUSSION

#### 4.1 Characterization of ADSO

Table. 7 displays an overview of the major fuel characteristics of ADSO. To ascertain the physicochemical parameters of ADSO, AOCS -CD1-25 and OCS CD3-25 Official Methods were applied. It was discovered that *A. digitata* seeds contained 42.3% oil, which is enough to make biodiesel. This content is slightly higher than the previous study reported by Nabora *et al.* (2019) in which the oil content was 36.2% extracted from *Parinari curatellifolia* seeds. This is probably associated with locality and environmental factors.

**Table 7: Physicochemical properties of ADSO**

Property	Units	ADSO
Oil content	%	42.3
Acidic value	mgKOH/g	1.55
Moisture content	ppm	260-283
Density @15°C	kg/m <sup>3</sup>	919.4
Iodine value	gI <sub>2</sub> /100g	84.4
Cetane number (min.)	-	47.8
Free fat acid (FFA)	mgKOH/g	0.78
Saponification value	mgKOH/g	210.35
Kinematic viscosity at 40°C	mm <sup>2</sup> /s	38.4

The relatively high AV suggests a high concentration of FFA. The result recorded 3.8% of FFA which is more than 2% to cause soap to develop and in turn reduces biodiesel yield (Eevera *et al.*, 2009). The AV was 1.55 mgKOH/g more than those recorded by Mohammed (2018) which was 0.47 mgKOH/g, but less than 2.75 mgKOH/g as observed by Abubakar *et al.* (2015). The SV was 210.35 mgKOH/g which is less than that observed by Mohammed, (2018) which was 338.49 mgKOH/g.



## 4.2 Optimization of Biodiesel Synthesis

### 4.2.1 Effect of Methanol to Oil Molar Ratio on Biodiesel Yield

The alcohol-to-oil molar ratio is a potential factor in the transesterification process. Normally, excess methanol speeds up the transesterification process (Narowska *et al.*, 2019). In this work, the methanol-to-oil molar ratio was varied from 2:1 to 4:1, 6:1, 8:1, 9:1, and 12:1 and was investigated with a conversion of triglycerides by 4 h reaction time, 1.5 wt% of catalyst, 3000 rpm stirring speed and 65°C reaction temperature (Nabora *et al.*, 2019; Kapile *et al.*, 2022). The methanol to oil ratio was found to be 1:8, with 94% biodiesel yield from the ADSO under optimum operating conditions, as illustrated in Fig.16(a). The ratio of 1:2 produced the least amount of biodiesel, with a yield of 64%. If it changed from 1:2 to 1:8, the yield rose; however, if it was changed from 1:8 to higher, the yield decreased. When there is too much alcohol in the reaction mixture, it frequently becomes more polar. Glycerine was widely dissolved as the concentration of methanol rose, which prohibited methanol from reacting with the catalyst and hindered the process of separating biodiesel from glycerine. This finding concurs with the previous study reported by Mohadesi *et al.* (2022).

### 4.2.2 Effect of Reaction Time on Biodiesel Yield

Under constant operating circumstances, the effects of various conditions such as 1, 2, 3, 4, 5, and 6 h on the yield of biodiesel were assessed for reaction temperature (65°C), the stirring rate (1500 rpm), catalyst amount (1.5 wt%) and methanol to oil ratio (1:8). The following are the results, as shown in Fig. 16(b): The biodiesel yields increased as the reaction temperature increased, reaching a maximum of 94% in 4 hours. The sluggish reaction was caused by the methanol's dispersion and mixing in oil, and at some point, throughout the reaction time, the production of biodiesel increased from 1 to 4 h. Because the chemical reaction involved in producing biodiesel is usually reversible, the yield of biodiesel can be decreased if the biodiesel bonds break longer than 4 h after the biodiesel is formed. Excessive mixing time, on the other hand, reduces product yield due to the backward reaction, resulting in a loss of esters and more fatty acids forming soaps (Encinar *et al.*, 2018).

### 4.2.3 Effect of Reaction Temperature on Biodiesel Yield

It is crucial to determine the optimal temperature for the transesterification reaction when making biodiesel. Fig. 16(c) shows how temperature affects biodiesel yield. The results show that raising the temperature increases the production of biodiesel. The highest yield (92%) for

biodiesel production was achieved at 65°C, raising the temperature over 65°C, however, lowers the yield since methanol can escape (vaporize) at 64.7°C and so does not participate in the chemical reaction. This result was probably similar to that reported by Taherkhani & Sadrameli (2018) in which linseed oil was optimized during the transesterification process.

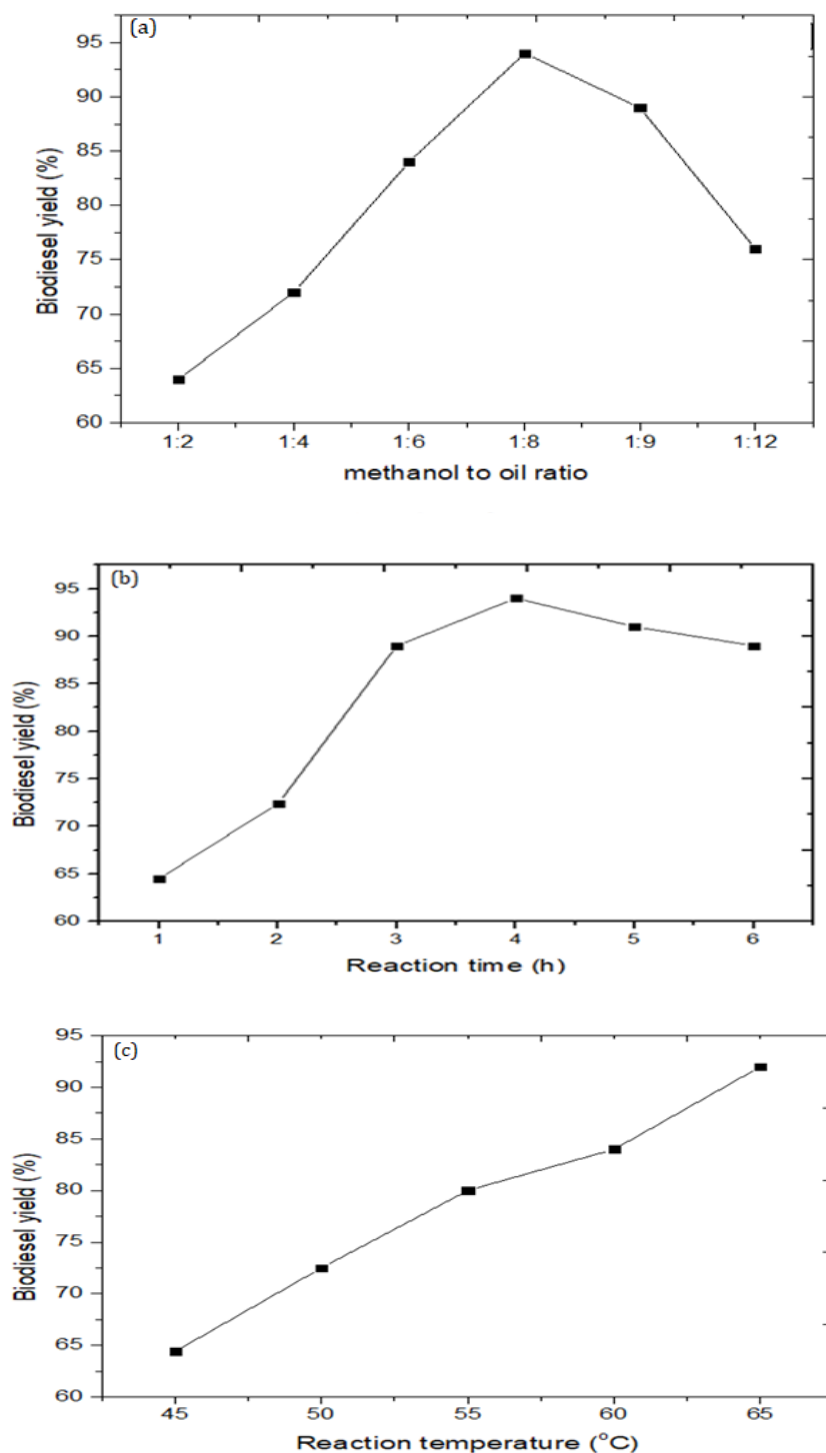


**Figure 16: Influence of (a) methanol to oil ratio (b) reaction time (c) reaction temperature on biodiesel yield**

### 4.3 Physicochemical Properties of ADME

According to EN 14214 and ASTM D6751 standard limits, the characteristics of ADME made from ADSO were assessed. The results are presented in Table 8. As per ASTM and EN standards, the following parameters were found to be within acceptable limits: CN was 56, pour point was found to be -1°C, which is slightly lower than that reported by Lamayi *et al.* (2016) which was -1.5°C. Kinematic viscosity was 4.62 mm<sup>2</sup>/s, which is higher than that reported by Lamayi *et al.* (2016) which was 3.144 mm<sup>2</sup>/s. Cloud point (3°C), which was lower than that observed by Buhari *et al.* (2014) who reported 10°C for the same plant. The calorific value (43.8 MJ/kg) was almost similar to that obtained by Lamayi *et al.* (2016) which was 44.063 MJ/kg for the same plant. Density (884 kg/m<sup>3</sup>), which was slightly lower than that reported by Buhari *et al.* (2014) who observed 886.6 kg/m<sup>3</sup>. Flash point (182°C) was higher compared to that obtained by Buhari *et al.* (2014) and Lamayi *et al.* (2016) which were 170 and 160°C respectively. Oxidation stability was 3.08 h, the low oxidation stability could most likely be attributed to the high quantity of unsaturated fatty acids in ADME as shown in Table 8.

**Table 8: Physicochemical properties of ADME**

Test	ASTM D6751	EN 14214	Diesel	ADME
Kinematic viscosity at 40°C (mm <sup>2</sup> /s)	1.9 – 6.0	3.5 - 5.0	2.0 - 4.5	4.62
Density (kg/m <sup>3</sup> )	860 - 900	860 - 900	850	884
Flash point (°C)	>130	>101	60 - 80	182
Cloud point (°C)	-3 to 12		-15 to -5	3
Pour point (°C)	-15 to 10		-35 to -15	-1
Cetane number (minimum)	>47	>51	54.6	56
Oxidation stability at 110°C(h)	>6	>3		3.8
Calorific value (MJ/kg)	42 - 46		45	43.8

#### 4.3.1 Composition Profile of FFA in ADME

Table 9 provides an overview of the FFA composition of ADME. Different ratios of saturated and unsaturated fatty acids make up ADME. The overall fatty acid composition consisted of 78.84% unsaturated fatty acids (Eicosenoic, Docosenoic, Linoleic, Heptadecanoic, and Oleic acids) and 21.16% saturated FFA (Myristic, Palmitic, Behenic Stearic, Tricosanoic,

Lignoceric, and Pentadecanoic acid). This was quietly different from the previous study reported by Mohammed (2018) in which saturated FFA in ADME was found to be 50.8% which is slightly greater than in unsaturated FFA which is 47.53%. In *Moringa* biodiesel the level of unsaturated FFA is greater than that of saturated which is 83 and 17% respectively as reported by Fernandes *et al.* (2015).

**Table 9: Composition of FFA in ADME by GC-MS analysis**

Fatty acids	Composition	Chemical formula	Composition (wt%)
Lignoceric acid	C24:0	$\text{CH}_3(\text{CH}_2)_{22} \text{COOH}$	0.714
Behenic acid	C22:0	$\text{CH}_3(\text{CH}_2)_{20} \text{COOH}$	1.366
Palmitic acid	C16:0	$\text{CH}_3(\text{CH}_2)_{14} \text{COOH}$	12.938
Tricosanoic acid	C23:0	$\text{CH}_3(\text{CH}_2)_{21} \text{COOH}$	3.944
Stearic acid	C18:0	$\text{CH}_3(\text{CH}_2)_{16} \text{COOH}$	0.968
Heptadecanoic acid	C17:1	$\text{CH}_3(\text{CH}_2)_{14} \text{CH}_2 \text{COOH}$	47.422
Linoleic acid	C18:2	$\text{CH}_3(\text{CH}_2)_7 \text{C}_2 \text{H}_2 (\text{CH}_2)_7 \text{COOH}$	29.959
Eicosenoic acid	C19:1	$\text{CH}_3(\text{CH}_2)_{16} \text{CH}_2 \text{COOH}$	0.597
Oleic acid	C18:1	$\text{CH}_3(\text{CH}_2)_7 \text{C}_2 \text{H}_2 (\text{CH}_2)_7 \text{COOH}$	0.570
Myristic acid	C14:0	$\text{CH}_3(\text{CH}_2)_{12} \text{COOH}$	0.989
Pentadecanoic acid	C15:0	$\text{CH}_3(\text{CH}_2)_{13} \text{COOH}$	0.239
Docosenoic acid	C22:1	$\text{CH}_3(\text{CH}_2)_7 \text{CHCH}(\text{CH}_2)_{11} \text{COOH}$	0.294
Saturated FFA			21.16
Unsaturated FFA			78.84
Total FFA			100

#### 4.3.2 Physicochemical Properties of Nano Fuel Blends

Table 10 summarizes the important calculated fuel-related properties that showed it met the global biodiesel standards' minimum requirements. The kinematics viscosity of B100+SiO<sub>2</sub> (4.60 mm<sup>2</sup>/s) meets the requirements of ASTM D6751 standard limits (1.9 - 6 mm<sup>2</sup>/s). The density of B20+SiO<sub>2</sub> and B100+SiO<sub>2</sub> were observed to be 844, and 884.3 kg/m<sup>3</sup>, which shows

an increase of 0.12 and 0.03% compared to B20 and B100 respectively. The calorific value of B0, B100+SiO<sub>2</sub>, and B20+SiO<sub>2</sub> was observed to be 45, 44.3, and 44.5 MJ/kg which shows an improved increase of 2.67, 1.57, and 1.13% respectively, compared to B100 (43.8 MJ/kg). Generally, fuels having high kinematic viscosity, on the other hand, during injection generate larger droplets, which might contribute to inefficient combustion. As a result of the biodiesel fuel's uneven combustion properties, the engine's lifespan will be reduced (Chidambaranathan *et al.*, 2020). On another hand, flash points of B0, B20+SiO<sub>2</sub>, and B100+SiO<sub>2</sub> obtained were at 65.5, 76, and 73°C respectively which were lower compared to B100 (182°C). Previous research reported by Mohammed (2018) showed density, kinematic viscosity, calorific value and flash point of B20 for the same plant were 851.9 kg/m<sup>3</sup>, 3.6 mm<sup>2</sup>/s, 44.354 MJ/kg, and 76°C respectively.

**Table 10: Physicochemical properties of ADME (ASTM D6751) and its blends (ASTM D7467)**

Property (unit)	ASTM D7467	ASTM D6751	B0	B20	B100	B20+SiO <sub>2</sub> (400 ppm)	B100+SiO <sub>2</sub> (400 ppm)
Viscosity@40°C(mm <sup>2</sup> /s)	1.9-4.1	1.9-6.0	2.45	3.2	4.62	3.40	4.60
Density at 15°C (kg/m <sup>3</sup> )	886.4	860-900	840	843	884	844	884.3
Calorific value (MJ/kg)	-	42-46	45	44.2	43.8	44.5	44.3
Flash point (°C)	<52	>130	65.5	68	182	76	73

#### 4.4 Physicochemical Properties of Nanoparticle Additives

##### 4.4.1 The FT-IR Spectral Analysis

The extracted silica and RHA FT-IR spectra were displayed as shown in Fig. 17. The O-H group stretching vibration is shown in Fig. 17(a) at a high-intensity broadband of 3387.6 cm<sup>-1</sup>. The O-H groups absorb more energy during stretching than the C-H groups because they are more polar but it vanished in Fig. 17(b) as a result of calcination at 650°C and burning in the air. At 3379.7 cm<sup>-1</sup>, however, the stretching peak corresponds to the C-H functional group because it is less polar than the O-H group. O-H and C-H align with the methyl groups (CH<sub>3</sub>) and silanol (SiOH) due to the presence of lignin, this is according to the previous study reported by Sandouqa *et al.* (2019). Little elevated peaks in both spectra at 1600.3 and 1640 cm<sup>-1</sup>,

show the stretching vibration of an organic component of the RHA's C=O double bond. However, peaks in both patterns between 445 and 1068  $\text{cm}^{-1}$  in the fingerprint region have been connected to the stretching vibrations of carbonate's C-O, suggesting some intriguing components because the peaks are associated with organic components,  $\text{Fe}_2\text{O}_3$ , and CaO. It is important to note that a prominent peak of  $\text{SiO}_2$  at 786.6  $\text{cm}^{-1}$  is particularly noteworthy because it has various benefits, including improved fuel-related properties due to its enhanced surface area and nano additive reactivity performance as well as its ability to avoid leaching (Kapile *et al.*, 2022).

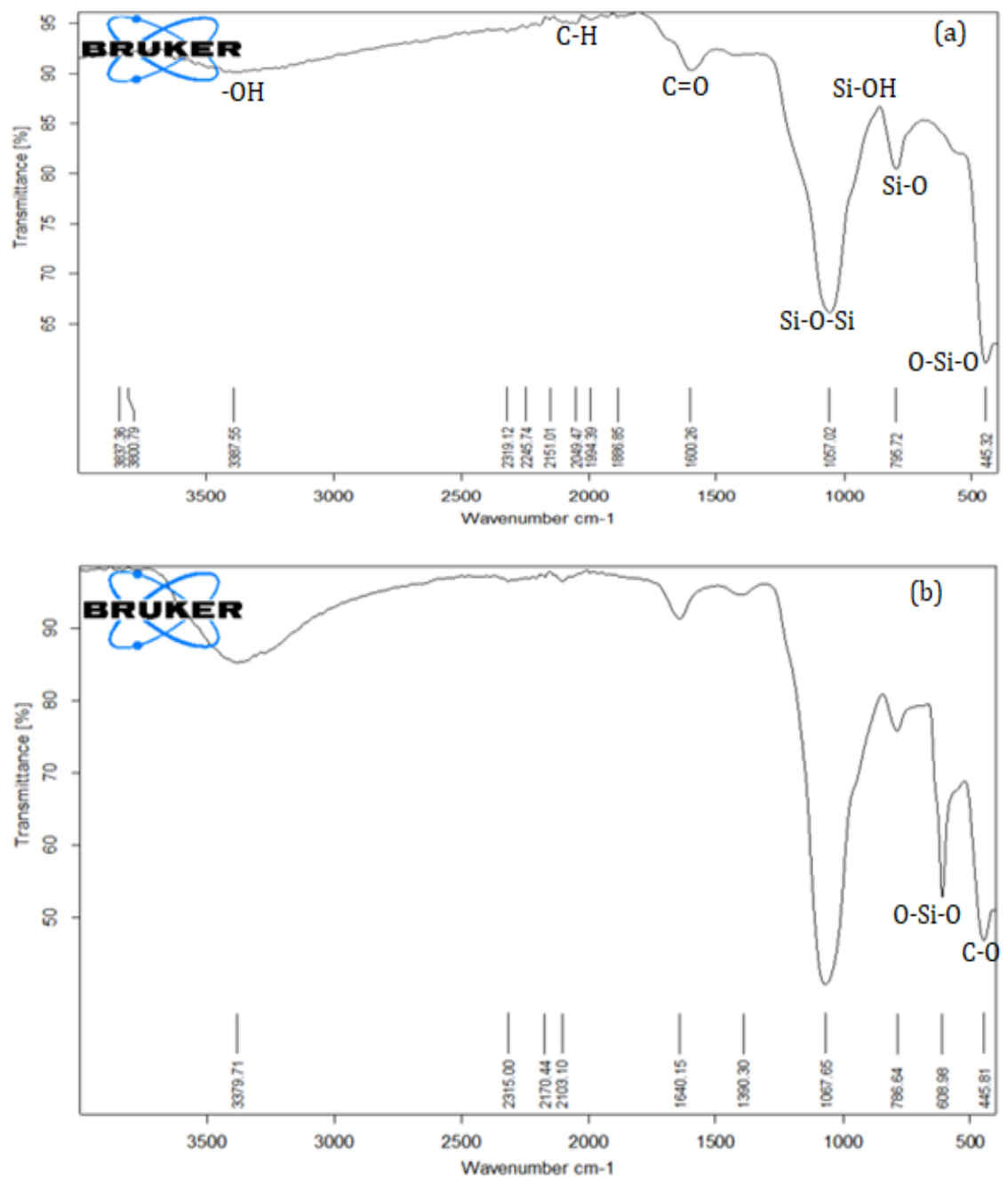


**Figure 17: The FT- IR spectra of (a) RHA and (b) RHS**

#### 4.4.2 Thermal Gravimetric Analysis of RHS

Thermal Gravimetric Analysis (TGA) was used in this investigation to examine the thermal properties of the manufactured nano-additive, as shown in Fig. 18. The calcination process, which occurred at a temperature between 70 and 380°C and caused volatile materials, such as moisture, to escape from the sample, resulted in a large mass loss of 39%. The TGA may also detect the quantity of alkoxy-silane group added to the pure RHA sample and the existence of materials like surfactants that include carbon, oxygen, and hydrogen on the surface of silica (Kapile *et al.*, 2022). The weight loss of RHS was shown to be thermally stable at temperatures beyond 400 to 750°C. This suggests that the sample precursor was likely to undergo full breakdown, with metal oxide emerging as the primary active component of the nanoparticles. The RHS has good thermal stability within this temperature range, as evidenced by the very slight weight loss that has been detected above 400°C. These findings demonstrate that silica can crystallize after 15 h of exposure at temperatures as low as 600, 500, or even 350°C. As a result, silica can remain stable at temperatures above 400°C. In contrast to the other samples, the silica sample that was burned for 12 h at 400°C has the greatest reactivity index value.

This is because, as burning temperatures rise beyond 400°C, amorphous silica transforms into crystalline silica, and only amorphous silica remains soluble after 3 min of extraction. The solubility of crystalline silica increases if the extraction time is prolonged beyond 3 min. If the high-temperature exposure was shorter than 1 min, it is possible to produce highly reactive silica by keeping the combustion temperature below 400°C under oxidizing circumstances for a comparatively long time, up to 680°C. Extended heating above this point may result in the material changing (at least partially) into crystalline silica, first into cristobalite and then into tridymite. This is caused by impurities, which are typically oxides of Ca, K, and Fe (Kapile *et al.*, 2022). If the combustion period of RHA is less than 1 h, SiO<sub>2</sub> may still be in its amorphous state at temperatures between 0 and 900°C. The previous findings reported by Zhang *et al.* (2012) demonstrated that nano-silica showed covalent linking due to the silane-coupling agent being firmly bonded to the particle surface. It loses 4.8% of its weight at temperatures below 200°C, which is caused by physisorbed water and remaining but the starting breakdown temperature of covalently bonded to nano-silica is 300°C which is almost similar in this study.

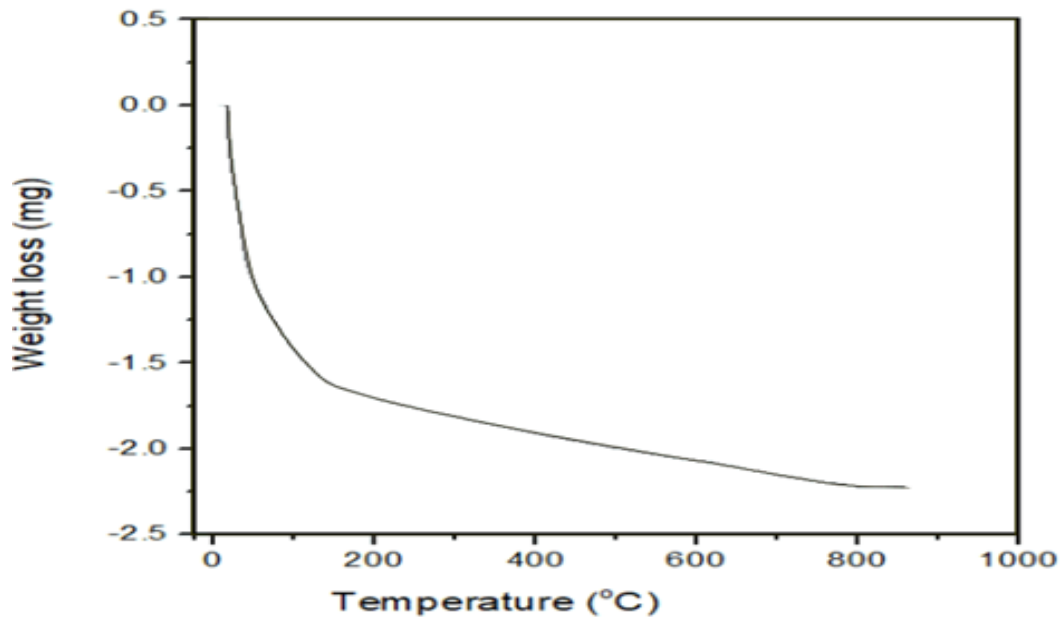


**Figure 18: The RHS thermal decomposition profile between 25 and 800°C**

#### **4.4.3 Surface Pore and Textural Profile Analysis of RHS**

The BJH pore volume, diameter, and BET-specific surface area of synthesized RHS were found to be 0.761 cm<sup>3</sup>/g, 19.3 nm, and 502.24 m<sup>2</sup>/g respectively, and for the RHA were 0.695 cm<sup>3</sup>/g, 30.69 Å, and 665.52 m<sup>2</sup>/g respectively. The surface structure of RHA changed significantly after calcination while still retaining a network of porous structures. The XRD spectra in Fig. 19(a) demonstrate that the amount of impurities had a substantial impact on the sample's pore structure. The average pore size, volume, and surface area increase when certain contaminants are present. In the instance of RHS, capillary pressure-induced shrinkage and cracking of the gel network occurs during calcination at ambient pressure, resulting in extremely low specific area silica. Nevertheless, the amorphous matrix that made up the bulk structure of RHA was still present, but it was dotted with tiny, elongated needles. The earlier research showed that the needles seemed to be thin, flat, elongated fiber fragments with sharp edges and nano-dimension when magnified further (Kapile *et al.*, 2022).

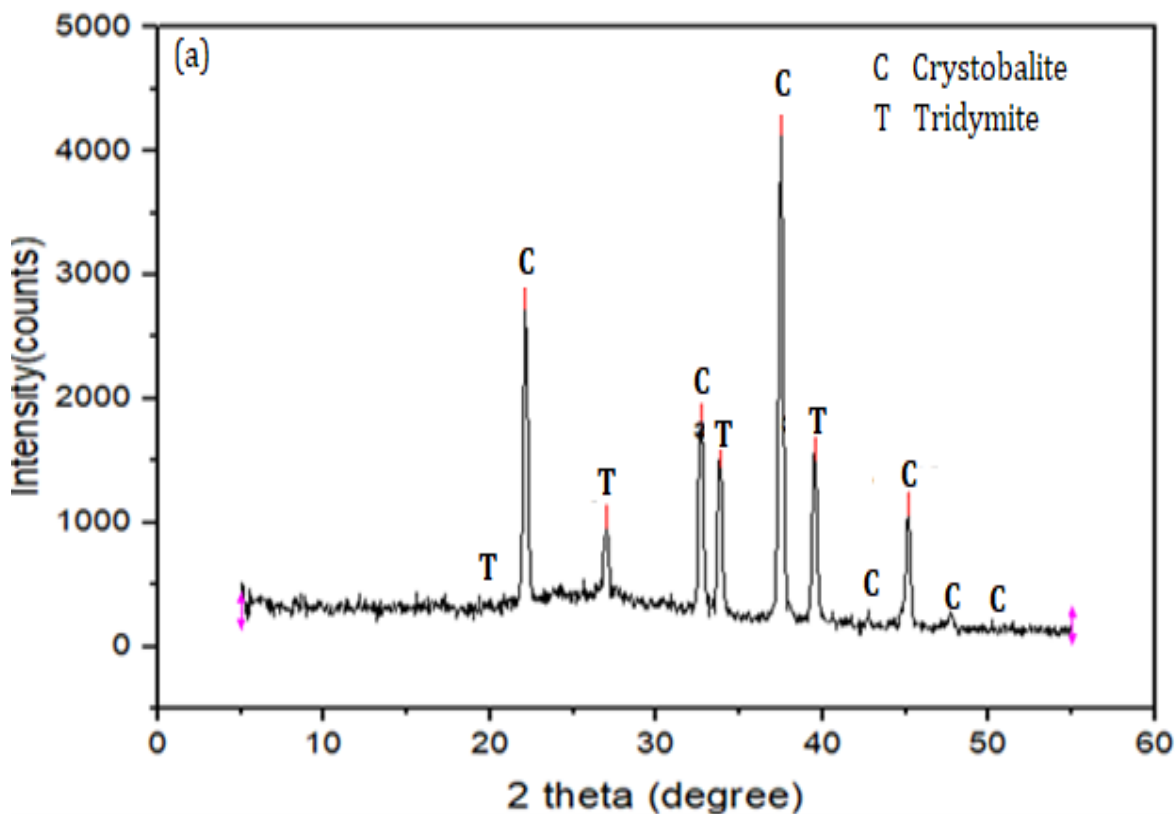
#### **4.4.4 The XRD Spectral Analysis**

As displayed in Fig. 19(a) and (b), the results of the XRD examination showed the existence of quartz, the origin of which may be related to contamination or re-crystallization of silica during calcination. Thus, the RHA, which is plentiful in silica, preserves the amorphous structure of RH at the calcination conditions of 650°C for 2 h, which is consistent with the amorphous nature. However, it's crucial to note how the diffraction peak amplitudes of the



RHS and RHA samples differ from one another. The diffuse peak is moved to a lower  $2\theta$  (Bragg's angle) position in RHS and the peak is thinner than in RHA. This is probably attributed to the Van der Waals forces between neighboring molecules. Cellulose makes up the only component in RH with a crystalline structure presence in levels of around 33%, as previously reported by Blanco *et al.* (2018).

The cellulose's diffraction peaks are at  $2\theta$ , which is equivalent to  $16^\circ$ ,  $22^\circ$ , and  $35^\circ$ , with  $22^\circ$  being the highest intensity peak. These peaks overlap with the amorphous components' background (Blanco *et al.*, 2018; Kapile *et al.*, 2022). When exposed to temperatures above  $650^\circ\text{C}$  for 6 h, the XRD pattern shows partial crystallization; after two hours, it completely changes at  $900^\circ\text{C}$ . The two phases that make up the crystalline state are tridymite and cristobalite. This is because the samples under evaluation have different chemical compositions. Amorphous silica crystallizes more readily at lower temperatures when alkaline elements, like K, are present as impurities (Kapile *et al.*, 2022). However, the XRD pattern for the pure commercial  $\text{SiO}_2$  nanoparticles is shown in Fig. 20, where the only peak is the broadband at about  $22^\circ$ , which is associated with the amorphous nature of silica, these results concur with the previous report by Gavhane *et al.* (2021).



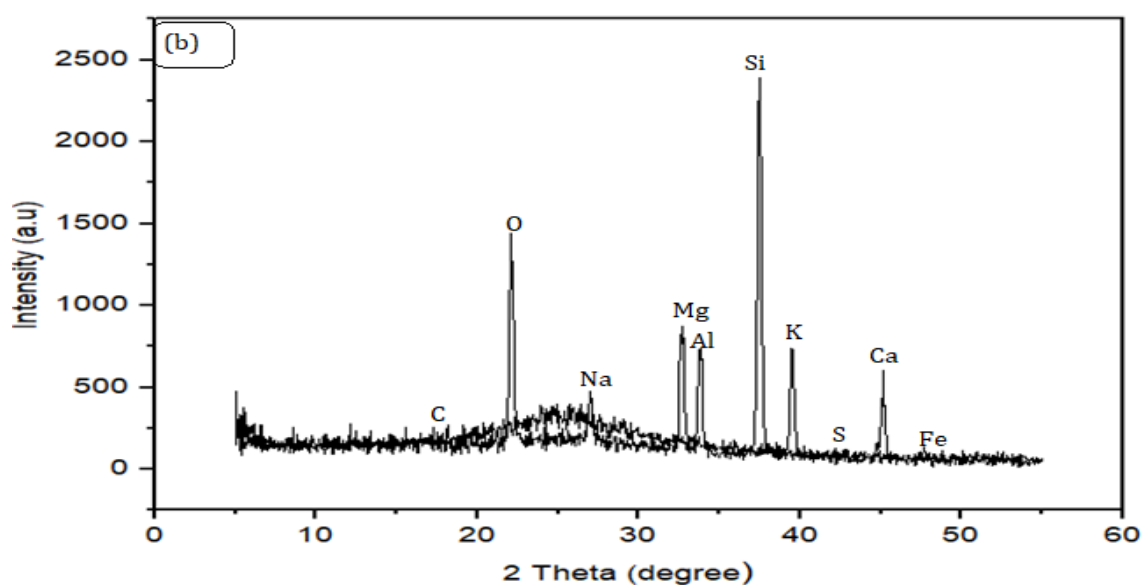


**Figure 19:** The XRD spectra of (a) RHS and (b) RHA

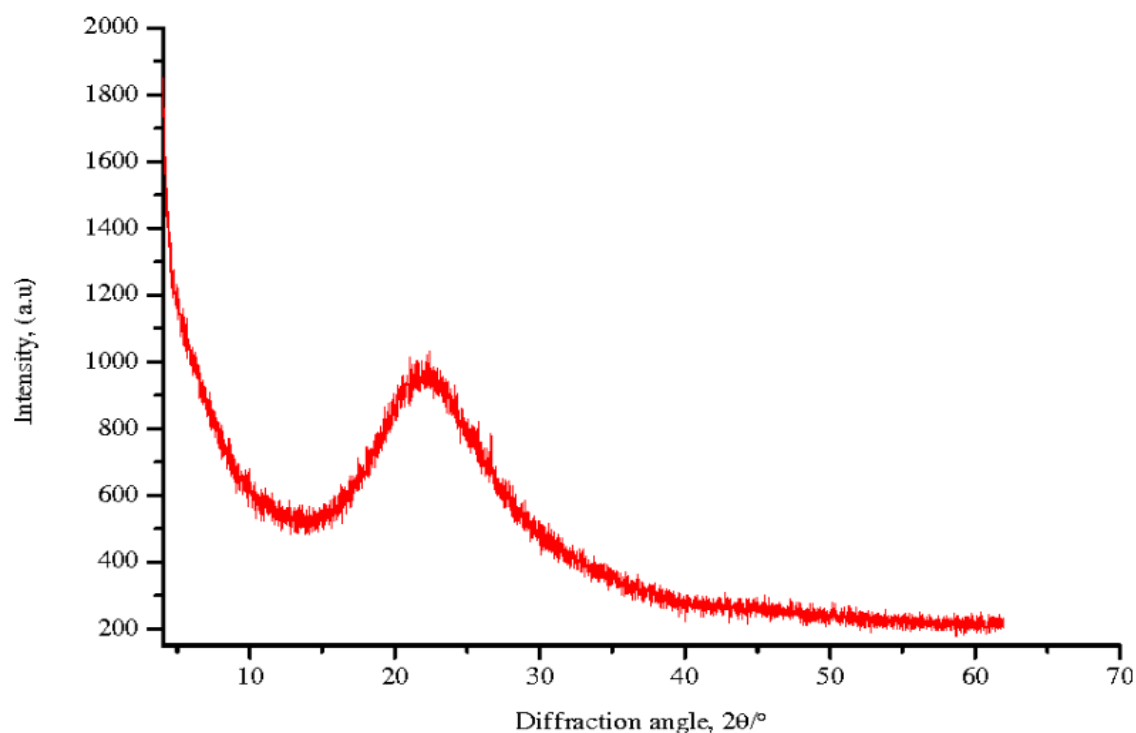


**Figure 20:** The XRD spectrum of pure commercial SiO<sub>2</sub> nanoparticle (Gavhane *et al.*, 2021)

#### 4.4.5 Scanning Electron Microscope

The RHA and RHS, which were produced via supercritical drying and calcined at 650°C are depicted in Fig. 21. Figure 21(a) displays an image of the RHA at a microscopic level. Because there is more carbon and less silica present, the color seems to be blackish. As shown in the XRD spectrum, RHA contains a trace number of impurities including the oxides of K, Fe, S,

Na, Ca, and Mg according to the previous literature. The SEM image of RHS, displayed in Fig. 21(b), reveals a porous structure like a sponge, with the particles' white-colored surface pores which are visible. The results revealed the presence of less sulphur, silicon with traces of Na ions, and oxygen in comparison to RHA, suggesting that the salts were effectively eliminated during the precipitation process. The previous research reported by Wei *et al.* (2021) observed the presence of spherical and amorphous morphology structure of nano-silica with 22.3 nm pore size which is smaller than the diameter of the injector nozzle (0.32 mm).

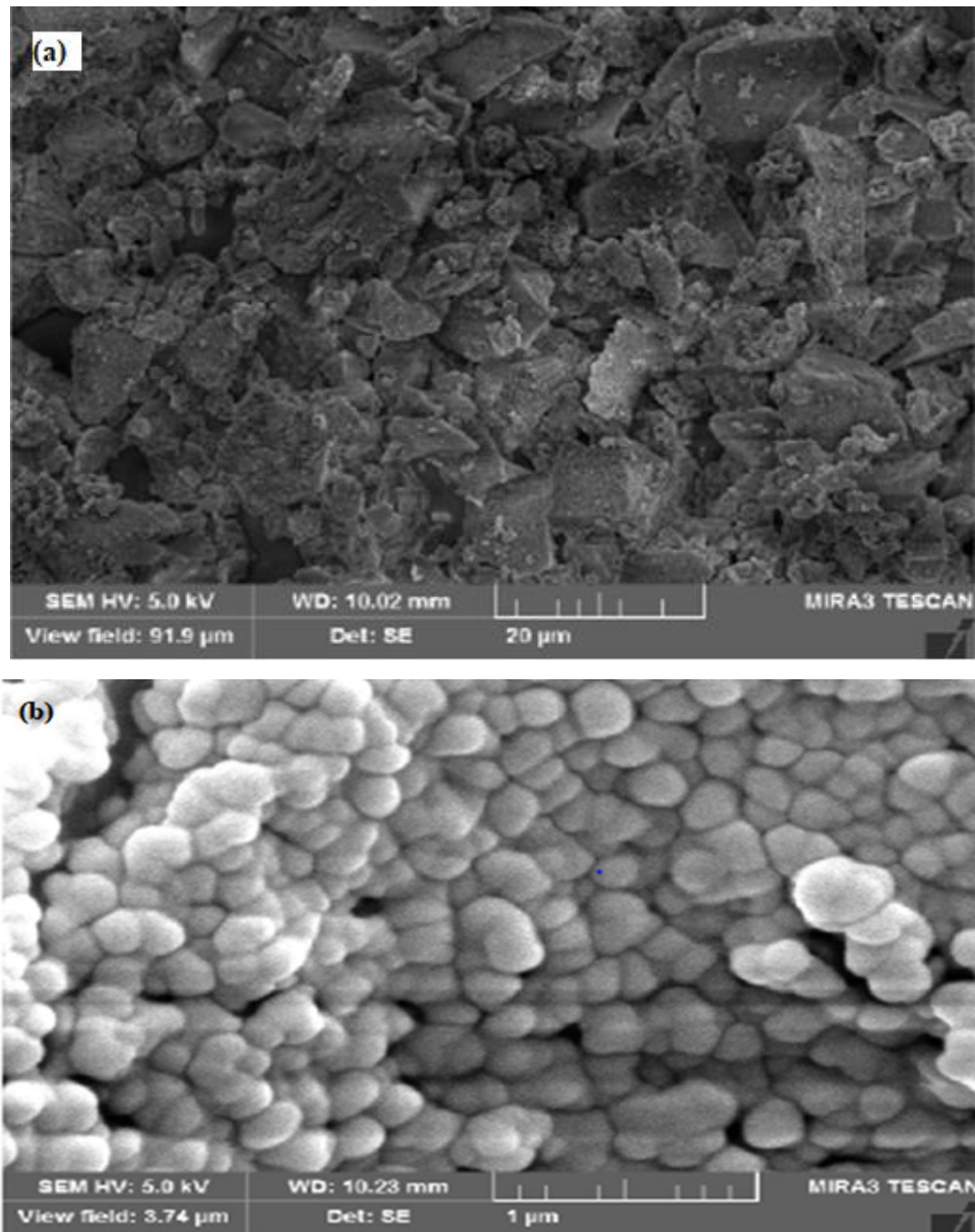


**Figure 21: The SEM images of the (a) RHA and (b) RHS**

#### 4.4.6 The RHA Elemental Composition Profile

The primary constituent of RHA is specified in Table 11. Other than silica,  $\text{Al}_2\text{O}_3$ ,  $\text{K}_2\text{O}$ , and  $\text{CaO}$  make up the majority of the RHA in the proportions of 1.16, 2.80 and 1.93%, respectively. There are trace levels of other contaminants, including unburned carbon, Fe, Na, Mg, and S. The total of these contaminants is 6.11%. The predominant component of RHA is typically 88% silica, which has a strong reactivity and a larger specific surface area-to-volume ratio.

**Table 11: The RHA elemental composition profile**

Elements	Chemical formula	Mass fraction (%)
Alumina	$\text{Al}_2\text{O}_3$	1.16%
Potassium oxide	$\text{K}_2\text{O}$	2.80%
Sodium oxide	$\text{Na}_2\text{O}$	0.56%
Magnesium oxide	$\text{MgO}$	0.45%
Calcium oxide	$\text{CaO}$	1.93%
Silica	$\text{SiO}_2$	88.0%
Ferric oxide	$\text{Fe}_2\text{O}_3$	0.37%
Sulphur trioxide	$\text{SO}_3$	0.135
Loss on Ignition	LOI	4.60%

#### 4.5 Effects of Nano-additive on Fuel Properties of ADME

##### 4.5.1 Oxidation Stability

One of the most crucial characteristics of FAME is oxidation stability, which mainly affects biodiesel during long periods of storage. In general, biodiesel is less oxidation-resistant than petroleum-based fuel, probably due to the high content of unsaturated FFA. Oxidation causes the degradation of the carbon chain which produces compounds that can damage fuel quality and engine efficiency (Hazrat *et al.*, 2021). In the present investigation, the dosage level variation of the nano-silica additive with oxidation stability was determined using pure ADME as the control fuel. Figure 22(a) shows that the oxidation induction period (OIP) increases from 5.2 h at 400 ppm to a maximum of 10.3 h at 800 ppm as the nanoparticle dose level is increased. According to these data, ADME's oxidation stability significantly improved to meet the >3 and >8 h standards set by ASTM D 6751 and EN 14214 respectively. However, the OIP appears to

decrease to 8.1 h at 1000 ppm dose. This is probably due to the increased methyl linolenate content in ADME (29.96%) which is more predominant in autooxidation.

Furthermore, the silicon atom in the silica exhibits tetrahedral coordination, in which a center atom is surrounded by four oxygen atoms.  $\text{SiO}_2$  thus creates three-dimensional network solids where each silicon atom is covalently bound to four oxygen atoms in a tetrahedral pattern. When the nano additive is used at high dosage levels (1000 ppm), its very active hydroxyl (-OH) group gives high oxygen atoms to unsaturated hydrocarbon chains, speeding up the methyl esters' rate of oxidation and increasing their volatility. Biodiesel with low oxidation stability creates challenges in handling during transportation and storage (Hazrat *et al.*, 2021; Kapile *et al.*, 2022).

#### **4.5.2 Kinematic Viscosity**

Figure 22(b) illustrates how the additive's dosage level affects the kinematic viscosity of biodiesel. The fuel's viscosity drops with increasing concentration of nano-additives; at 600 ppm dosing, it drops from 4.62  $\text{mm}^2/\text{s}$  for pure biodiesel to 3.9  $\text{mm}^2/\text{s}$ . Additionally, viscosity increases from 3.9 to 4.5  $\text{mm}^2/\text{s}$  which occurs at the highest dosage of 600 to 1000 ppm. It makes sense that the fuel's additional nanoparticles would raise the fluid layer resistance hence in turn viscosity, which would cause gums and sediments to build up and lead to clogging of the filters (Hazrat *et al.*, 2021). Generally, the higher viscosity fuels often inject into larger droplets, which can lead to poor combustion and more emissions and exhaust smoke. As a result, choosing the nanoparticle dosage level should be predicted to strike a balance between these two opposing effects on the engine's performance and combustion (Hoseini *et al.*, 2020; Kapile *et al.*, 2022).

#### **4.5.3 Flash Point**

The fuel's flash point serves as an indicator of its volatility. This temperature is necessary for a volatile substance to evaporate and turn into an ignitable mixture in the atmosphere. When volatility declines, the flash point rises. Figure 22(c) illustrates the fluctuation of the ADME flash point as a function of dosage and indicates a progressive decrease in fuel volatility as the nano-additive amount is increased. This growth is nearly a straight line. Higher flash point temperatures are ideal for the safe handling and storage of fuel. Because of their higher flash point temperature, fuels enhanced with  $\text{SiO}_2$  nanoparticles are intrinsically safer than base fuels in this scenario (Kapile *et al.*, 2022).

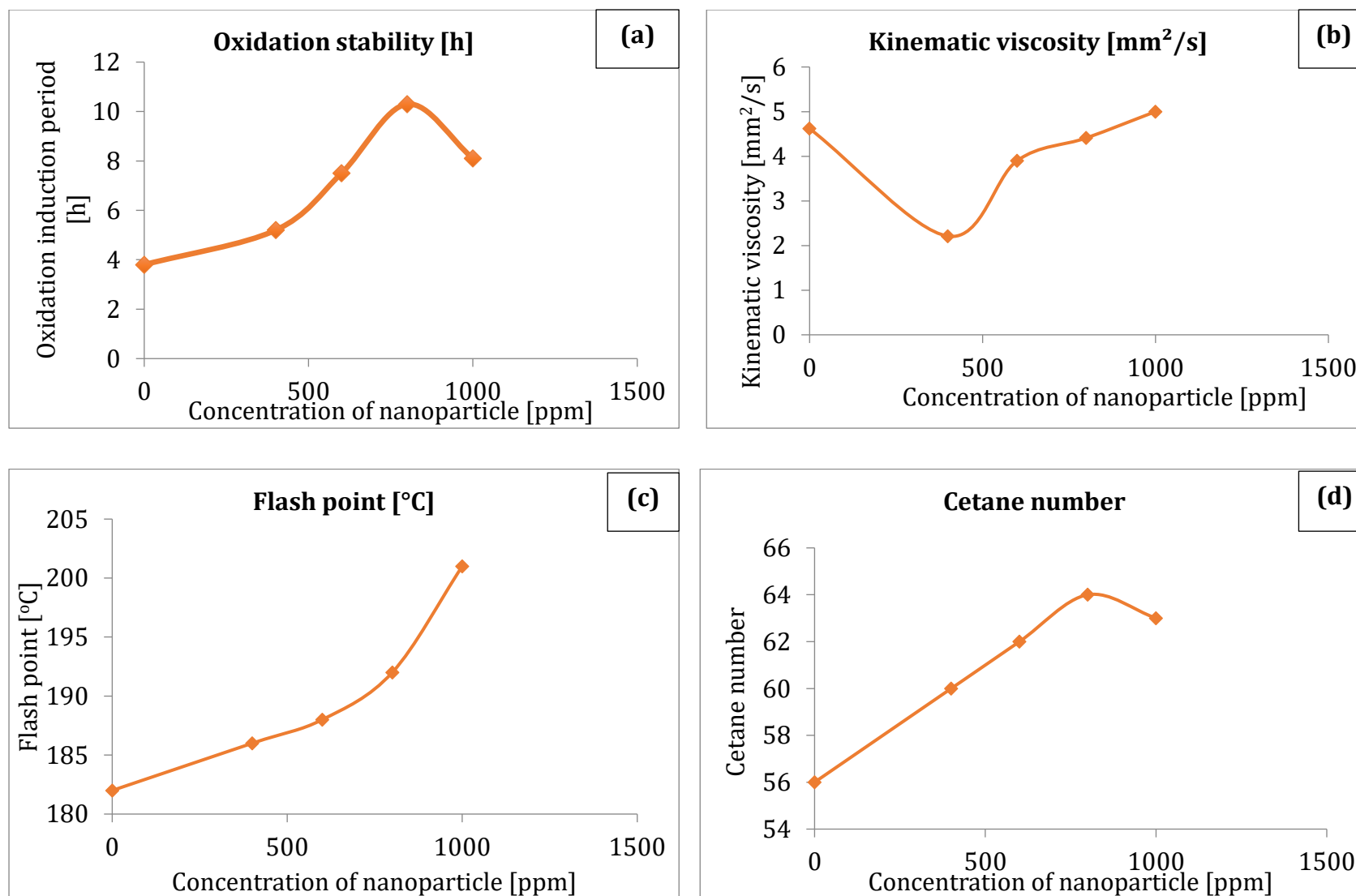


**Figure 22: Influence of nano-SiO<sub>2</sub> additive on (a) oxidation stability (b) kinematic viscosity (c) flash point (d) CN of ADME**

#### 4.5.4 Cetane Number

Cetane number (CN) defined as a measurement of a fuel's ignition quality, affects the engine's ability to produce white smoke and rough combustion. An essential characteristic of a fuel that determines the length of the ID in the combustion chamber is the cetane number. Engine performance is enhanced by fuel of higher CN because it results in a shorter ID period (Erman *et al.*, 2020). Figure 22(d) displays the CN values of ADME for different nanoparticle additive dose levels. The findings showed that at dosage levels of 400 to 800 ppm, CN increases concurrently. As a result, the nanoparticles served as a surfactant (with a slightly larger surface area) and their amorphous nature was successfully emulsified, improving the spray features of ADME. However, beyond 800 ppm CN dropped. This is most likely caused by an increase in the fuel's surface tension, which also raises the fuel's viscosity. Therefore, it is advised that a nanoparticle blending mechanism be used in the improvement of CN (Erman *et al.*, 2020; Kapile *et al.*, 2022).

#### 4.5.5 Cloud and Pour Point

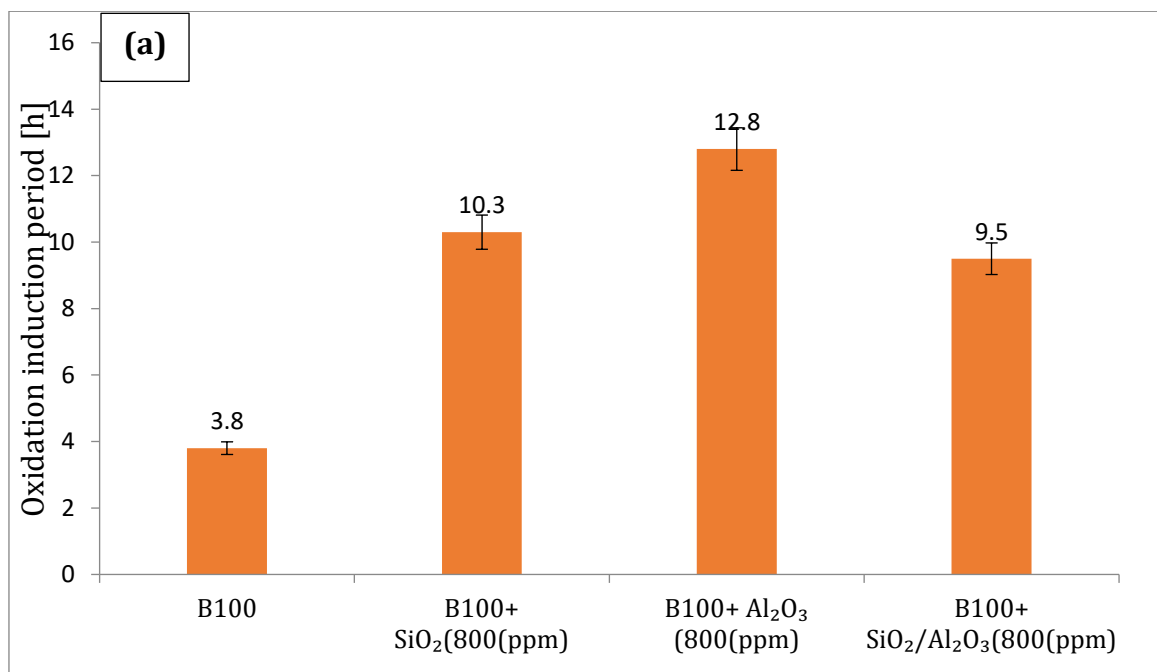
The influence of nano-additives on the pour and cloud point of the ADME and its blends was insignificant. Because of the addition of nanoparticles at various dosage levels to the biodiesel in this situation, no appreciable changes in the pour and cloud points were shown (400, 800, and 1000 ppm). In general, adding silicon oxide nanoparticles to biodiesel has no discernible impact on its cold-temperature properties, so no special handling or storage procedures for the modified fuels are needed in the cold. These findings are consistent with earlier researchers who examined the impact of CeO on biodiesel's cloud and pour points and discovered no appreciable difference between the cloud and pour points for neat and modified biodiesel, which were 6 and -1 °C, respectively at 40 ppm dosing level (Kalaimurugan *et al.*, 2023).

#### 4.5.6 Comparison of Commercial Alumina and Manufactured Silica Nano-additives on Fuel Properties of ADME and its Blends

Synthetic silica and alumina (commercial nano-additives) were doped with ADME to determine its influence on fuel-related properties, the blending was prepared using the ultrasonication process. Results indicated that when pure silica (800 ppm), pure alumina (800 ppm), and blends (400/400 ppm) were used, respectively, there was a small increase in OIP from 10.3 to 12.8 up to 16.4 as displayed in Fig. 23(a), this is due to that alumina is purer than manufactured SiO<sub>2</sub>. Therefore, Al<sub>2</sub>O<sub>3</sub> donates more oxygen atoms to the oxidation reaction,

than nano-SiO<sub>2</sub> additives (Fayad & Dhahad, 2021). Nevertheless, when nano-SiO<sub>2</sub> additives were utilized, the kinematic viscosity of ADME decreased from 4.62 to 2.21 mm<sup>2</sup>/s. This is probably due to the limited tiny particle size (19.3 nm) and low density (2.65 g/cm<sup>3</sup>) of silica in contrast to 20 nm and 3.95 g/cm<sup>3</sup> of alumina.

Therefore, commercial alumina reduced viscosity by 24.2%, from 4.62 to 3.5 mm<sup>2</sup>/s. The kinematic viscosity of ADME increased as the volume fraction of nanoparticles increased, supporting the idea that at higher concentrations, there should be a decrease in the number of collisions between base fuel molecules and nanoparticles because the fuel is more viscous and prevents the nanoparticles from moving freely. These findings concurred with outcomes reported previously by Hazrat *et al.* (2021). The kinematic viscosity rose as the concentration of nanoparticles increased for all SiO<sub>2</sub>/Al<sub>2</sub>O<sub>3</sub> nanoparticle fuel blends as shown in Fig. 23(b). This resulted from the inclusion of blends of nanoparticles, which raised the surface tension in the fuel. As the concentration of nanoparticles increased, led to raised surface tension and therefore the viscosity (Kapile *et al.*, 2022). Furthermore, an increase in CN was noted for ADME doped with SO<sub>2</sub>, Al<sub>2</sub>O<sub>3</sub>, and SO<sub>2</sub>/Al<sub>2</sub>O<sub>3</sub> blend when the concentration of nanoparticles was increased by 14.3, 19.6, and 33.6%, respectively as shown in Fig. 23(c). This is due to the use of nanoparticles greatly boosting the fuel's thermal conductivity. Brownian motion and the high surface area to volume ratio of alumina nanoparticles may be the reason for facilitating collision between the nanoparticles and the base fuel molecules which results in increased thermal interactions between them (Jabbari *et al.*, 2017).





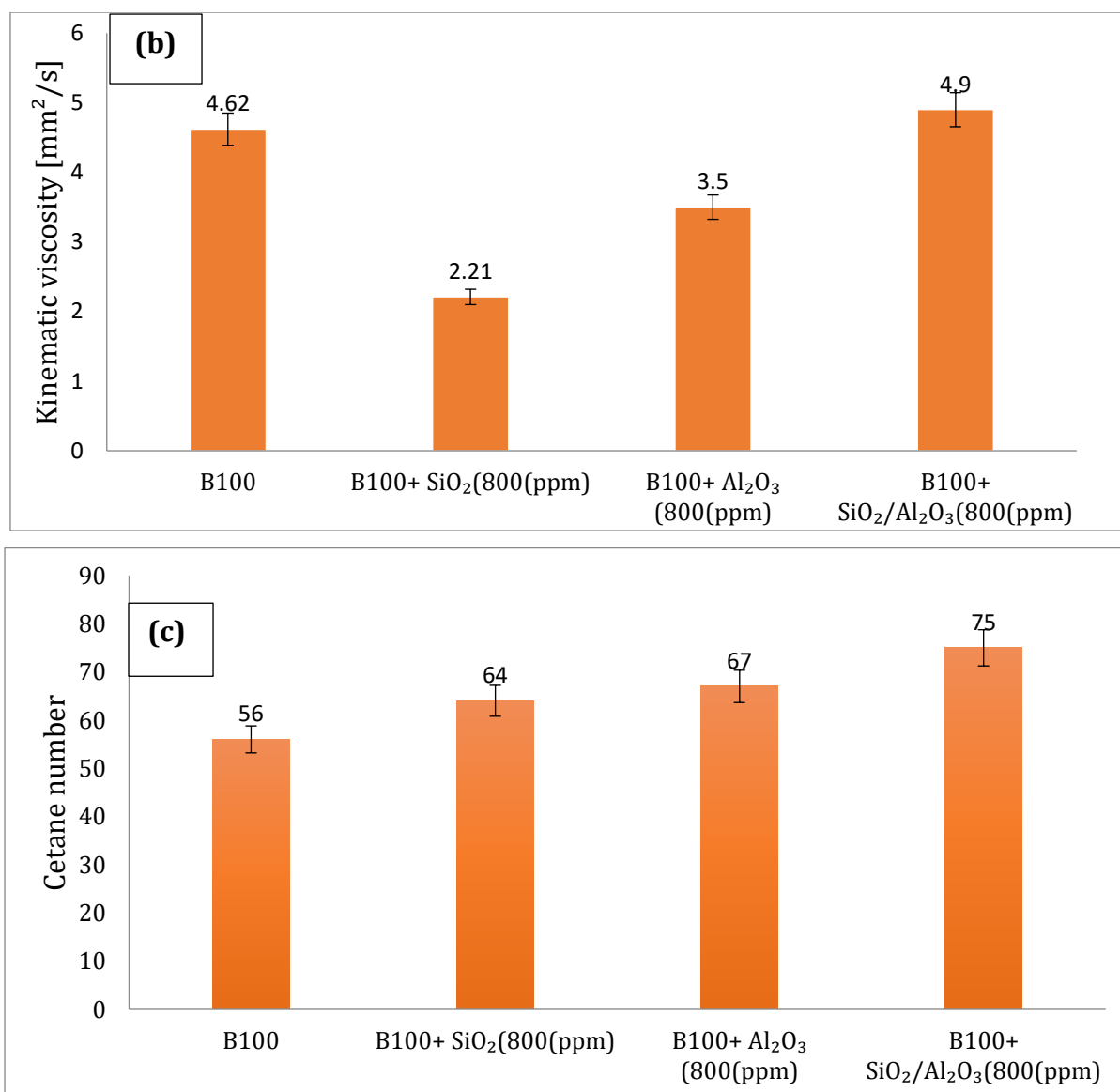


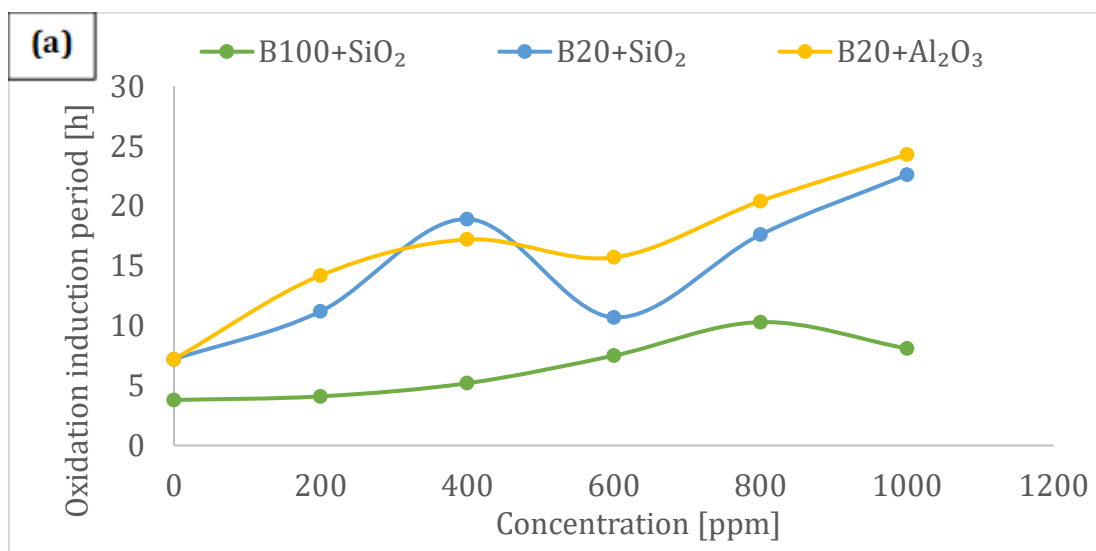
**Figure 23: Effect of commercial and manufactured nano-additives on (a) oxidation stability, (b) kinematic viscosity, and (c) cetane number**

In addition, Fig. 24(a) showed the effect of different dose levels of nano-additives on the oxidation stability of B100 and its blends (B20). The outcome demonstrates that the OIP rises from 3.8 to 10.3 h at dosage levels of 0 to 800 ppm for B100+SiO<sub>2</sub>, but falls at 1000 ppm. However, blending of B20+Al<sub>2</sub>O<sub>3</sub> exhibited the best improvement by 71.7% at 1000 ppm but significantly declined at 600 ppm (15.7 h). The blending of ADME and petroleum diesel (B20+SiO<sub>2</sub>), on the other hand, showed considerable improvement in OIP from 47.2 to 64.16%

at 0 to 1000 ppm respectively. This is because  $\text{Al}_2\text{O}_3$  increases OIP by donating more oxygen atoms from its lattice structure to the fuel blend than  $\text{SiO}_2$ .

Figure 24(b) illustrates how the addition of nanoparticles affects the kinematic viscosity of biodiesel and its blends. An improvement is seen at 400 ppm ( $2.21 \text{ mm}^2/\text{s}$ ) in the result. Blending of B20+ $\text{SiO}_2$  showed minor improvement (a decrease of 32.6%) at 400 ppm, but an increase ( $4.16 \text{ mm}^2/\text{s}$ ) at 600 ppm. At 600 and 1000 ppm dosages, respectively, a higher dosing level of the additive showed an improvement in viscosity from 4.16 to  $4 \text{ mm}^2/\text{s}$  by 3.85%. The improvement in the B20+ $\text{Al}_2\text{O}_3$  blend was shown to drop by 36.9% at 600 ppm. However, at higher dosages (1000 ppm),  $\text{Al}_2\text{O}_3$  showed improvement to  $5.2 \text{ mm}^2/\text{s}$ , while  $\text{SiO}_2$  dosage was reduced to  $4 \text{ mm}^2/\text{s}$ . This is evident as a result of the fuel blend's non-homogeneous  $\text{Al}_2\text{O}_3$  mixing.  $\text{Al}_2\text{O}_3$  caused more kinematic viscosity than  $\text{SiO}_2$  when added at greater dosage levels. This is due to that  $\text{Al}_2\text{O}_3$  fuel blends have a larger density ( $3.7 \text{ g/cm}^3$ ) than the  $\text{SiO}_2$  blends ( $2.65 \text{ g/cm}^3$ ).

Furthermore, the addition of nanoparticles raises the fuel blends' surface tension, therefore raising surface tension would likewise raise viscosity (Mei *et al.*, 2021). The previous study conducted by Sajith *et al.* (2010) used CeO additives in biodiesel at the dosing levels of 20, 40, and 80 ppm. The results showed a decrease in fuel viscosity upon the addition of nanoadditives which in turn increased flash and fire point. Generally, since ADME has a higher degree of unsaturation than fossil fuel diesel by a factor of two, blending B20 with nanoparticles improves the stability of biodiesel over B100 with nanoparticles. This increases dispensability in contact with the fuel, which in turn enhances oxidation stability and kinematic viscosity according to the research reported by Gad & Jayaraj (2020).



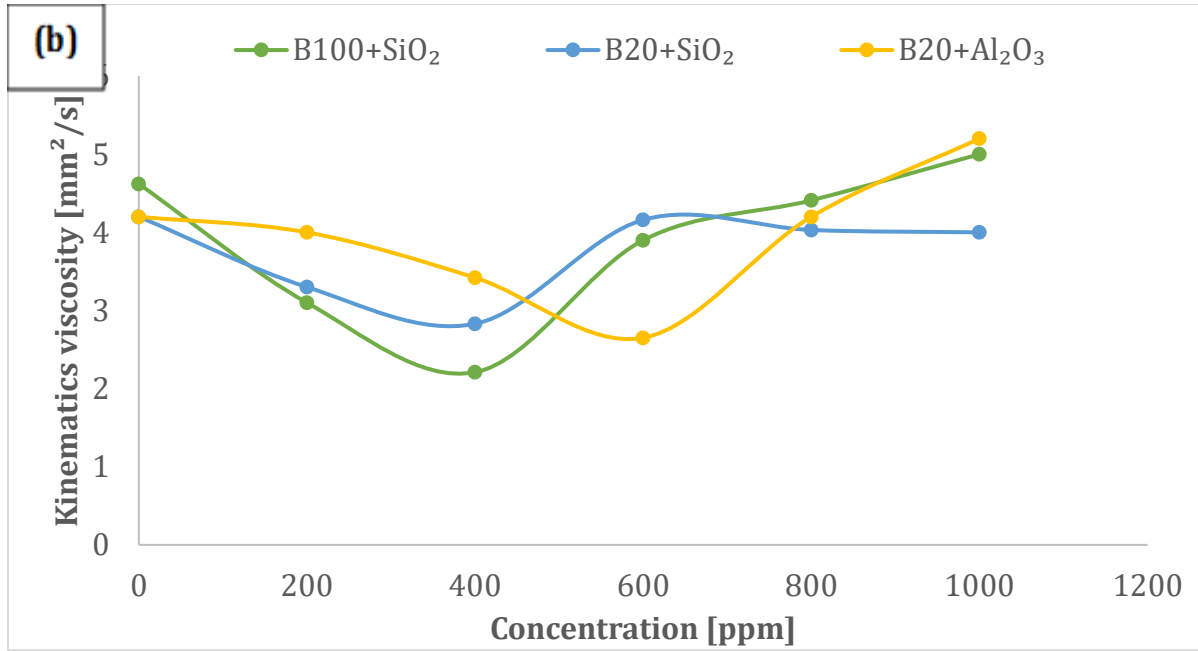


**Figure 24: Effect of commercial and manufactured nano-additives on (a) Oxidation stability (b) Kinematic viscosity of B100 and B20**

#### 4.6 Engine Performance Analysis

##### 4.6.1 Brake Thermal Efficiency (BTE)

The influence of SiO<sub>2</sub> on the BTE at different BP is depicted in Fig. 25. The measurements were taken for several biodiesel blends using nano-additive in varied combinations. BTE was observed to rise to up to 16 kW brake power in every combination and then either stabilize or diminish after that. At medium brake power (12 kW), B20+SiO<sub>2</sub> recorded slightly higher BTE by 0.28% and 0.84% compared to B100 and B100+SiO<sub>2</sub> respectively, this is probably due to nanoparticles showed higher heat transfer rate, rapid oxidation, shorter ID, increased reactivity, and improved catalytic effect due to their increased surface area to volume ratio which in turn improved the combustion efficiency (Wei *et al.*, 2021). However, the BTE reduction is considerable due to biodiesel's lower calorific value caused by its fuel-bound oxygen and greater density. The mean value of BTE at maximum BP (20 kW) for B20, B20+SiO<sub>2</sub>, B100, and B100+SiO<sub>2</sub> fuels were 29.9, 28.2, 28.44, and 27.1% respectively. This revealed that B20+SiO<sub>2</sub> was slightly reduced by 1.76% compared to B20 and B100+SiO<sub>2</sub> increased by 0.24% compared to B20+SiO<sub>2</sub>, also B100+SiO<sub>2</sub> reduced by 1.34% compared to neat B100.

In general, it was shown that the engine efficiency using B100 blends is lower compared to that of conventional B0 which is due to its higher viscosity than B0 fuel. While increasing loads

on the engine, the BP of the engine and mass flow rate of fuel increase due to self-governance which maintains the engine rpm constant. The heat loss will be reduced and all these factors together will increase the BTE of the engine. However, the proportion at which BP increases with load is greater than the proportion of the increase in mass flow rate of the fuel and there is a minor decrease in BTE in the case of the B100 at all the BP (Gad *et al.*, 2018). These results concurred with a previous study reported by Gavhane *et al.* (2021) in which BTE was higher when SiO<sub>2</sub> was added to neat soybean biodiesel than that of untreated biodiesel.

#### 4.6.2 Brake Specific Fuel Consumption

The brake specific fuel consumption (BSFC) is the ratio of fuel consumed per hour to produce a kW of power. Figure 26 depicts the variation of BSFC with different engine BP. At all BPs, the B100 blend had the highest BSFC of any nano-fuel combination, while the B0 fuel had the lowest BSFC. When compared to B100, however, adding 400 ppm of nano-SiO<sub>2</sub> additive leads to a lower BSFC. The cylinder temperature rises as the engine load increases, shortening the ID period and lowering the BSFC (Aldhaidhawi *et al.*, 2017). SiO<sub>2</sub> nano-additives operate as catalysts during combustion because of their greater reactive surface area (Gavhane *et al.*, 2021). When a droplet is injected into the combustion chamber, leads to improved combustion, resulting in a lowering BSFC as compared to B100. Therefore, BSFC for B20, B20+SiO<sub>2</sub>, B100, and B100+SiO<sub>2</sub> was reduced by 78.9, 78.2, 79.6 and 79.3%, respectively from minimum to maximum BP. These results concurred with the previous studies recorded by Hoseini *et al.* (2020) and Gavhane *et al.* (2021). In general, B0 consumed the lowest BSFC as compared to neat B100. The higher BSFC of B100 was due to its lower calorific value, which produced lower HRR and CGP during combustion as compared to B0.

In addition, the higher viscosity of B100 leads to reduced atomization of B20 and thus facilitates incomplete combustion and hence produces less energy. When nanoparticle fuel blends were utilized, there was an improvement in combustion efficiency for all BP applied, and hence the fuel consumption was reduced as compared to un-doped nanoparticle fuel blends, this provides similar trends to the study reported by Gavhane *et al.* (2021) in which lower BSFC resulted for SiO<sub>2</sub> added to soya bean biodiesel blends (B25) as compared to neat B25. Therefore, about 9.88 and 5.81% reduction of BSFC for B25 at a dosage level of 50 and 75 ppm were observed compared to B25 respectively.

### 4.6.3 Exhaust Gas Temperature

Figure 27 depicts how nanoparticles affected the exhaust gas temperature (EGT) of tested fuel samples at different applied BP. The EGT rose with engine BP for all test fuels, this is probably due to more fuel being required to provide the same amount of power, the quantity of heat inside the cylinder, and the amount of heat carried by exhaust gases increased, causing the EGT to rise. At the low BP, B20 and B100+SiO<sub>2</sub> recorded a high EGT of about 168°C compared to all other fuel blends. However, at maximum BP, B100 and B100+SiO<sub>2</sub> reported the highest EGT at about 485 and 480°C respectively therefore, showed an increase by 7.77% and 6.67% as compared to B20. Fuel samples of B0 and B20+SiO<sub>2</sub> showed a similar increase by 4.44%. The B20+SiO<sub>2</sub> fuel blend shows an improved increase for all BPs compared to all other blends and the neat B0. The further reduction in EGT with the B20 and B0 blend was most likely brought during the expansion stroke by the early completion of combustion. The SiO<sub>2</sub> nanoparticles are generally added to biodiesel to improve the combustion process since it raises the fuel blend's oxygen content and, consequently, the peak pressure (Najafi, 2018). For this study, the SiO<sub>2</sub> nanoparticle additive had a slight influence on the EGT.

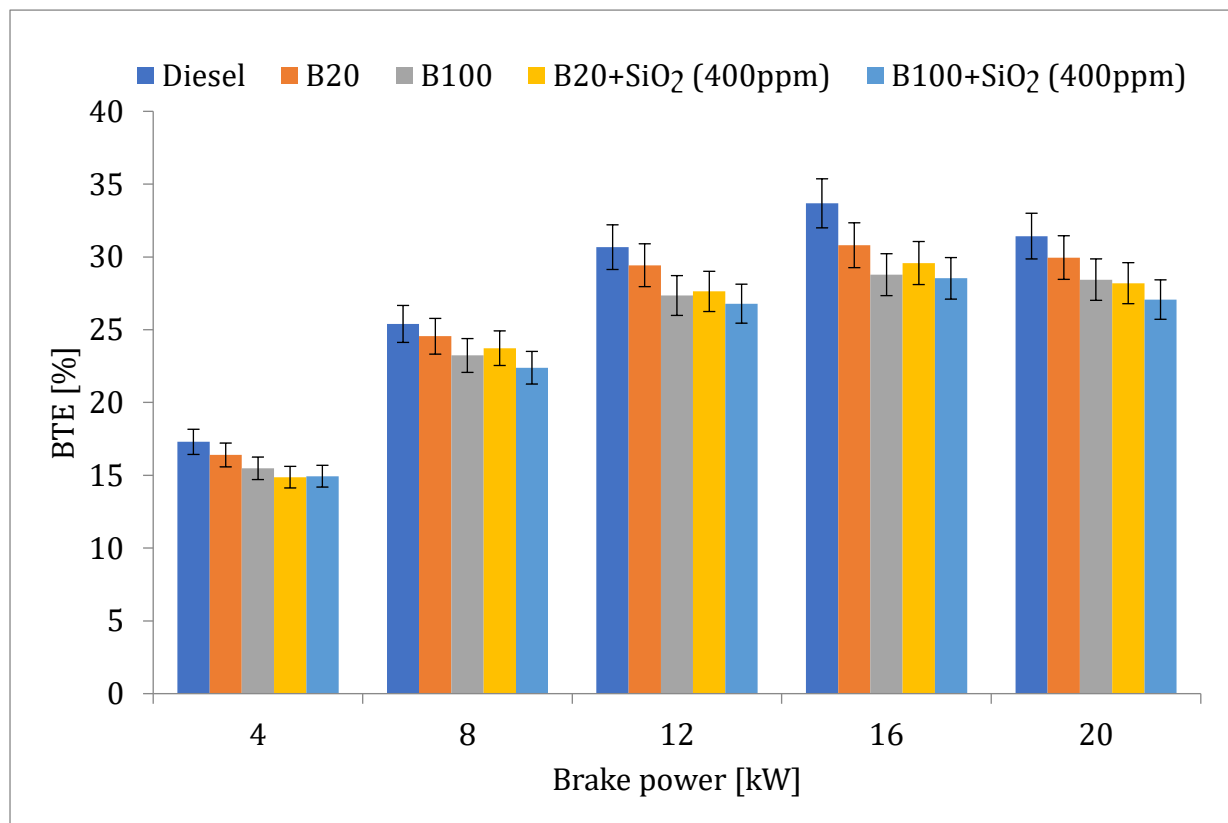
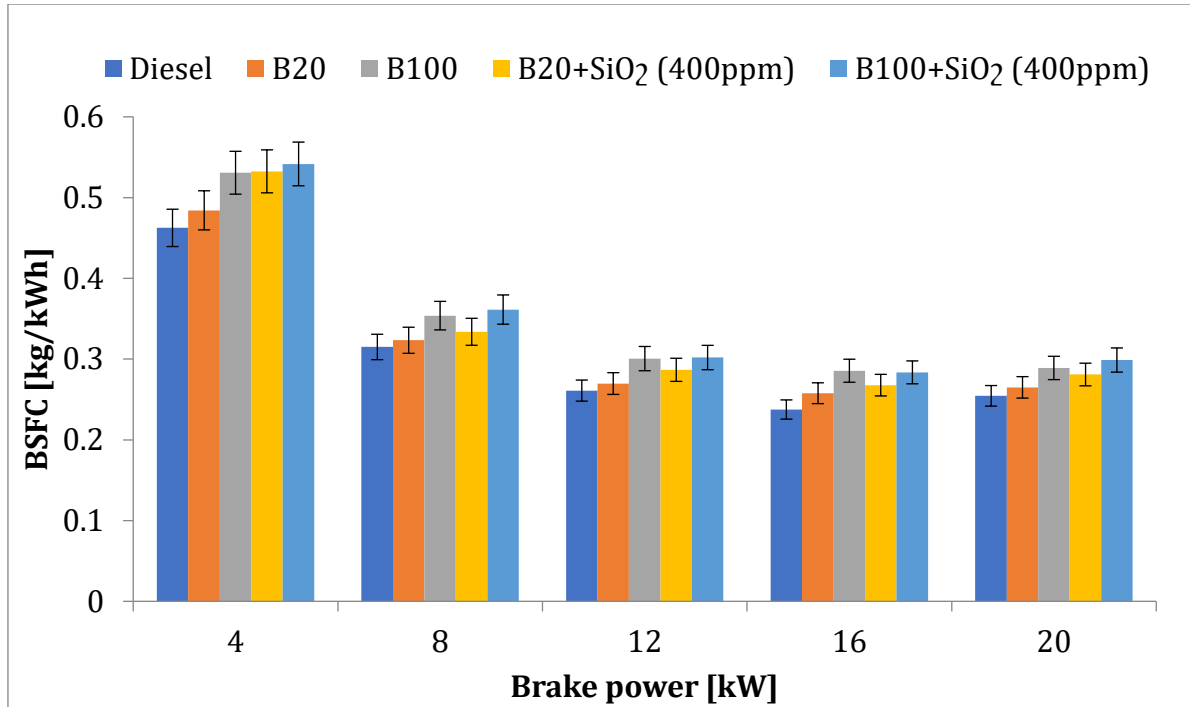
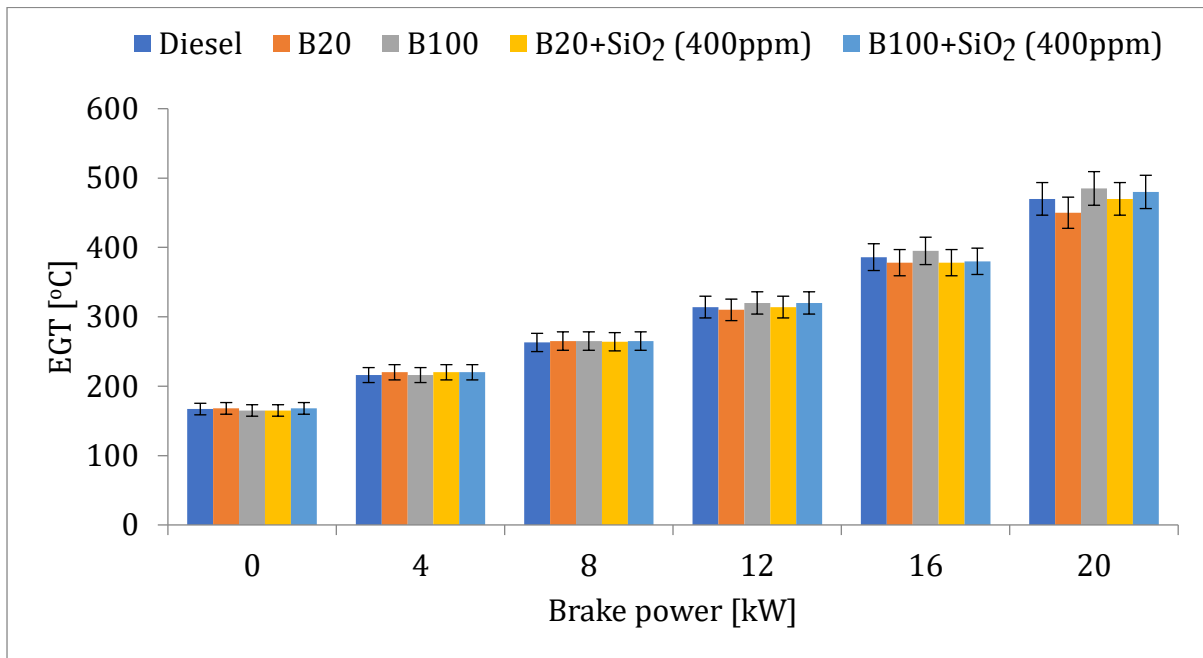


Figure 25: Brake thermal efficiency (BTE) as a function of brake power



**Figure 26: Brake specific fuel consumption (BSFC) as a function of brake power**



**Figure 27: Exhaust gas temperature (EGT) as a function of brake power**

## 4.7 Engine Combustion Analysis

### 4.7.1 In-cylinder Gas Pressure

In-cylinder pressure profiles for the five tested fuels at medium (12 kW) and maximum (20 kW) BP are displayed in Fig. 28. The diesel engine produces a similar In-cylinder gas pressure

(CGP) pattern for all tested fuels. It was observed that there was no significant difference in peak cylinder pressure at low BP conditions among all five fuel samples tested. At medium BP, B0, and B100+SiO<sub>2</sub> recorded higher CGP of about 67.1 and 67.04 bar respectively, in comparison with B20+SiO<sub>2</sub>, B20, and B100 which noticed CGP of about 65.9, 66.8 and 66.9 bar respectively. The typical order for the increase of CGP is B20+SiO<sub>2</sub><B20<B100<B100+SiO<sub>2</sub><B0. At maximum BP condition (20 kW), it was observed that the maximum peak cylinder pressure was established to be 82.1 bar with B100 by 1.56% compared to B100+SiO<sub>2</sub>. Also, B20 recorded a slightly lower peak cylinder pressure which was 80.67 bar. B20+SiO<sub>2</sub> was noticed slightly higher by 0.06% compared to B20 and B0 recorded a lower CGP of about 81.54 bar than B100 which was 82.06 bar. In general, the cylinder pressure was not significantly affected by the addition of SiO<sub>2</sub> nanoparticles to biodiesel. Additionally, in a CI engine, the amount of fuel participating in the uncontrolled combustion phase, which is controlled by the delay period, affects the peak pressure, which in turn depends on the combustion rate in the early stages. The formation of the fuel mixture during the delay time has an impact as well. Higher peak pressures for biodiesel fuels than with diesel fuel are caused by longer ID (Sathish & Singaravelu, 2020). This is due to the viscosity of diesel being lower than that of ADME, the ID of diesel is shortened and results in uniform combustion and lower peak cylinder pressure. The other reason for the lower peak pressure for B0 is due to its higher calorific value. Fuel with a higher calorific value requires a lesser quantity of fuel during combustion (Devarajan *et al.*, 2018; Ooi *et al.*, 2018).

It is observed that adding 400 ppm of SiO<sub>2</sub> nanoparticles to ADME observed a likely considerable slightly increase in the peak CGP compared to the B20 fuel blend than neat B100. The thermal conductivity of the fuel blend is improved with the addition of nanoparticles. As a result of higher thermal conductivity, the combustion is initiated early, causing a higher peak pressure. This is due to the improved ignition quality and higher thermal conductivity of SiO<sub>2</sub> nanoparticles (Goyal *et al.*, 2019). These results match with the previous study reported by Kumar and Tomar, (2019) that reported a similar pressure variation of the diesel engine fueled with the nano-fuel blends.

#### **4.7.2 Heat Release Rate**

Heat release analysis provides valuable information about the fuel injection system, fuel type, effect of engine design, and engine operating conditions on the engine performance and combustion process. In the heat release rate (HRR) profile shown in Fig. 29, it was observed

that the peak HRR value of B100 corresponding to peak pressure is lower than that of B0. This is probably due to the higher CN of biodiesel (56) than diesel fuel. Generally, heat release occurs in a variety of stages. The first stage, referred to as premixed combustion, lasts from the moment of ignition until the HRR starts to fall. This is because the fuel-air mixture that was created during the ID phase ignited (Pham *et al.*, 2021). The diffusion combustion phase is the second stage. As is common for naturally aspirated engines, this investigation found that B0 fuel exhibited quick premixed burning followed by diffusion combustion. Consequently, using low-viscosity, highly volatile diesel led to a greater build-up of fuel over the comparatively longer delay period, which raised the HRR (Emiroğlu & Şen, 2018).

In addition, physical properties such as kinematic viscosity and density are less favorable to initiate instantaneous combustion despite enough ID available. There are chances of power being wasted due to slower combustion. At the medium BP, the maximum value of HRR of B20+SiO<sub>2</sub>, B20, B100, B100+SiO<sub>2</sub>, and B0 fuel blends were 105.12, 109.22, 102.34, 105.45, and 115.75 J/°CA respectively. The peak HRR values of the nano-fuel mixture are slightly greater than untreated biodiesel. This can be accredited to the penetration of fuel droplets, uniform air-fuel mixture, high volatility, improved fuel jet momentum reduced ID, and high surface area-to-volume ratio of the SiO nanoparticles. Similar outcomes were proposed by Praveena *et al.* (2020) while doping CuO nanoparticle additive at concentration levels of 50 and 100 ppm to pongamia methyl ester. At maximum BP (20 kW), the peak HRR was recorded to be 161.32, 147.74, 129.62, 124.7, and 119.45 J/°CA for B0, B20, B20+SiO<sub>2</sub>, B100, and B100+SiO<sub>2</sub> tested fuels respectively. The results of this experimental investigation showed that the overall combustion properties of mineral diesel and biodiesel were quite similar and that the 400 ppm addition of SiO<sub>2</sub> nanoparticles to the biodiesel had no discernible impact on these characteristics.

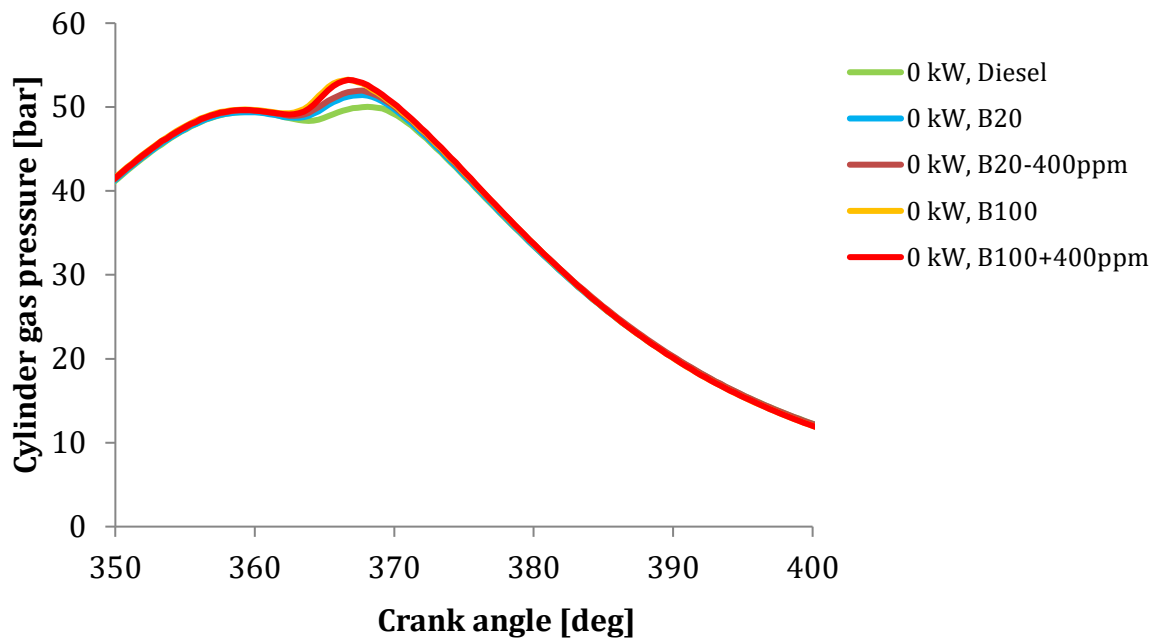
#### **4.7.3 The Mass Rate of Fuel Burnt**

The variation of the mass rate of fuel burnt with the BP for all fuel samples is shown in Fig. 30. The mass fraction of fuel burnt for all the biodiesel blended fuels was slightly higher compared to that of diesel fuel. This implies that the combustion starts earlier for biodiesel blends for all engine BP conditions and it is more prominent with an increase in the quantity of the biodiesel and its blends consumed (Bibin *et al.*, 2022). At low BP, B100 and B100+SiO<sub>2</sub> observed a slightly higher mass rate of fuel consumed about 1.42 and 1.44 kg/h than all other fuel samples. This clearly showed that the amount of fuel that had to burn increased with engine

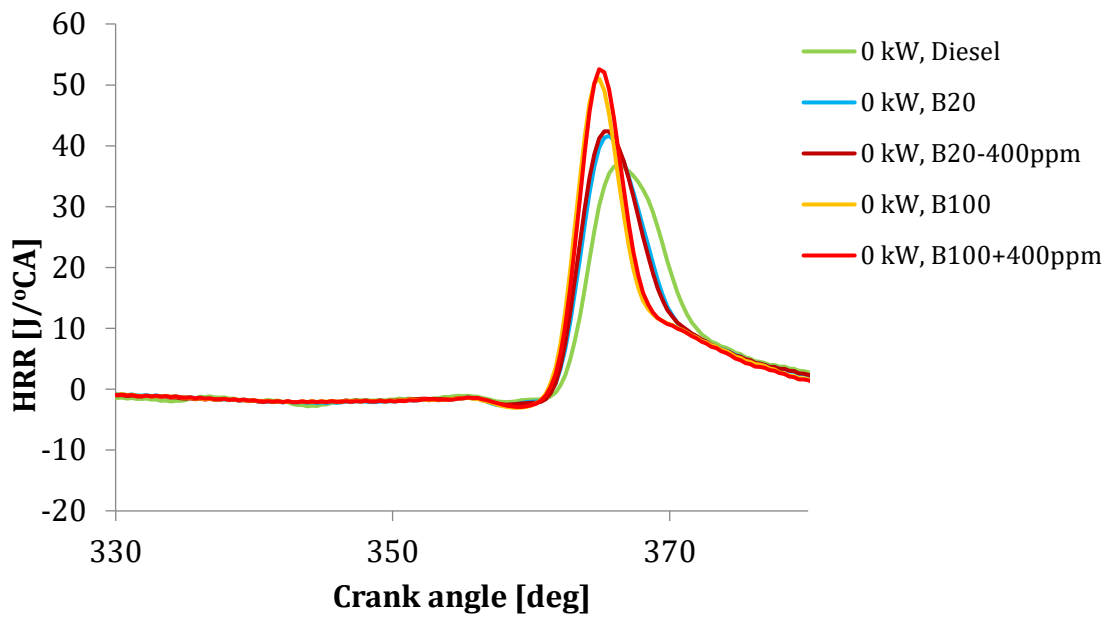


BP because more fuel injection implies that the combustion process would take a longer time to complete.

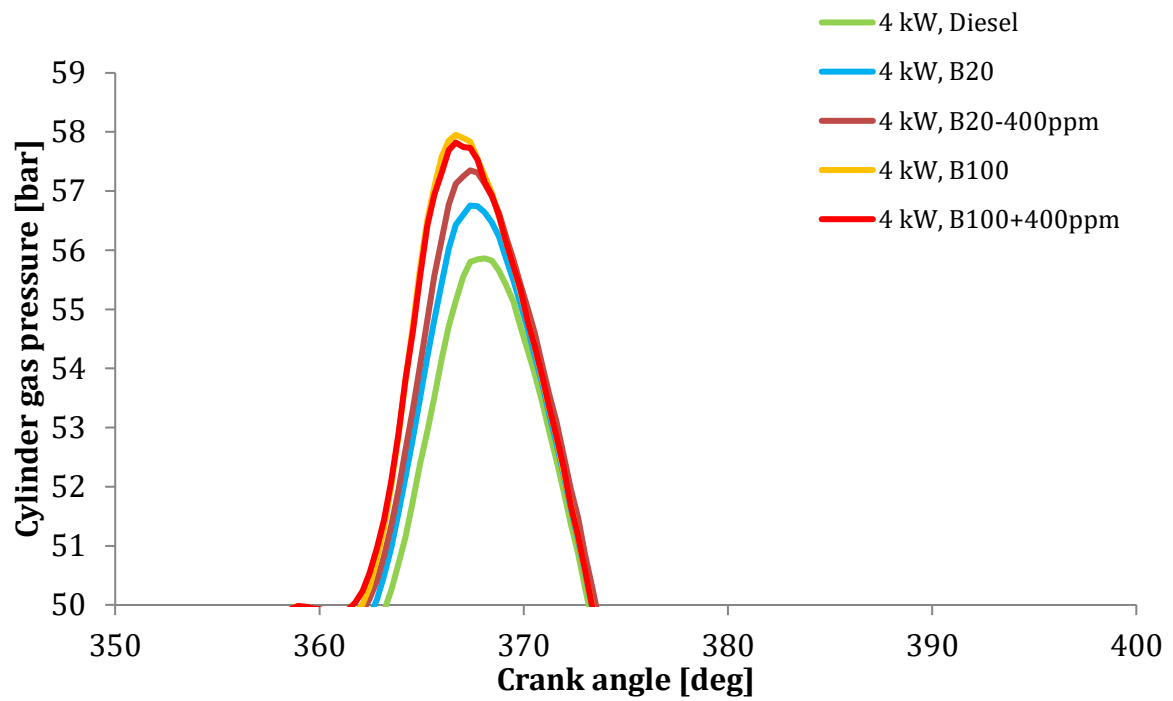
At medium (12 kW) and maximum (20 kW) BP, similar trends were recorded in which B100, B20+SiO<sub>2</sub>, and B100+SiO<sub>2</sub> showed a higher mass of fuel consumed compared to all other fuel samples. However, the addition of SiO<sub>2</sub> nanoparticles enhances faster combustion, which is associated with the catalytic and thermal conductive nature of nanoparticles. This can be observed for maximum BP, B100+SiO<sub>2</sub> nano-fuel blend had advanced in the mass rate of fuel burnt by 3.5% compared to B100 and B20+SiO<sub>2</sub> increased by 6% compared to B20. Also, B100 experiences the point of retarded phase as a result of more injected fuel associated with its lower calorific value and late start of combustion as compared to diesel. This implies that the B100 burnt was earlier compared to B0 possibly due to improved air-fuel mixing and fuel reactivity. Fast combustion is due to high cylinder temperature and oxygen availability. Dhar *et al.* (2012) also reported similar kind of results with nanoparticles added to biodiesel blends.



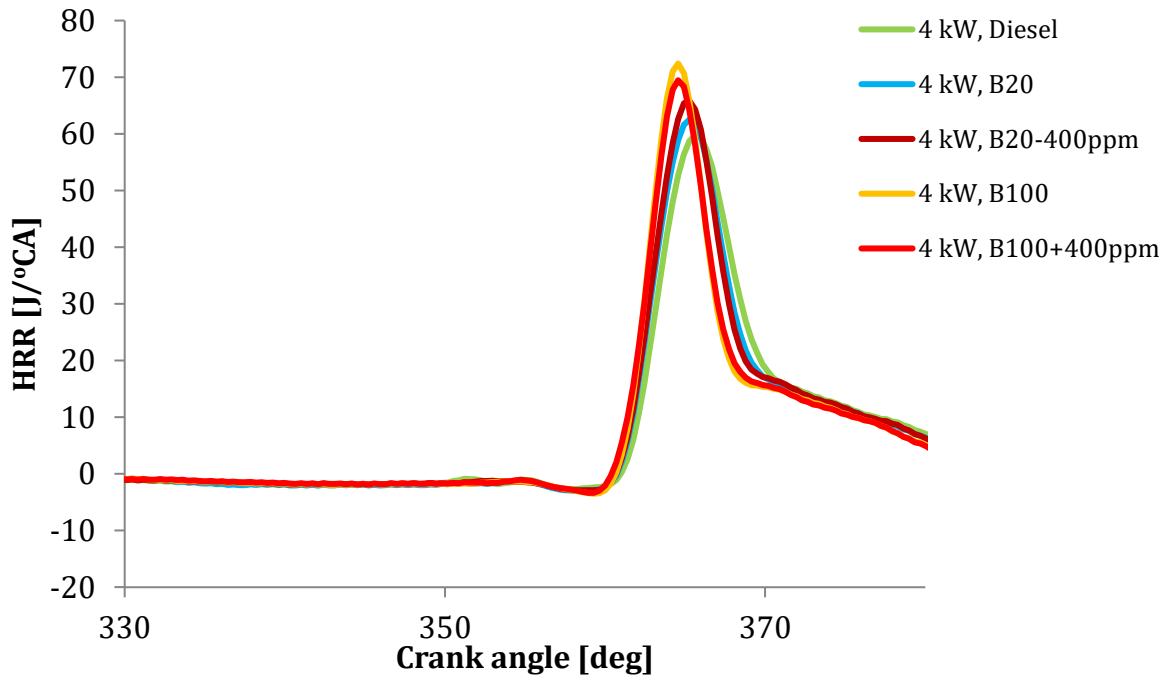
(a)



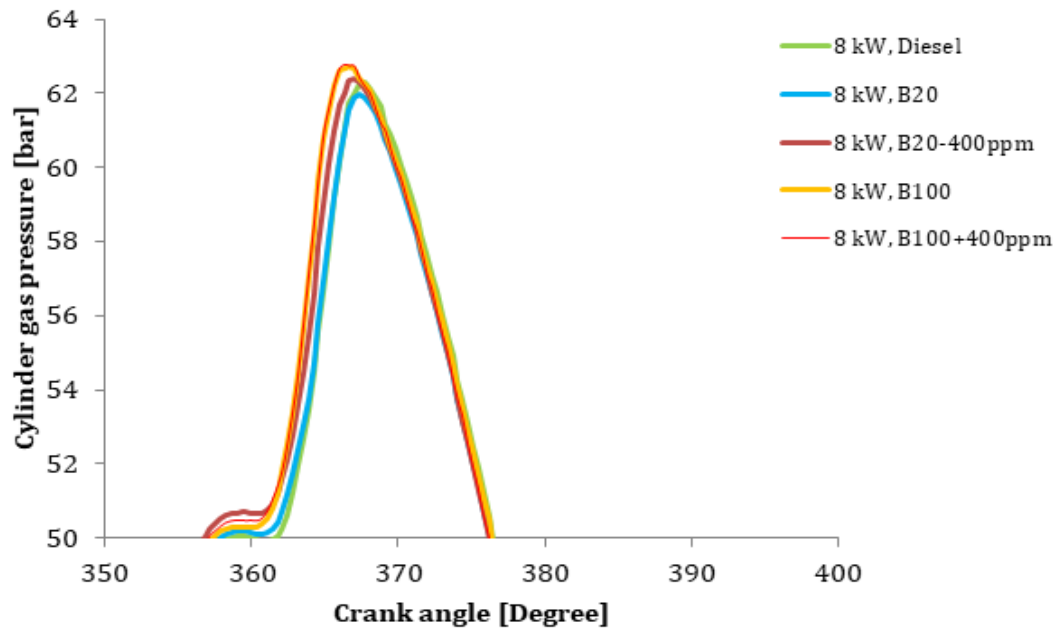
(b)



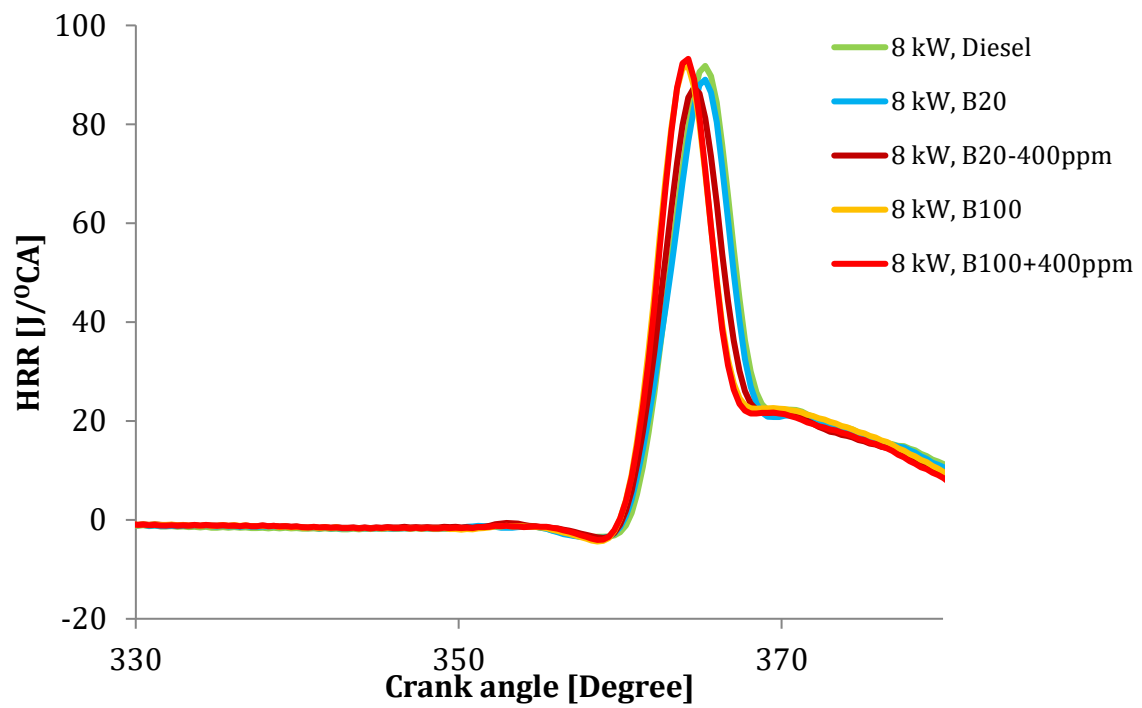
(a)



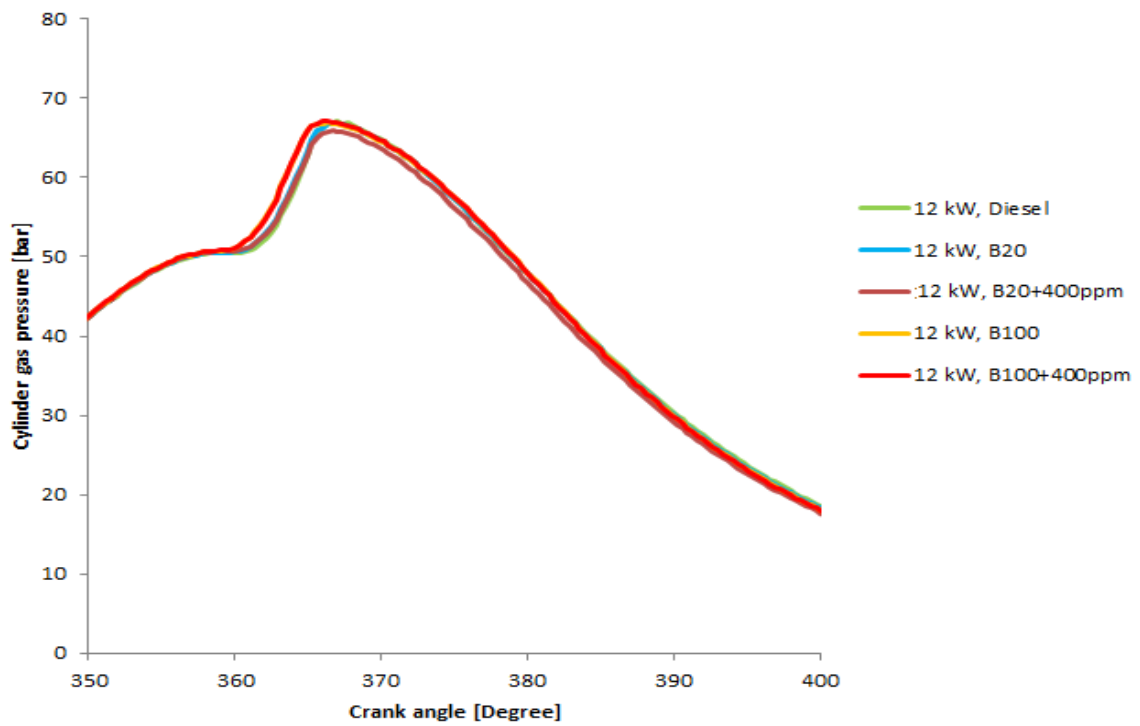
(b)



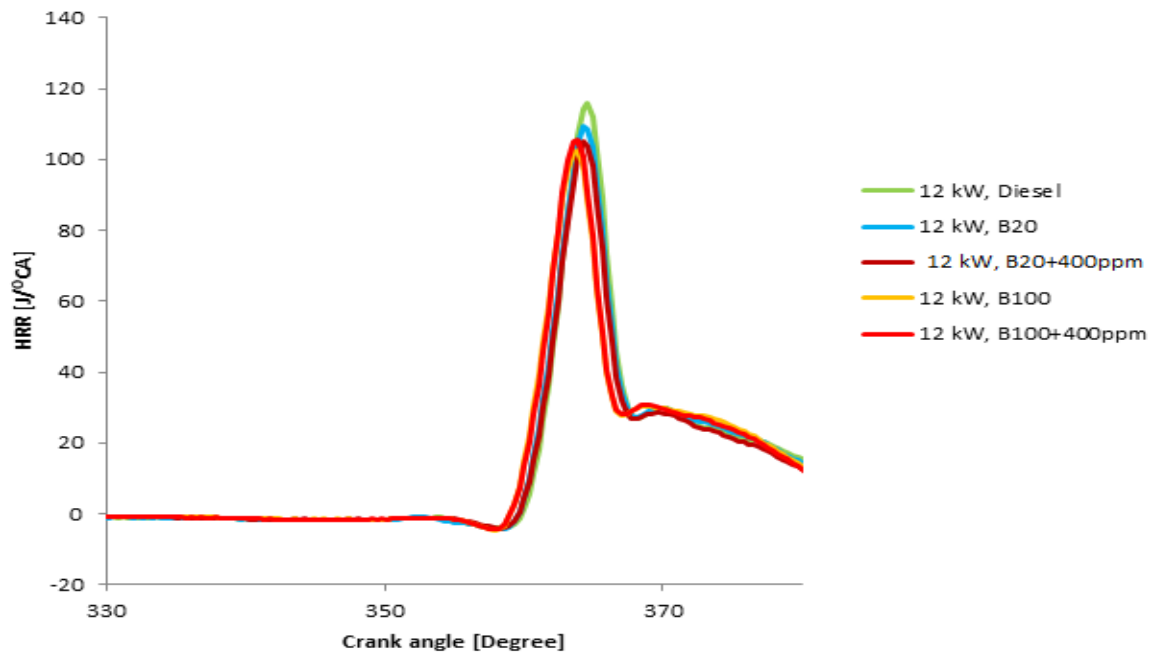
(a)



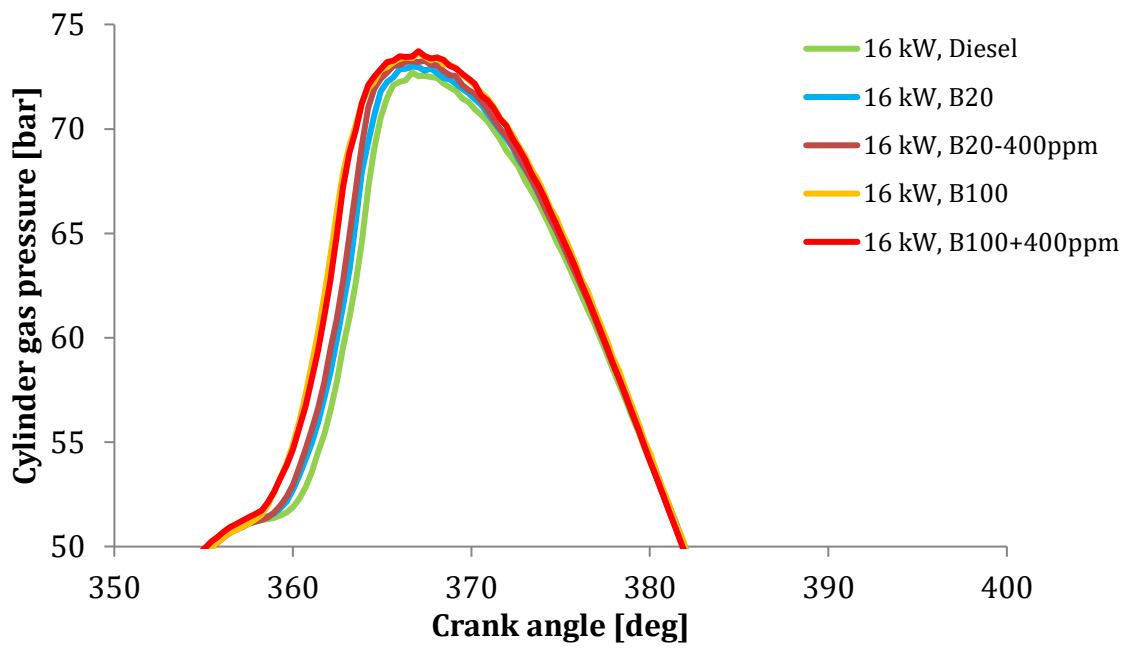
(b)



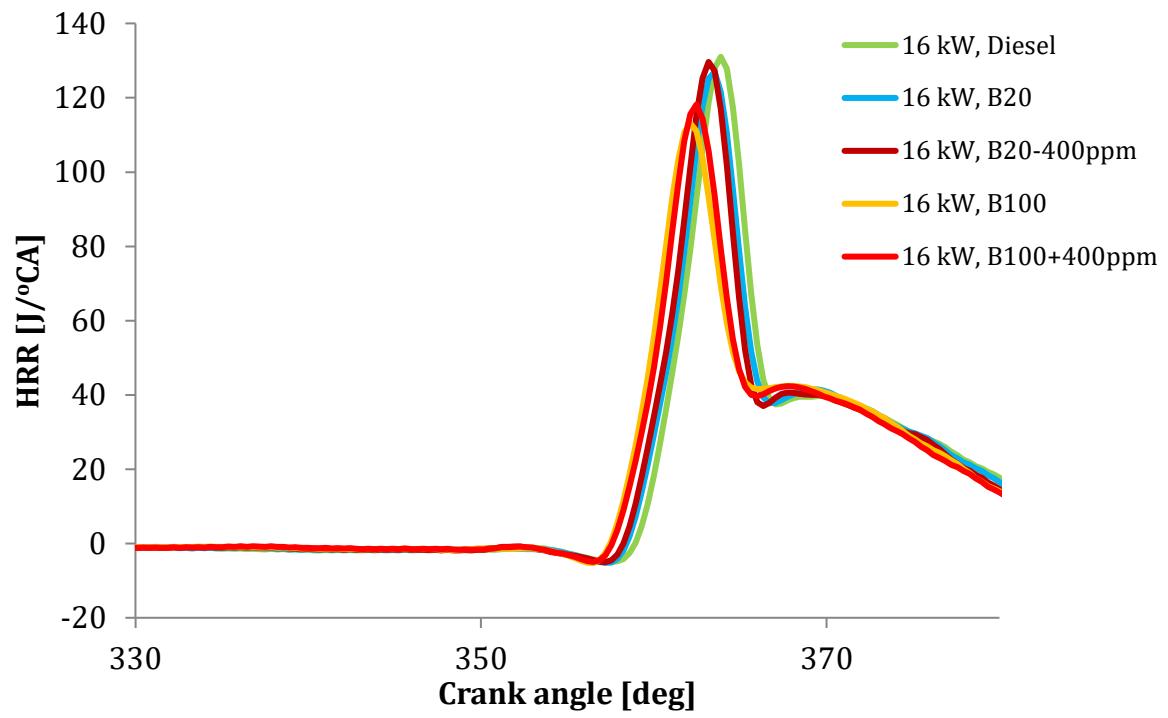
(a)



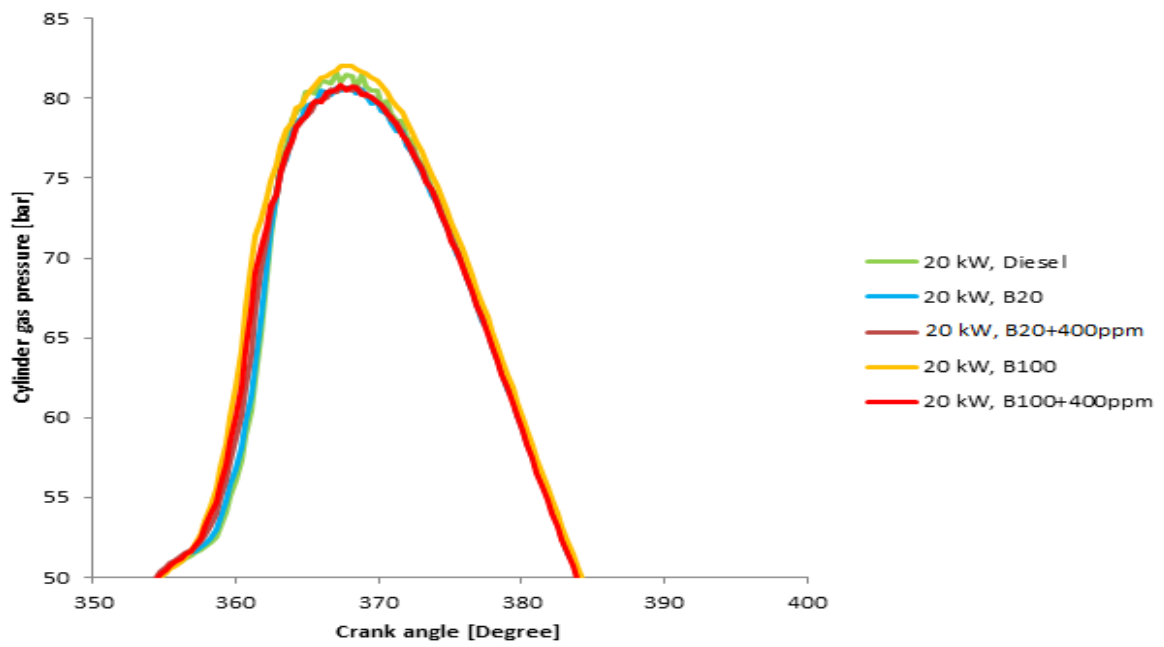
(b)



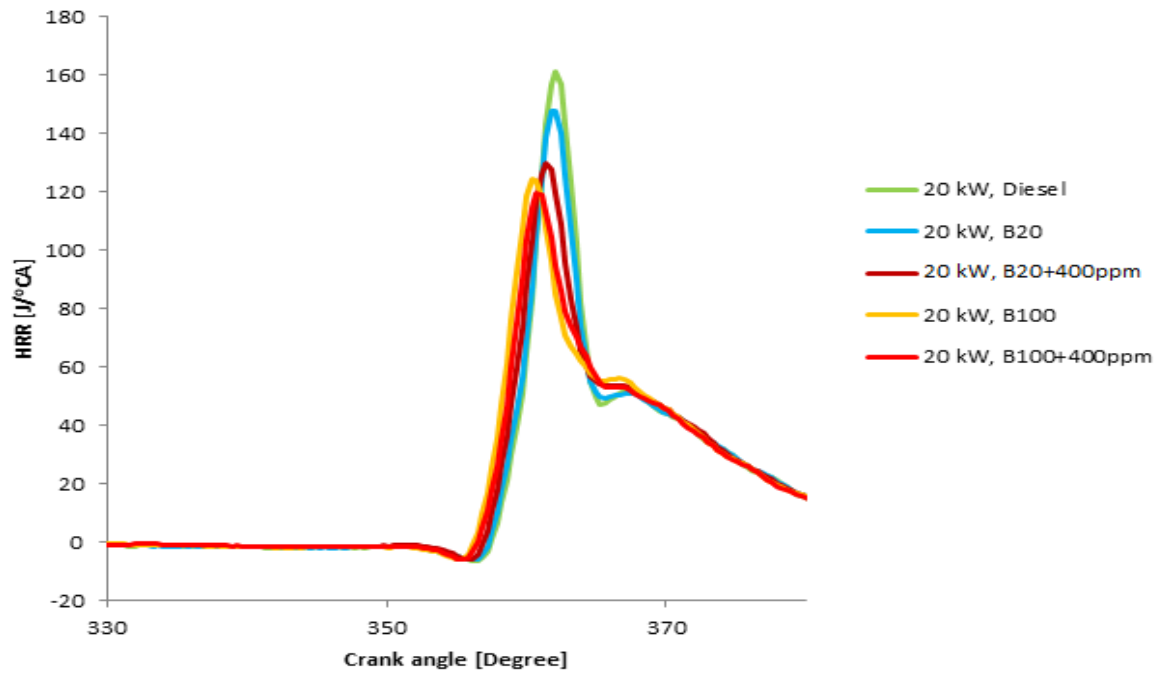
(a)



(b)



(a)



(b)

**Figure 28:** The variation of (a) CGP and (b) HRR profile of the test fuels at 0, 4, 8, 12, 16, and 20 kW brake powers

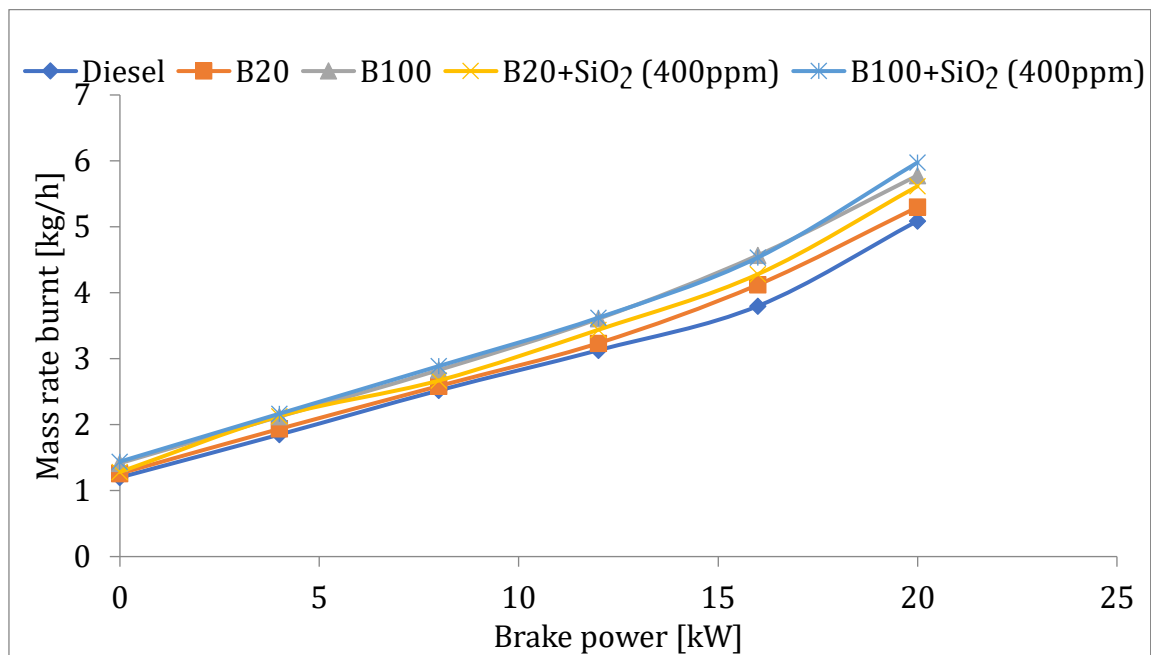


**Figure 29:** The mass rate burnt as a function of brake power

#### 4.7.4 Variation of Crank Angle (CA) for Test Fuels at Minimum and Maximum Brake Power

Figure 30(a) and (b) displayed the variation of crank angle (CA) of test fuels at minimum and maximum brake power respectively. The result shows at minimum brake power (0 kW), B0, B20, and B20+SiO<sub>2</sub> fuels showed faster earlier combustion during the start of combustion (SoC) than all other fuels, this is probably due to the higher calorific value of diesel which led to fast atomization of injected fuels. On the contrary, the effect of maximum engine BP (20 kW) and test fuel type on CA, results observed that in comparison to B20+SiO<sub>2</sub> and B100+SiO<sub>2</sub>, it was found that CA points retarded with B20 because of more fuel being injected, which was linked to its lower calorific value and late SoC. In comparison with B100 and B100+SiO<sub>2</sub> to pure B0, the fuel burned more quickly, presumably as a result of better fuel reactivity and air-fuel mixing. When engine efficiency was taken into account, the best CA points for all test fuels under various engine settings were found to be within 357 CA after Total Dead Center (aTDC) for 50% of the fuel consumed. Because of its lower calorific value, B100 burnt more quickly than diesel during both the rapid and controlled combustion stages, even though more fuel was injected. It might be due to the micro-explosion of injected fuel producing finer fuel droplets, which enhance air-fuel mixing and burning (Ampah *et al.*, 2022).

In addition to improved air-fuel mixing, nanoparticles played the role of catalytic which enhances the fastest combustion with B100+SiO<sub>2</sub> among all the test fuels. The mean rapid combustion duration for B100+SiO<sub>2</sub> was reduced by 0.29, 0.19, and 0.09% compared to neat B0, B20, and B20+SiO<sub>2</sub>, respectively. The length of rapid combustion duration is associated with NO<sub>x</sub> formation because these pollutants are predominantly formed in the primary phase of combustion due to high cylinder temperature and oxygen availability. In general, the mean total combustion duration for B100+SiO<sub>2</sub> test fuel recorded shortened ID by 0.39, 0.39. and 0.19% lesser than those of B0, B20, and B20+SiO<sub>2</sub>, respectively at all crank-shaft rotations conditions such as at the SoC, maximum heat release rate ( $HRR_{max}$ ), maximum indicated pressure ( $P_{max}$ ), and maximum value of change in heat release rate ( $dHRR/dCA, max$ ).



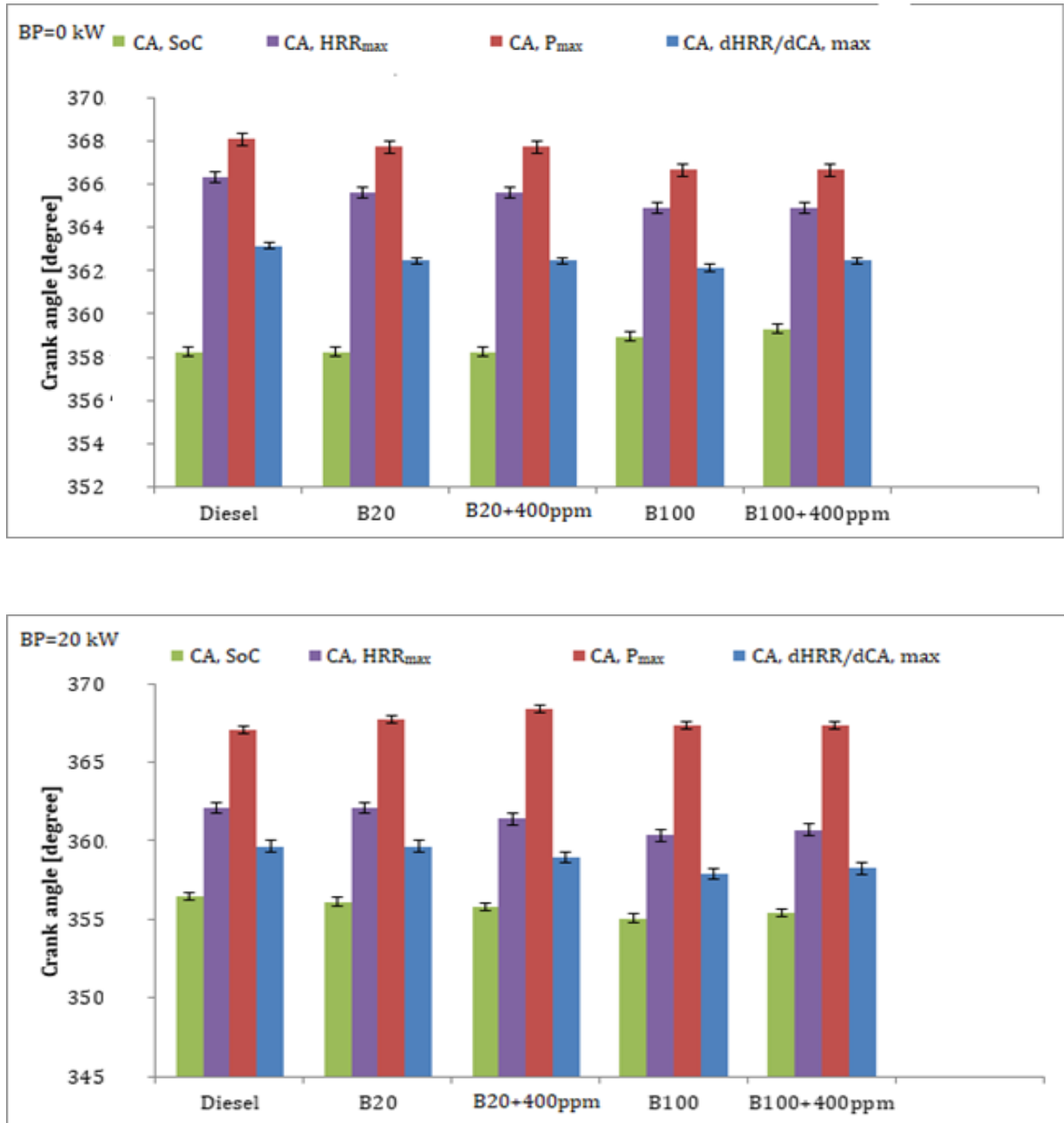


**Figure 30: The variation of the crank angle at (a) minimum and (b) maximum brake power**

## 4.8 Engine Exhausts Emission Analysis

### 4.8.1 Total Hydrocarbon (THC) Emission

Total hydrocarbon (THC) emissions are influenced by several factors, including combustion chamber temperature, inadequate atomization pattern resulting in inadequate mixing and locally fuel-rich mixture, flame quenching effect, and nozzle sac (Heywood, 2018). The

injector of the used CI engine is characterized by 3 large holes that are sensitive to viscosity and have a high ID due to its low compression ratio as a result a large proportion of the fuel forms a fuel film on the piston surface and evaporates. Therefore, it is assumed that the absorption and desorption of the impurities deposited in the combustion chamber also result in considerable THC emissions (Heywood, 2018). It can be observed in Fig. 31 that the measured values do not differ significantly at idle run and low load.

As previously stated, adding nanoparticles raises the temperature and pressure of the combustion process and hence, improves combustion efficiency. When compared to baseline B0 fuel, B100 and B100+SiO<sub>2</sub> (400 ppm) recorded the lowest THC emissions at low BP. It is observed that B100, B20+SiO<sub>2</sub>, and B100+SiO<sub>2</sub> fuel blends showed the highest THC emissions at medium and maximum BP compared to neat B0. Therefore, at maximum BP, B20+SiO<sub>2</sub> and B100+SiO<sub>2</sub> observed a reduction of THC emission by 17.7 and 3.7% respectively, compared to neat B100. Since biodiesel fuel has higher viscosity and density, the atomization pattern has deteriorated, but the addition of oxygen content derived from nanoparticles increases the temperature and pressure of the combustion process and hence improves combustion efficiency and reduces THC emissions. This can be observed at idle running (0 kW), with B20 and B100 having the same or reduced THC emissions compared to B0, with the addition of 400 ppm of SiO<sub>2</sub> leading to further reduction. This effect is not always observed at medium loads, so presumably the flame quenching effect and the effect of nozzle sac volume are more significant.

At full load (20 kW), THC emissions at B100 increased significantly, probably due to poorer atomization, with the addition of 400 ppm SiO<sub>2</sub> reducing THC emissions, but still higher than that of B0. These results were almost fairly in agreement with previous studies reported by Sivasaravanan *et al.* (2019) in which the addition of rice husk nanoparticles to neem biodiesel blends, B10 and B20 showed a reduction of THC by 11.3 and 11.2%, respectively.

#### **4.8.2 Carbon Monoxide (CO) Emission**

The unavailability of excess air is a significant cause of CO formation, but this is mainly valid for spark ignition (SI) engines, for CI engines, a fuel-poor mixture is always predominant. Therefore, CO emissions are partly like THC emissions. The local excess air factor is likely a potential factor and is significantly influenced by atomization, mixture formation, processing temperature, flame quenching effect, and the equilibrium reaction of CO<sub>2</sub> and CO. The fluctuation in CO emission as a function of BP with all test fuels is displayed in Fig. 32. At

higher BP, CO emission increases following the trend;  $B20 < B20+SiO_2 < B100+SiO_2 < B100$ , this implies that  $B20+SiO_2$ , B20, and  $B100+SiO_2$  reduced by 21.3, 27.4, and 2.8% respectively compared to B100. It is observed that with increasing BP, CO emissions increase only slightly up to 12 kW, at 16 kW loads CO emissions decrease for B0, B20, and  $B20+SiO_2$  fuels compared to lower loads, and then at 20 kW load, CO emissions increase significantly. This may be because the combustion chamber temperature increases with increasing BP, but at this condition (20 kW) power, the amount of available air decreases. At all the powers tested, B100 and  $B100+SiO_2$  have the highest CO emissions, presumably due to the higher viscosity, which is not significantly reduced by the addition of nanoparticles, and therefore the deterioration of the atomization process is most significant, so the CO emissions were not reduced upon addition of nano-additives in this engine. This result shows a similar impact as reported by Hu *et al.* (2018).

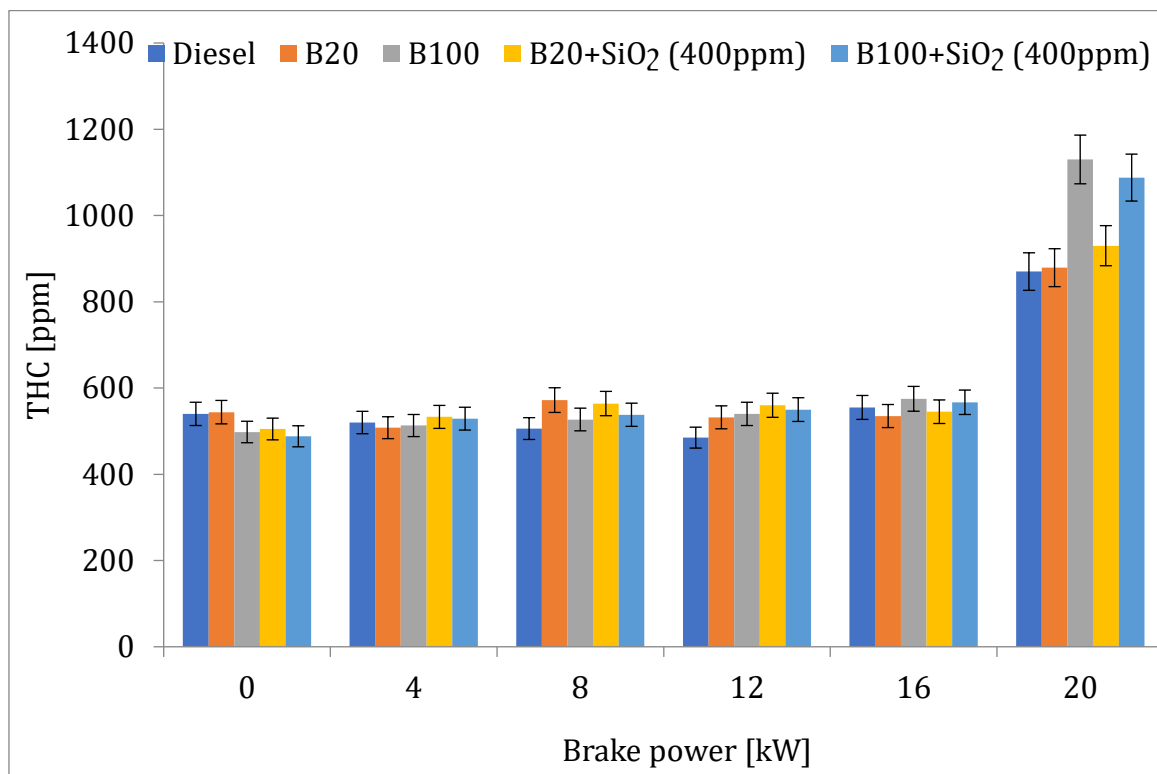


**Figure 31: Total hydrocarbon (THC) emission as a function of brake power**

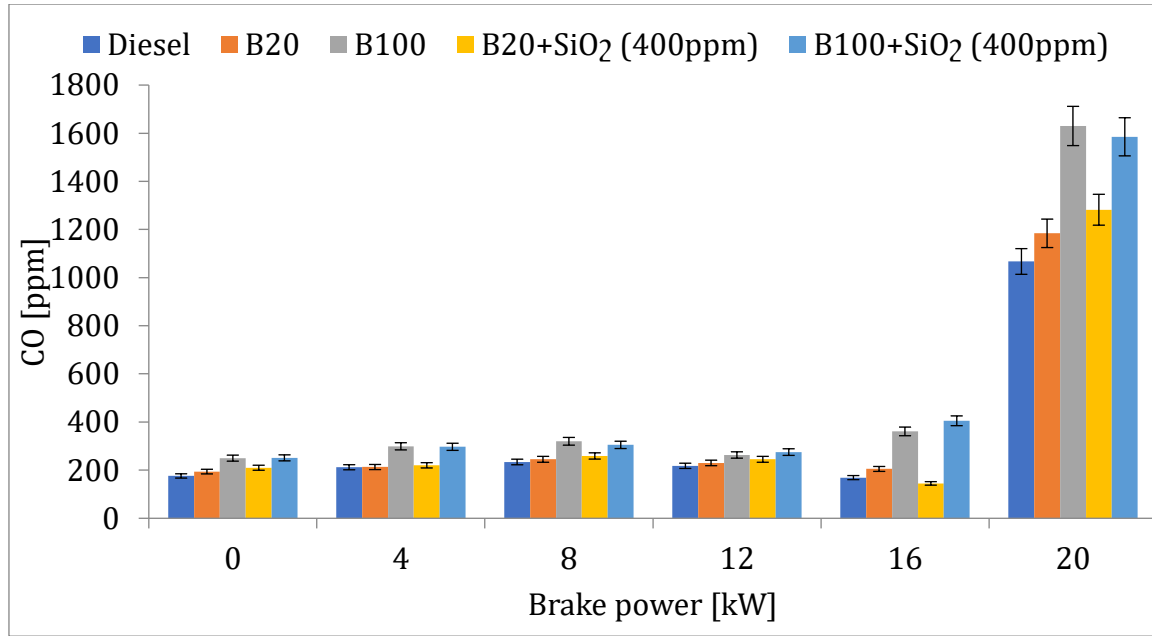


**Figure 32: Carbon monoxide (CO) emission as a function of brake power**

#### 4.8.3 Carbon Dioxide (CO<sub>2</sub>) Emission

The formation of CO<sub>2</sub> is associated with complete and quality combustion in the cylinder by converting CO to CO<sub>2</sub>. Figure 33 depicts the impact of different blended fuels on CO<sub>2</sub> emissions. All tested fuels showed tremendous increases as the BP increased. At low BP, B100 and B100+SiO<sub>2</sub> recorded almost slightly similar CO<sub>2</sub> emissions of about 1.7 v/vol%. B20+SiO<sub>2</sub> showed a reduction of 1.78% compared with B100. At medium BP (12 kW), B20+SiO<sub>2</sub> recorded lower emission by 0.62% compared to B20, this is due to the influence of SiO<sub>2</sub> nano-additive. However, B100+SiO<sub>2</sub> reported an increase of 0.61% compared with B100. At maximum BP, B20+SiO<sub>2</sub> and B100+SiO<sub>2</sub> recorded a reduction of CO<sub>2</sub> by 2.46 and 0.12% respectively compared to B100. It has been revealed that, at low and medium engine BP, B0 displayed the lowest CO<sub>2</sub> emission at about 1.61 and 4.8 v/vol% respectively, compared to all other fuels. However, the previous study reported by Özgür *et al.* (2015) showed a maximum increase of CO<sub>2</sub> emission by 2% and 2.7% when 25 and 50 ppm dosing level of SiO<sub>2</sub> was added to rape seed methyl ester respectively.

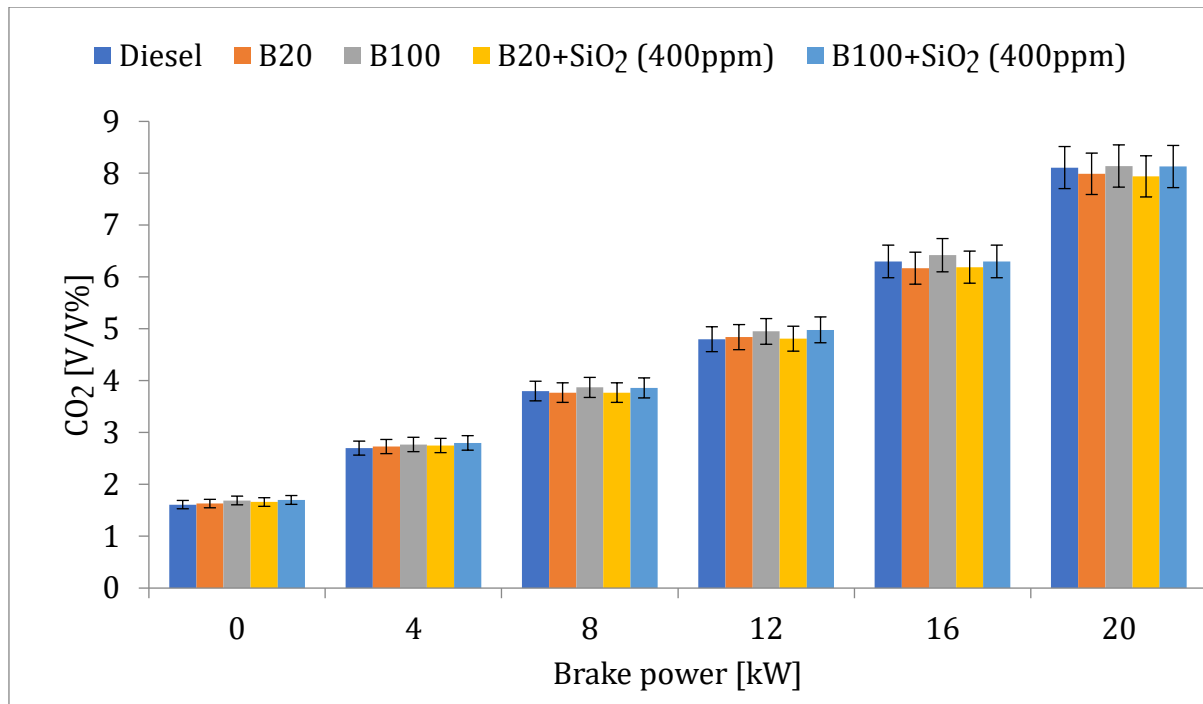


**Figure 33: Carbon dioxide (CO<sub>2</sub>) emission as a function of brake power**

#### 4.8.4 Oxides of Nitrogen (NO<sub>x</sub>) Emission

Figure 34 depicts NO<sub>x</sub> emissions for all the tested fuel samples. The results show that as the BP increases, NO<sub>x</sub> emissions increase as well. The NO<sub>x</sub> is produced at high temperatures in the post-flame regions. The addition of SiO<sub>2</sub> nanoparticles facilitates the reduction of NO<sub>x</sub> emissions. At the idle run (0 kW) B20, B100, B20+SiO<sub>2</sub>, and B100+SiO<sub>2</sub> recorded the reduction of NO<sub>x</sub> emission by 4.1, 2.83, 5.29, and 2.8% compared to B0. However, at maximum BP, B20+SiO<sub>2</sub> reported a lower emission than all other fuel blends. The addition of SiO<sub>2</sub> nanoparticles facilitates the reduction of NO<sub>x</sub> emissions. On the other hand, the biodiesel blends and B20 sprayed better once the nanoparticles were added. The distinct qualities of nanoparticles, like enhanced spray, heat transmission, and thermal conductivity, may have enhanced the quality of combustion. This is most likely the result of enhanced mass and heat transfer during combustion, which decreased flame spots and, in turn, decreased the total amount of NO<sub>x</sub> generation (Sivasaravanan *et al.*, 2019).

Furthermore, the biodiesel had lower calorific values than B0 which implies less heat would be generated, resulting in lower combustion temperatures for the RH nanoparticles added to the biodiesel blends (Zhang *et al.*, 2018; Nour *et al.*, 2019). Therefore, NO<sub>x</sub> emissions were reduced in both B100 and B20 upon the addition of nano-additives. At maximum BP, B100, B20+SiO<sub>2</sub>, and B100+SiO<sub>2</sub> recorded the reduction of NO<sub>x</sub> emission by 9.1, 10, and 8.97%

respectively, as compared to B0. These results are similar to an earlier study reported by Attia *et al.* (2014) in which  $\text{Al}_2\text{O}_3$  was doped with jojoba biodiesel blends and they found the 20 mg concentration of nanoparticle reduced the  $\text{NO}_x$  emission. Diesel causes earlier start premixed combustion, which raises the chamber's combustion temperature and increases  $\text{NO}_x$  emissions compared to B100 fuel as reported by Alloune *et al.* (2018). Generally, higher  $\text{NO}_x$  emissions from biodiesels are caused by fuel-bound oxygen, flame temperature, fuel characteristics, and residency. It can be advised to minimize  $\text{NO}_x$  emissions by increasing the fuel blending ratio, emulsification technique, and using a nanoparticle-reducing agent that can reduce  $\text{NO}_x$  to oxygen and nitrogen (Singh *et al.*, 2017).

#### **4.8.5 Particulate Matter (PM) Emission**

Smoke is indicative of dry soot emissions which is the main reason behind the formation of PM (Wei *et al.*, 2021). It is the basis of measuring the amount of smoke coming from a diesel engine. Smoke emissions occur in oxygen-deficient combustion environments due to the thermal cracking of the long-chain hydrocarbon compound molecules (Ulusoy, 2020). Figure 35 shows the effects of engine BP and all the tested fuels on PM. It is observed that the PM rises as BP increases due to the increase of fuel accumulation inside the combustion chamber. Compared with the pure biodiesel mode and nano-fuel blends, the B0 and B20 show slightly high PM emissions from low to high BP. This can be ascribed to the fuel-borne oxygen in biodiesel which improves the combustion process.

Generally, other input factors have less impact on the generation of PM. On the other hand, the addition of  $\text{SiO}_2$  nano-additives to B100, and B20 results in a better micro-explosion of the blend due to plenty of oxygen on the nanoparticle, resulting in less PM that facilitates complete combustion. The results showed that at low engine BP, PM emissions for B20+ $\text{SiO}_2$ , and B100+ $\text{SiO}_2$  fuel blends were reduced by 31.6 and 21.1% compared to that of B20 and B100 respectively. In addition, at both medium and maximum BP, increased PM emission for B0 and B20 and lower emission for B100, B20+ $\text{SiO}_2$ , and B100+ $\text{SiO}_2$ . The oxygen component of the fuel either avoids or oxidizes PM that has already been generated (Bae & Kim, 2017; Nabi & Rasul, 2018). The previous research reported by Gavhane *et al.* (2021) observed a reduction of smoke emission by 23.54 and 10.16% when  $\text{SiO}_2$  nanoparticle was added to Soyabean biodiesel blends (B25) at a dosage level of 50 and 75 ppm, respectively as compared to untreated B25.

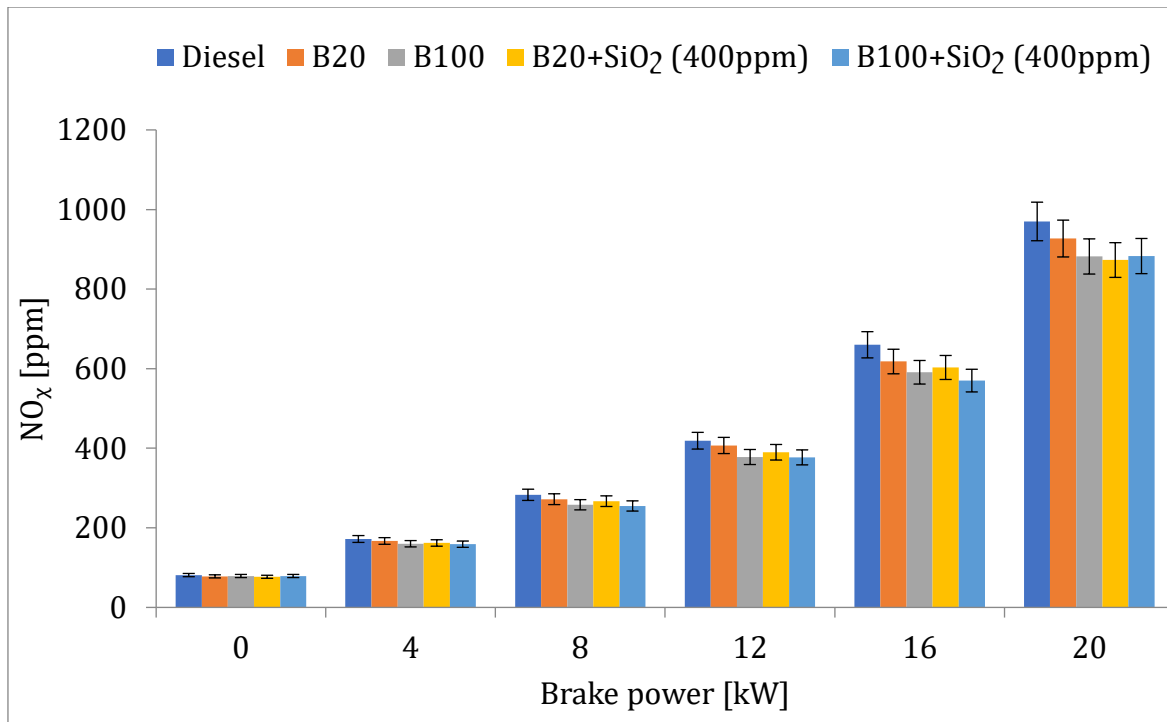


**Figure 34: Oxides of nitrogen (NOX) emission as a function of brake power**

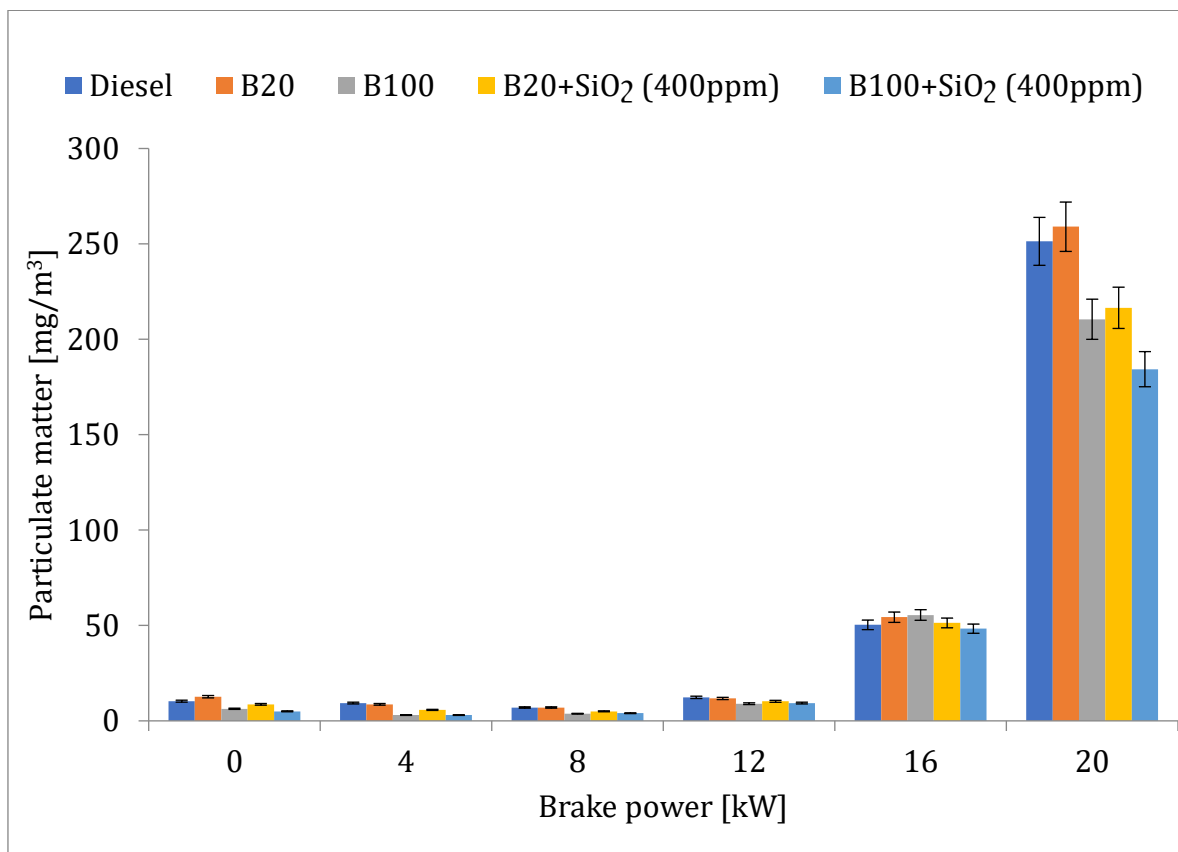


**Figure 35: Particulate matter (PM) emission as a function of brake power**

## CHAPTER FIVE

### CONCLUSION AND RECOMMENDATIONS

#### 5.1 Conclusion

This study investigates how RH agricultural waste can be used to produce an affordable SiO<sub>2</sub> nano-additive. The study also investigated the impact of these additives on ADME's (baobab biodiesel) fuel-related properties, CI diesel engine's performance, exhaust emission, and combustion characteristics. The results showed that at a reaction time of 4 h, a temperature of 65°C, and a methanol-to-oil molar ratio of 1:8, the maximum biodiesel yield was 94%. Determining the physicochemical characteristics of synthetic nano-silica, ADME, and ADSO was another goal of the current study. The measured parameters were within the implemented ASTM D6751 and EN 14214 standard limits. From 0 to 1000 ppm, different doses of nanoparticles were used. The OIP of 10.3 h at 800 ppm, kinematic viscosity of 2.21 mm<sup>2</sup>/s at 400 ppm, flash point of 202°C at 1000 ppm, and CN of 64 at 800 ppm all showed a marginally notable improvement.

Moreover, the influence on the performance, combustion, and emission characteristics of a four-stroke, 3-in line-cylinder CI diesel engine were investigated in this study and the general results showed that SiO<sub>2</sub> nano-additive enhanced ADME and its blends as a catalytic fuel additive and oxygen donor on organic carbon chain during the combustion process. The results showed that the mean value of BTE at maximum BP (20 kW load) for B20, B20+SiO<sub>2</sub>, B100, and B100+SiO<sub>2</sub> fuels were 29.9, 28.2, 28.44, and 27.1% respectively. BSFC for B20, B20+SiO<sub>2</sub>, B100, and B100+SiO<sub>2</sub> was reduced by 46.8, 49.7, 46.2, and 47.7%, respectively from 4 kW BP to 16 kW BP. However, B100 and B100+SiO<sub>2</sub> reported an increase in EGT by 7.77 and 6.67% as compared to B20. B0 and B20+SiO<sub>2</sub> showed a similar increase of 4.44% at full load. In addition, B100 recorded a maximum peak CGP of 82.1 bar, with B100+SiO<sub>2</sub> having a 1.56% higher peak CGP. B20 had a slightly lower peak CGP of 80.67 bar. The peak HRR was recorded to be 161.32, 147.74, 129.62, 124.7, and 119.45 J/°CA for B0, B20, B20+SiO<sub>2</sub>, B100, and B100+SiO<sub>2</sub> fuels respectively. Exhaust emission analysis revealed that B20+SiO<sub>2</sub>, B20, and B100+SiO<sub>2</sub> exhibited a reduction of CO emissions by 21.3, 27.4, and 2.8% respectively as compared to B100. Also, B20+SiO<sub>2</sub> and B100+SiO<sub>2</sub> observed a reduction of THC emission by 17.7 and 3.7% respectively, and CO<sub>2</sub> by 2.46 and 0.12% respectively compared to B100. However, NO<sub>x</sub> emission lowered by 10 and 8.97% respectively, as



compared to B0 at full load. PM emissions for B20+SiO<sub>2</sub> and B100+SiO<sub>2</sub> fuel blends were reduced by 31.6 and 21.1% compared to that of B20 and B100 respectively. This study recommends that SiO<sub>2</sub> as an alternative fuel additive improved almost all potential fuel properties as well as all performance, and combustion parameters, and reduced emissions in the CI diesel engine.

## **5.2 Recommendations**

This study recommends silica as a potential nano-additive and good oxidizer catalyst since they were able to improve important fuel properties and enhance engine performance, combustion, and reduce exhaust emission when doped with biodiesel and its blends.

- (i) This study observed that there is no significant influence of nanoparticles on cloud and pour point therefore, various types of antioxidants and cold flow improver additives will also need to be studied to ensure better combustion attributes.
- (ii) Techno-economic analysis and life cycle assessment should be conducted for further scale-up and eventually commercialization. This will help to minimize the selling price to encourage high profitability of fuels.
- (iii) Examining mass-energy balance should also be considered to determine the raw material used for the biodiesel processing industry and energy derived, to control the yield of the product.
- (iv) Chemico-kinetic analysis of biodiesel, when doped with nanoparticle additives, should also be analyzed to explore the detailed mechanism of the reaction.

## REFERENCES

- Abdulahaleem, S. M. (2019). Effect of SiO<sub>2</sub> nanoparticles added to diesel fuel on the performance and pollutant emissions of a four stroke diesel engine. *The Iraqi Journal for Mechanical and Materials Engineering*, 19(2), 129-137.
- Abubakar, S., Etim, V., Bwai, D., & Afolayan, M. (2015). Nutraceutical evaluation of baobab (*Adansonia digitata* L.) seeds and physicochemical properties of its oil. *Annals of Biological Sciences*, 3(2), 13-19.
- Adzmi, M. A., Abdullah, A., Abdullah, Z., & Mrwan, A. G. (2019). Effect of Al<sub>2</sub>O<sub>3</sub> and SiO<sub>2</sub> metal oxide nanoparticles blended with POME on combustion, performance and emissions characteristics of a diesel engine. *International Journal of Automotive and Mechanical Engineering*, 16(3), 6859-6873.
- Ağbulut, Ü., Karagöz, M., Sarıdemir, S., & Öztürk, A. (2020). Impact of various metal-oxide based nanoparticles and biodiesel blends on the combustion, performance, emission, vibration and noise characteristics of a CI engine. *Fuel*, 270, 117521.
- Aldhaidhawi, M., Chiriac, R., & Badescu V (2017). Ignition delay, combustion and emission characteristics of Diesel engine fueled with rapeseed biodiesel: A literature review. *Renewable and Sustainable Energy Reviews* 73:178–186, Elsevier.
- Alemzero, D., Acheampong, T., & Huaping, S. (2021). Prospects of wind energy deployment in Africa: Technical and economic analysis. *Renewable Energy*, 179, 652-666.
- Alloune, R., Balistrrou, M., Awad, S., Loubar, K., & Tazerout, M. (2018). Performance, combustion and exhaust emissions characteristics investigation using *Citrullus colocynthis* L. biodiesel in DI diesel engine. *Journal of the Energy Institute*, 91(3), 434-444.
- Alrefaai, M. M., Peña, G. D. G., Raj, A., Stephen, S., Anjana, T., & Dindi, A. (2018). Impact of dicyclopentadiene addition to diesel on cetane number, sooting propensity, and soot characteristics. *Fuel*, 216, 110-120.
- Alvarez, D., Perls, H., & Monast, J. (2024). Clearing the Air on Supplemental Environmental Projects. *Environmental Law Reporter*, 54, 10382.

- Amineh, M. P., & Yang, G. (2018). China's geopolitical economy of energy security: A theoretical and conceptual exploration. *African and Asian Studies*, 17(1-2), 9-39.
- Ampah, J. D., Yusuf, A. A., Agyekum, E. B., Afrane, S., Jin, C., Liu, H., & Kamel, S. (2022). Progress and recent trends in the application of nanoparticles as low carbon fuel additives: A state-of-the-art review. *Nanomaterials*, 12(9), 1515.
- Ashraful, A. M., Masjuki, H. H., Kalam, M. A., Rashedul, H. K., Sajjad, H., & Abedin, M. J. (2014). Influence of anti-corrosion additive on the performance, emission and engine component wear characteristics of an IDI diesel engine fueled with palm biodiesel. *Energy Conversion and Management*, 87, 48-57.
- Atabani, A. E., Shobana, S., Mohammed, M. N., Uğuz, G., Kumar, G., Arvindnarayan, S., & Ala'a, H. (2019). Integrated valorization of waste cooking oil and spent coffee grounds for biodiesel production: Blending with higher alcohols, FT-IR, TGA, DSC and NMR characterizations. *Fuel*, 244, 419-430.
- Attia, A. M., El-Seesy, A. I., El-Batsh, H. M., & Shehata, M. S. (2014). Effects of alumina nanoparticles additives into jojoba methyl ester-diesel mixture on diesel engine performance. In *ASME International Mechanical Engineering Congress and Exposition*, 46521, V06BT07A019.
- Bae, C., & Kim, J. (2017). Alternative fuels for internal combustion engines. *Proceedings of the Combustion Institute*, 36(3), 3389-3413.
- Bakhtawar, J., Irfan, M., Shakir, H. A., Khan, M., Ali, S., Saeed, S., & Franco, M. (2022). Trends in Biodiesel Production from Algae and Animal Fat Wastes: Challenges and Prospects. *Food Waste to Green Fuel: Trend & Development*, 255-278.
- Bhuiya, M. M. K., Rasul, M. G., Khan, M. M. K., Ashwath, N., & Azad, A. K. (2016). Prospects of 2<sup>nd</sup> generation biodiesel as a sustainable fuel. Part: 1 selection of feedstocks, oil extraction techniques and conversion technologies. *Renewable and Sustainable Energy Reviews*, 55, 1109-1128.
- Chidambaranathan, B., Kumarasami, D. P., Soundararajan, G., & Thulasiram, R. (2023). Performance and environmental impact assessment of diesel engine operating on high

viscous punnai oil–diesel blends. *Environmental Science and Pollution Research*, 30(22), 61177-61189.

- Blanco, A., Monte, M. C., Campano, C., Balea, A., Merayo, N., & Negro, C. (2018). Nanocellulose for industrial use: Cellulose nanofibers (CNF), cellulose nanocrystals (CNC), and bacterial cellulose (BC). In *Handbook of Nanomaterials for Industrial Applications*, 74-126.
- Buhari, M., Danbature, W. L., Muzakir, M. M., & Abubakar, B. A. (2014). Production of biodiesel from baobab seed oil. *Greener Journal of Agricultural Sciences*, 4(2), 022-026.
- Campbell-Lendrum, D., & Prüss-Ustün, A. (2019). Climate change, air pollution and noncommunicable diseases. *Bulletin of the World Health Organization*, 97(2), 160.
- Cercado, A. P. I., Ballesteros Jr, F. C., & Capareda, S. C. (2018). Biodiesel from three microalgae transesterification processes using different homogenous catalysts. *International Journal of Technology*, 9(4), 645-651.
- Chang, M. Y., Chan, E. S., & Song, C. P. (2021). Biodiesel production catalysed by low-cost liquid enzyme Eversa® Transform 2.0: Effect of free fatty acid content on lipase methanol tolerance and kinetic model. *Fuel*, 283, 119266.
- Chhabra, M., Saini, B. S., & Dwivedi, G. (2021). Impact assessment of biofuel from waste neem oil. *Energy Sources, Part A: Recovery, Utilization, and Environmental Effects*, 43(24), 3381-3392.
- Chidambaranathan, B., Gopinath, S., Aravindraj, R., Devaraj, A., Krishnan, S. G., & Jeevaanathan, J. K. S. (2020). The production of biodiesel from castor oil as a potential feedstock and its usage in compression ignition Engine: A comprehensive review. *Materials Today: Proceedings*, 33, 84-92.
- Chilabade, D. (2018). *Biodiesel production from plant oils of African origin* (Doctoral dissertation, North-West University).
- Chitiga, M., Kandiero, T., & Ngwenya, P. (2008). African Development Bank.

- Choudhary, K. D., Nayyar, A., & Dasgupta, M. S. (2018). Effect of compression ratio on combustion and emission characteristics of CI Engine operated with acetylene in conjunction with diesel fuel. *Fuel*, 214, 489-496.
- Cordero-Ravelo, V., & Schallenberg-Rodriguez, J. (2018). Biodiesel production as a solution to waste cooking oil (WCO) disposal. Will any type of WCO do for a transesterification process? A quality assessment. *Journal of Environmental Management*, 228, 117-129.
- Cuong, N. D., & Quang, D. T. (2020). Progress through synergistic effects of heterojunction in nanocatalysts: Review. *Vietnam Journal of Chemistry*, 58(4), 434-463.
- Devarajan, Y., Mahalingam, A., Munuswamy, D. B., & Arunkumar, T. (2018). Combustion, performance, and emission study of a research diesel engine fueled with palm oil biodiesel and its additive. *Energy & Fuels*, 32(8), 8447-8452.
- Dhar, A., Kevin, R., & Agarwal, A. K. (2012). Production of biodiesel from high-FFA neem oil and its performance, emission and combustion characterization in a single-cylinder DICl engine. *Fuel Processing Technology*, 97, 118-129.
- Eevera, T., Rajendran, K., & Saradha, S. J. R. E. (2009). Biodiesel production process optimization and characterization to assess the suitability of the product for varied environmental conditions. *Renewable Energy*, 34(3), 762-765.
- Emiroğlu, A. O., & Şen, M. (2018). Combustion, performance and exhaust emission characterizations of a diesel engine operating with a ternary blend (alcohol-biodiesel-diesel fuel). *Applied Thermal Engineering*, 133, 371-380.
- Encinar, J. M., Pardal, A., Sánchez, N., & Nogales, S. (2018). Biodiesel by transesterification of rapeseed oil using ultrasound: A kinetic study of base-catalysed reactions. *Energies*, 11(9), 2229.
- Erman, A. G., Hellier, P., & Ladommatos, N. (2020). The impact of ignition delay and further fuel properties on combustion and emissions in a compression ignition engine. *Fuel*, 262, 116155.

- Eshton, B., & Katima, J. H. (2015). Carbon footprints of production and use of liquid biofuels in Tanzania. *Renewable and Sustainable Energy Reviews*, 42, 672-680.
- Fayad, M. A., & Dhahad, H. A. (2021). Effects of adding aluminum oxide nanoparticles to butanol-diesel blends on performance, particulate matter, and emission characteristics of diesel engine. *Fuel*, 286, 119363.
- Fernandes, D. M., Sousa, R. M., de Oliveira, A., Morais, S. A., Richter, E. M., & Muñoz, R. A. (2015). *Moringa oleifera*: A potential source for production of biodiesel and antioxidant additives. *Fuel*, 146, 75-80.
- Folayan, A. J., Anawe, P. A. L., Aladejare, A. E., & Ayeni, A. O. (2019). Experimental investigation of the effect of fatty acids configuration, chain length, branching and degree of unsaturation on biodiesel fuel properties obtained from lauric oils, high-oleic and high-linoleic vegetable oil biomass. *Energy Reports*, 5, 793-806.
- Gad, M. S., El-Araby, R., Abed, K. A., El-Ibiari, N. N., El Morsi, A. K., & El-Diwani, G. I. (2018). Performance and emissions characteristics of CI engine fueled with palm oil/palm oil methyl ester blended with diesel fuel. *Egyptian Journal of Petroleum*, 27(2), 215-219.
- Gad, M. S., & Jayaraj, S. (2020). A comparative study on the effect of nano-additives on the performance and emissions of a diesel engine run on Jatropha biodiesel. *Fuel*, 267, 117168.
- Gajraj, R. S., Singh, G. P., & Kumar, A. (2018). Third-generation biofuel: Algal biofuels as a sustainable energy source. *Biofuels: Greenhouse Gas Mitigation and Global Warming: Next Generation Biofuels and Role of Biotechnology*, 307-325.
- Gavhane, R. S., Kate, A. M., Soudagar, M. E. M., Wakchaure, V. D., Balgude, S., Rizwanul Fattah, I. M., & Shahabuddin, M. (2021). Influence of silica nano-additives on performance and emission characteristics of Soybean biodiesel fuelled diesel engine. *Energies*, 14(5), 1489.
- Ghafoori, M., Ghobadian, B., Najafi, G., Layeghi, M., Rashidi, A., & Mamat, R. (2015). Effect of nano-particles on the performance and emission of a diesel engine using biodiesel-diesel blend. *International Journal of Automotive & Mechanical Engineering*, 12, 3097.

- Goyal, H., Kook, S., & Ikeda, Y. (2019). The influence of fuel ignition quality and first injection proportion on gasoline compression ignition (GCI) combustion in a small-bore engine. *Fuel*, 235, 1207-1215.
- Luciani, G. L. (2022). The Palgrave Handbook of International Energy Economics.
- Hanif, M. A., Nisar, S., Akhtar, M. N., Nisar, N., & Rashid, N. (2018). Optimized production and advanced assessment of biodiesel: A review. *International Journal of Energy Research*, 42(6), 2070-2083.
- Hazrat, M. A., Rasul, M. G., Khan, M. M. K., Mofijur, M., Ahmed, S. F., Ong, H. C., & Show, P. L. (2021). Techniques to improve the stability of biodiesel: A review. *Environmental Chemistry Letters*, 19, 2209-2236.
- Helwani, Z., Othman, M. R., Aziz, N., Fernando, W. J. N., & Kim, J. (2009). Technologies for production of biodiesel focusing on green catalytic techniques: A review. *Fuel Processing Technology*, 90(12), 1502-1514.
- Heywood JB (2018) *Internal combustion engine fundamentals*, McGraw-Hill Education.
- Hoang, A. T. (2021). Combustion behavior, performance and emission characteristics of diesel engine fuelled with biodiesel containing cerium oxide nanoparticles: A review. *Fuel Processing Technology*, 218, 106840.
- Hoseini, S. S., Najafi, G., Ghobadian, B., Mamat, R., Sidik, N. A. C., & Azmi, W. H. (2017). The effect of combustion management on diesel engine emissions fueled with biodiesel-diesel blends. *Renewable and Sustainable Energy Reviews*, 73, 307-331.
- Hoseini, S. S., Najafi, G., Ghobadian, B., Ebadi, M. T., Mamat, R., & Yusaf, T. J. R. E. (2020). Performance and emission characteristics of a CI engine using graphene oxide (GO) nano-particles additives in biodiesel-diesel blends. *Renewable Energy*, 145, 458-465.
- Hu, H., Xie, N., Fang, D., & Zhang, X. (2018). The role of renewable energy consumption and commercial services trade in carbon dioxide reduction: Evidence from 25 developing countries. *Applied Energy*, 211, 1229-1244.
- Hussain, M., Butt, A. R., Uzma, F., Ahmed, R., Irshad, S., Rehman, A., & Yousaf, B. (2020). A comprehensive review of climate change impacts, adaptation, and mitigation on

- environmental and natural calamities in Pakistan. *Environmental Monitoring and Assessment*, 192, 1-20.
- Imdadul, H. K., Masjuki, H. H., Kalam, M. A., Zulkifli, N. W. M., Kamruzzaman, M., Shahin, M. M., & Rashed, M. M. (2017). Evaluation of oxygenated n-butanol-biodiesel blends along with ethyl hexyl nitrate as cetane improver on diesel engine attributes. *Journal of Cleaner Production*, 141, 928-939.
- Jabbari, F., Rajabpour, A., & Saedodin, S. (2017). Thermal conductivity and viscosity of nanofluids: A review of recent molecular dynamics studies. *Chemical Engineering Science*, 174, 67-81.
- Jambulingam, R., Srinivasan, G. R., Palani, S., Munir, M., Saeed, M., & Mohanam, A. (2020). Process optimization of biodiesel production from waste beef tallow using ethanol as co-solvent. *SN Applied Sciences*, 2, 1-18.
- Jayanthi, P., & Rao, M. S. (2016). Effects of nanoparticles additives on performance and emissions characteristics of a DI diesel engine fuelled with biodiesel. *International Journal of Advances in Engineering & Technology*, 9(6), 689.
- Jayaraman, J., Alagu, K., Appavu, P., Joy, N., & Mariadhas, A. (2020). Impact of methyl, ethyl, and butyl ester blends of freshwater algae oil on the combustion, performance, and emissions of a CI engine. *Energy & Fuels*, 34(8), 9763-9770.
- Jung, M. R., Horgen, F. D., Orski, S. V., Rodriguez, V., Beers, K. L., Balazs, G. H., & Lynch, J. M. (2018). Validation of ATR FT-IR to identify polymers of plastic marine debris, including those ingested by marine organisms. *Marine Pollution Bulletin*, 127, 704-716.
- Kaimal, A. M., Tidke, V. B., Mujumdar, A. S., & Thorat, B. N. (2022). Food security and sustainability through solar drying technologies: A case study based on solar conduction dryer. *Materials Circular Economy*, 4, 1-23.
- Kalaimurugan, K., Karthikeyan, S., Periyasamy, M., Mahendran, G., & Dharmaprabhakaran, T. (2023). Experimental studies on the influence of copper oxide nanoparticle on biodiesel-diesel fuel blend in CI engine. *Energy Sources, Part A: Recovery, Utilization, and Environmental Effects*, 45(3), 8997-9012.



- Kamatou, G. P. P., Vermaak, I., & Viljoen, A. M. (2011). An updated review of *Adansonia digitata*: A commercially important African tree. *South African Journal of Botany*, 77(4), 908-919.
- Kapile, F. A., Bereczky, A., Ntalikwa, J. W., & Kivevele, T. T. (2022). Comprehensive analysis of fuel properties of *Adansonia digitata* methyl ester with the influence of nanoparticle additives extracted from an agricultural waste. *Waste and Biomass Valorization*, 13(6), 2927-2945.
- Karthickeyan, V. (2019). Effect of combustion chamber bowl geometry modification on engine performance, combustion and emission characteristics of biodiesel fuelled diesel engine with its energy and exergy analysis. *Energy*, 176, 830-852.
- Kaufman, J. D., Elkind, M. S., Bhatnagar, A., Koehler, K., Balmes, J. R., Sidney, S., & American Heart Association Advocacy Coordinating Committee. (2020). Guidance to reduce the cardiovascular burden of ambient air pollutants: A policy statement from the American Heart Association. *Circulation*, 142(23), e432-e447.
- Kazimierczuk, A. H. (2019). Wind energy in Kenya: A status and policy framework review. *Renewable and Sustainable Energy Reviews*, 107, 434-445.
- Kirubakaran, M., & Selvan, V. A. M. (2018). A comprehensive review of low cost biodiesel production from waste chicken fat. *Renewable and Sustainable Energy Reviews*, 82, 390-401.
- Kumar, C. B., Lata, D. B., & Mahto, D. (2020). Analysis of ignition delay by taking Di-tertiary-butyl peroxide as an additive in a dual fuel diesel engine using hydrogen as a secondary fuel. *International Journal of Hydrogen Energy*, 45(29), 14806-14820.
- Kumar, N., & Tomar, M. (2019). Influence of nanoadditives on ignition characteristics of Kusum (*Schleichera oleosa*) biodiesel. *International Journal of Energy Research*, 43(8), 3223-3236.
- Kumar, S., Shamsuddin, M. R., Farabi, M. A., Saiman, M. I., Zainal, Z., & Taufiq-Yap, Y. H. (2020). Production of methyl esters from waste cooking oil and chicken fat oil via simultaneous esterification and transesterification using acid catalyst. *Energy Conversion and Management*, 226, 113366.

- Kunc, F., Balhara, V., Sun, Y., Daroszewska, M., Jakubek, Z. J., Hill, M., & Johnston, L. J. (2019). Quantification of surface functional groups on silica nanoparticles: Comparison of thermogravimetric analysis and quantitative NMR. *Analyst*, 144(18), 5589-5599.
- Kweku, D. W., Bismark, O., Maxwell, A., Desmond, K. A., Danso, K. B., Oti-Mensah, E. A., & Adormaa, B. B. (2018). Greenhouse effect: Greenhouse gases and their impact on global warming. *Journal of Scientific Research and Reports*, 17(6), 1-9.
- Lalji, S. M., Ali, S. I., Hussain, S., Ali, S. M., & Lashari, Z. A. (2023). Variations in cold flow and physical properties of Northern Pakistan gas condensate oil after interacting with different polymeric drilling mud systems. *Arabian Journal of Geosciences*, 16(8), 477.
- Lamayi, D. W., Jauro, A. L. I. Y. U., & MALGWI, A. H. (2016). Production and optimization of ethyl ester produced from *Adansonia digitata* seed oil. *Journal of Applied Chemical Science International*, 6(4), 186-194.
- Lapham, D. P., & Lapham, J. L. (2019). Gas adsorption on commercial magnesium stearate: The origin of atypical isotherms and BET transform data. *Powder Technology*, 342, 676-689.
- Loganathan, S., Valapa, R. B., Mishra, R. K., Pugazhenth, G., & Thomas, S. (2017). Thermogravimetric analysis for characterization of nanomaterials. In *Thermal and Rheological Measurement Techniques for Nanomaterials Characterization*, 67-108.
- Long, M., Petek, S., Artigaud, S., Legrand, F., Le Squin, L., Guillonneau, R., & Hégaret, H. (2018). Partial purification of *Alexandrium minutum* allelochemicals. *Marc Long*, 163.
- Lv, J., Wang, S., & Meng, B. (2022). The effects of nano-additives added to diesel-biodiesel fuel blends on combustion and emission characteristics of diesel engine: A review. *Energies*, 15(3), 1032.
- Maheshwari, P., Haider, M. B., Yusuf, M., Klemeš, J. J., Bokhari, A., Beg, M., & Jaiswal, A. K. (2022). A review on latest trends in cleaner biodiesel production: Role of feedstock, production methods, and catalysts. *Journal of Cleaner Production*, 355, 131588.

- Mahmud, S., Haider, A. R., Shahriar, S. T., Salehin, S., Hasan, A. M., & Johansson, M. T. (2022). Bioethanol and biodiesel blended fuels: Feasibility analysis of biofuel feedstocks in Bangladesh. *Energy Reports*, 8, 1741-1756.
- Maji, I. K., Sulaiman, C., & Abdul-Rahim, A. S. (2019). Renewable energy consumption and economic growth nexus: A fresh evidence from West Africa. *Energy Reports*, 5, 384-392.
- Maroa, S., & Inambao, F. (2021). A review of sustainable biodiesel production using biomass derived heterogeneous catalysts. *Engineering in Life Sciences*, 21(12), 790-824.
- Masera, K. (2019). *Biodiesel-biodiesel mixtures to upgrade fuel properties and lower exhaust gas emissions* (Doctoral dissertation, Aston University).
- Masera, K., Hossain, A. K., Davies, P. A., & Doudin, K. (2021). Investigation of 2-butoxyethanol as biodiesel additive on fuel property and combustion characteristics of two neat biodiesels. *Renewable Energy*, 164, 285-297.
- Mathew, G. M., Raina, D., Narisetty, V., Kumar, V., Saran, S., Pugazhendhi, A., & Binod, P. (2021). Recent advances in biodiesel production: Challenges and solutions. *Science of the Total Environment*, 794, 148751.
- Mauer, L. J. (2024). Moisture and total solids analysis. In *Nielsen's Food Analysis*, 233-260. Cham: Springer International Publishing.
- Mei, D., Fang, Y., Zhang, Z., Guo, D., Chen, Z., & Sun, C. (2021). Analysis of surface tension for nano-fuels containing disparate types of suspended nanoparticles. *Powder Technology*, 388, 526-536.
- Mishra, V. K., & Goswami, R. (2018). A review of production, properties and advantages of biodiesel. *Biofuels*, 9(2), 273-289.
- Moazeni, F., Chen, Y. C., & Zhang, G. (2019). Enzymatic transesterification for biodiesel production from used cooking oil: A review. *Journal of Cleaner Production*, 216, 117-128.
- Mohadesi, M., Aghel, B., Gouran, A., & Razmehgir, M. H. (2022). Transesterification of waste cooking oil using Clay/CaO as a solid base catalyst. *Energy*, 242, 122536.

- Mohammed, H. M. (2018). *Extraction and Characterization of the oil, Biodiesel and it's blends from Adansonia digitata (Baobab) seed* (Doctoral Thesis, Sudan University of Science and Technology).
- Musoni, N. E. (2018). *Analysis of the effect of renewable generation on the power quality of the grid, modelling and analysis of harmonic and voltage distortion* (Doctoral dissertation, Cape Peninsula University of Technology).
- Mustayen, A. G. M. B., Wang, X., Rasul, M. G., Hamilton, J. M., & Negnevitsky, M. (2022). Thermodynamic analysis of diesel engine ignition delay under low load conditions. *Energy Reports*, 8, 495-501.
- Nabi, M. N., & Rasul, M. G. (2018). Influence of second generation biodiesel on engine performance, emissions, energy and exergy parameters. *Energy Conversion and Management*, 169, 326-333.
- Nabora, C. S., Kingondy, C. K., & Kivevele, T. T. (2019). Tamarindus Indica fruit shell ash: A low cost and effective catalyst for biodiesel production from *Parinari curatellifolia* seeds oil. *SN Applied Sciences*, 1, 1-9.
- Najafi, G. (2018). Diesel engine combustion characteristics using nano-particles in biodiesel-diesel blends. *Fuel*, 212, 668-678.
- Najeeb, J., Akram, S., Mumtaz, M. W., Danish, M., Irfan, A., Touqeer, T., & Choong, T. S. Y. (2021). Nanobiocatalysts for biodiesel synthesis through transesterification: A review. *Catalysts*, 11(2), 171.
- Narowska, B., Kułczyński, M., Łukaszewicz, M., & Burchacka, E. (2019). Use of activated carbons as catalyst supports for biodiesel production. *Renewable Energy*, 135, 176-185.
- Nielsen, S. S. (2010). Determination of moisture content. *Food Analysis Laboratory Manual*, 17-27.
- Nour, M., Attia, A. M., & Nada, S. A. (2019). Combustion, performance and emission analysis of diesel engine fuelled by higher alcohols (butanol, octanol and heptanol)/diesel blends. *Energy Conversion and Management*, 185, 313-329.

- Oi-Uchisawa, J., Wang, S., Nanba, T., Ohi, A., & Obuchi, A. (2003). Improvement of Pt catalyst for soot oxidation using mixed oxide as a support. *Applied Catalysis B: Environmental*, 44(3), 207-215.
- Ooi, J. B., Ismail, H. M., Tan, B. T., & Wang, X. (2018). Effects of graphite oxide and single-walled carbon nanotubes as diesel additives on the performance, combustion, and emission characteristics of a light-duty diesel engine. *Energy*, 161, 70-80.
- Özgür, T., Özcanlı, M., & Aydın, K. (2015). Investigation of nanoparticle additives to biodiesel for improvement of the performance and exhaust emissions in a compression ignition engine. *International Journal of Green Energy*, 12(1), 51-56.
- Oztig, L. I. (2017). Europe's climate change policies: The Paris Agreement and beyond. *Energy Sources, Part B: Economics, Planning, and Policy*, 12(10), 917-924.
- Pandey, S., & Sharma, A. K. (2021). Combustion and Formation of Emissions in Compression Ignition Engines and Emission Reduction Techniques. In *Petrodiesel Fuel*, 977-993. CRC Press.
- Pepenene, R. D. (2018). *Macroscopic and Microscopic surface features of Hydrogenated silicon thin films* (Master dissertation, University of the Western Cape).
- Pham, P. X., Pham, N. V., Pham, T. V., Nguyen, V. H., & Nguyen, K. T. (2021). Ignition delays of biodiesel-diesel blends: Investigations into the role of physical and chemical processes. *Fuel*, 303, 121251.
- Poulose, A., Shibina, T., Sreejith, T., Mercy, A. S., Das, D., Haritha, K., & Mathew, G. (2023). Characterization of Nontoxic Nanomaterials for Biological Applications. *Biomedical Applications and Toxicity of Nanomaterials*, 363-400.
- Prasad, C. S., Maiti, K. N., & Venugopal, R. (2003). Effect of substitution of quartz by rice husk ash and silica fume on the properties of whiteware compositions. *Ceramics International*, 29(8), 907-914.
- Praveena, V., Martin, M. L. J., & Geo, V. E. (2020). Experimental characterization of CI engine performance, combustion and emission parameters using various metal oxide

- nanoemulsion of grapeseed oil methyl ester. *Journal of Thermal Analysis and Calorimetry*, 139(6), 3441-3456.
- Raja, P. M., & Barron, A. R. (2021). BET surface area analysis of nanoparticles. *Rice University*.
- Razak, N. H., Hashim, H., Yunus, N. A., & Klemeš, J. J. (2021). Reducing diesel exhaust emissions by optimisation of alcohol oxygenates blend with diesel/biodiesel. *Journal of Cleaner Production*, 316, 128090.
- Reddy, M. S., Sharma, N., & Agarwal, A. K. (2016). Effect of straight vegetable oil blends and biodiesel blends on wear of mechanical fuel injection equipment of a constant speed diesel engine. *Renewable Energy*, 99, 1008-1018.
- Rempel, A. (2023). An Unsettled “Stranded Asset Debt”? Proposing a Supply-Side Counterpart to the “Climate Debt” in a Bid to Guide a Just Transition from Fossil Fuels in South Africa and Beyond. *Antipode*, 55(1), 243-267.
- Rezania, S., Oryani, B., Park, J., Hashemi, B., Yadav, K. K., Kwon, E. E., & Cho, J. (2019). Review on transesterification of non-edible sources for biodiesel production with a focus on economic aspects, fuel properties and by-product applications. *Energy Conversion and Management*, 201, 112155.
- Ritchie, H., & Roser, M. (2019). Outdoor air pollution. *Our world in data*.
- Rosi, F., Cartechini, L., Sali, D., & Miliani, C. (2019). Recent trends in the application of Fourier Transform Infrared (FT-IR) spectroscopy in Heritage Science: From micro-to non-invasive FT-IR. *Physical Sciences Reviews*, 4(11), 20180006.
- Rozina, Ahmad, M., Zafar, M., Yousaf, Z., Ullah, S. A., Sultana, S., & Bibi, F. (2022). Identification of novel, non-edible oil seeds via scanning electron microscopy as potential feedstock for green synthesis of biodiesel. *Microscopy Research and Technique*, 85(2), 708-720.
- Sajith, V., Sobhan, C. B., & Peterson, G. P. (2010). Experimental investigations on the effects of cerium oxide nanoparticle fuel additives on biodiesel. *Advances in Mechanical Engineering*, 2, 581407.

- Sandouqa, A., Al-Hamamre, Z., & Asfar, J. (2019). Preparation and performance investigation of a lignin-based solid acid catalyst manufactured from olive cake for biodiesel production. *Renewable Energy*, 132, 667-682.
- Sangkharak, K., Chookhun, K., Numreung, J., & Prasertsan, P. (2020). Utilization of coconut meal, a waste product of milk processing, as a novel substrate for biodiesel and bioethanol production. *Biomass Conversion and Biorefinery*, 10, 651-662.
- Sarkar, D., Goudarzy, M., König, D., & Wichtmann, T. (2020). Influence of particle shape and size on the threshold fines content and the limit index void ratios of sands containing non-plastic fines. *Soils and Foundations*, 60(3), 621-633.
- Sathish, T., & Singaravelu, D. K. (2020). Combustion analysis using third generation biofuels in diesel engine. *Journal of Scientific and Industrial Research*, 79(5), 449-452.
- Saxena, V., Kumar, N., & Saxena, V. K. (2017). A comprehensive review on combustion and stability aspects of metal nanoparticles and its additive effect on diesel and biodiesel fuelled CI engine. *Renewable and Sustainable Energy Reviews*, 70, 563-588.
- Schulz, W., Fraillon, J., Losito, B., Agrusti, G., Ainley, J., Damiani, V., & Friedman, T. (2023). *IEA International Civic and Citizenship Education Study 2022 Assessment Framework*, 133. Springer Nature.
- September, L. A., Kheswa, N., Seroka, N. S., & Khotseng, L. (2023). Green synthesis of silica and silicon from agricultural residue sugarcane bagasse ash: A mini review. *RSC Advances*, 13(2), 1370-1380.
- Seshamamba, B. S. V., Malati, P., Ruth, A. N. G., Mallika, A. S., & Sharma, V. (2018). Studies on physicochemical properties & proximate analysis of Carica papaya seed. *Journal of Pharmacognosy and Phytochemistry*, 7(6), 1514-1519.
- Siddique, M. B. M., Khairuddin, N., Ali, N. A., Hassan, M. A., Ahmed, J., Kasem, S., & Afrouzi, H. N. (2021). A comprehensive review on the application of bioethanol/biodiesel in direct injection engines and consequential environmental impact. *Cleaner Engineering and Technology*, 3, 100092.

- Singh, A., & Nigam, P. S. (2018). Microbial biofuels production. *Microbial Biotechnology*, 170-183. CRC Press.
- Singh, D., Subramanian, K. A., Juneja, M., Singh, K., Singh, S., Badola, R., & Singh, N. (2017). Investigating the effect of fuel cetane number, oxygen content, fuel density, and engine operating variables on NO<sub>x</sub> emissions of a heavy duty diesel engine. *Environmental Progress & Sustainable Energy*, 36(1), 214-221.
- Singh, D. K., & Tirkey, J. V. (2022). Performance optimization through response surface methodology of an integrated coal gasification and CI engine fuelled with diesel and low-grade coal-based producer gas. *Energy*, 238, 121982.
- Sivasaravanan, S., Booma-Devi, P., Nagaraj, M., Jeya-Jeevahan, J., & Britto-Joseph, G. (2019). Influence of rice husk nanoparticles on engine performance and emission characteristics of diesel and neem oil biodiesel blends in a single cylinder diesel engine. *Energy Sources, Part A: Recovery, Utilization, and Environmental Effects*, 1-16.
- Soares, S., Lima, M. J., & Rocha, F. R. (2017). A spot test for iodine value determination in biodiesel based on digital images exploiting a smartphone. *Microchemical Journal*, 133, 195-199.
- Srivastava, N., Srivastava, M., Gupta, V. K., Manikanta, A., Mishra, K., Singh, S., & Mishra, P. K. (2018). Recent development on sustainable biodiesel production using sewage sludge. *3 Biotech*, 8, 1-11.
- Staples, M. D., Malina, R., Suresh, P., Hileman, J. I., & Barrett, S. R. (2018). Aviation CO<sub>2</sub> emissions reductions from the use of alternative jet fuels. *Energy Policy*, 114, 342-354.
- Swenson, H., & Stadie, N. P. (2019). Langmuir's theory of adsorption: A centennial review. *Langmuir*, 35(16), 5409-5426.
- Syafiuddin, A., Chong, J. H., Yuniarto, A., & Hadibarata, T. (2020). The current scenario and challenges of biodiesel production in Asian countries: A review. *Bioresource Technology Reports*, 12, 100608.



- Taherkhani, M., & Sadrameli, S. M. (2018). An improvement and optimization study of biodiesel production from linseed via in-situ transesterification using a co-solvent. *Renewable Energy*, 119, 787-794.
- Thangarasu, V., Balaji, B., & Ramanathan, A. (2019). Experimental investigation of tribo-corrosion and engine characteristics of Aegle Marmelos Correa biodiesel and its diesel blends on direct injection diesel engine. *Energy*, 171, 879-892.
- Thiruselvam, K., Mohan-Gift, M. D., Saravanan, R., & Subramonian, N. (2023). Investigation of usage of neat palm biodiesel in CI engine using cerium oxide nanoparticle addition to the fuel. *International Journal of Ambient Energy*, 44(1), 1396-1405.
- Todkar, B. S., Deorukhkar, O. A., & Deshmukh, S. M. (2016). Extraction of silica from rice husk. *International Journal of Engineering Research and Development*, 12(3), 69-74.
- Tomašek, I., Damby, D. E., Andronico, D., Baxter, P. J., Boonen, I., Claeys, P., & Elskens, M. (2021). Assessing the biological reactivity of organic compounds on volcanic ash: Implications for human health hazard. *Bulletin of Volcanology*, 83, 1-11.
- Ulusoy, Y. (2020). Investigation of particulate matter by FTIR, TEM and elemental analyses in a diesel engine operating on diesel and waste cooking oil-biodiesel. *Environmental Science and Pollution Research*, 27(1), 500-509.
- Vahidi, H., Syed, K., Guo, H., Wang, X., Wardini, J. L., Martinez, J., & Bowman, W. J. (2021). A review of grain boundary and heterointerface characterization in polycrystalline oxides by (scanning) transmission electron microscopy. *Crystals*, 11(08), 878.
- Vardoulakis, S., & Heaviside, C. (2012). Health effects of climate change in the UK 2012. *London: Health Protection Agency*, 10, 1600-0668.
- Varela-Pérez, P., Greiner, B. E., & von Cossel, M. (2022). Socio-Economic and Environmental Implications of Bioenergy Crop Cultivation on Marginal African Drylands and Key Principles for a Sustainable Development. *Earth*, 3(2), 652-682.
- Vergel-Ortega, M., Valencia-Ochoa, G., & Duarte-Forero, J. (2021). Experimental study of emissions in single-cylinder diesel engine operating with diesel-biodiesel blends of palm oil-sunflower oil and ethanol. *Case Studies in Thermal Engineering*, 26, 101190.

- Verma, P., Stevanovic, S., Zare, A., Dwivedi, G., Chu Van, T., Davidson, M., & Ristovski, Z. D. (2019). An overview of the influence of biodiesel, alcohols, and various oxygenated additives on the particulate matter emissions from diesel engines. *Energies*, 12(10), 1987.
- Wang, T. C., Bury, W., Gómez-Gualdrón, D. A., Vermeulen, N. A., Mondloch, J. E., Deria, P., & Farha, O. K. (2015). Ultrahigh surface area zirconium MOFs and insights into the applicability of the BET theory. *Journal of the American Chemical Society*, 137(10), 3585-3591.
- Wei, J., He, C., Lv, G., Zhuang, Y., Qian, Y., & Pan, S. (2021). The combustion, performance and emissions investigation of a dual-fuel diesel engine using silicon dioxide nanoparticle additives to methanol. *Energy*, 230, 120734.
- Wei, J., Yin, Z., Wang, C., Lv, G., Zhuang, Y., Li, X., & Wu, H. (2021). Impact of aluminium oxide nanoparticles as an additive in diesel-methanol blends on a modern DI diesel engine. *Applied Thermal Engineering*, 185, 116372.
- Westphal, K. (2016). 6. The EU: In the Midst of Crisis—Downgraded Sustainable Energy Ambitions. *Sustainable Energy in the G20*, 39.
- Winkler, H. (2007). Energy policies for sustainable development in South Africa. *Energy for sustainable Development*, 11(1), 26-34.
- Zhang, H., Li, C., Guo, J., Zang, L., & Luo, J. (2012). In situ synthesis of poly (methyl methacrylate)/SiO<sub>2</sub> hybrid nanocomposites via “grafting onto” strategy based on UV irradiation in the presence of iron aqueous solution. *Journal of Nanomaterials*, 2012(1), 217412.
- Zhang, Z., Jiaqiang, E., Deng, Y., Pham, M., Zuo, W., Peng, Q., & Yin, Z. (2018). Effects of fatty acid methyl esters proportion on combustion and emission characteristics of a biodiesel fueled marine diesel engine. *Energy Conversion and Management*, 159, 244-253.

## RESEARCH OUTPUTS

### (i) Research Papers

Kapile, F. A., Bereczky, A., Ntalikwa, J. W., & Kivevele, T. T. (2022). Comprehensive analysis of fuel properties of *Adansonia digitata* methyl ester with the influence of nanoparticle additives extracted from agricultural waste. *Waste and Biomass Valorization*, 13(6), 2927-2945.

Kapile, F. A., Bereczky, A., Ntalikwa, J. W., & Kivevele, T. T. (2024). Investigation of engine performance, exhaust emissions, and combustion characteristics of a diesel engine fueled with *adansonia digitata* methyl ester doped with nano-silica additive extracted from agricultural waste”, *Biofuel, Bioproduct, and Biofinery*; Wiley. DOI:10.1002/bbb.2633.

### (ii) Poster Presentation